SEARCH FOR RELIC NEUTRALINOS WITH MILAGRO

by

Lazar Fleysher

A dissertation submitted in partial fulfillment

of the requirements for the degree of

Doctor of Philosophy

Department of Physics

New York University

May, 2003

Thesis Adviser Allen I. Mincer

© Lazar Fleysher

All Rights Reserved, 2003

Apart from very short notes, it was usual to dictate everything into the speakwrite, which was of course impossible for his present purpose. He dipped the pen into the ink and then faltered for just a second. A tremor had gone through his bowels. To mark the paper was the decisive act. In small clumsy letters he wrote:

George Orwell, "1984"

Search for relic neutralinos with Milagro

Dedication

I dedicate this to my family.

Acknowledgements

"What happens to you here is forever",
O'Brien had said. That was a true word.
George Orwell, "1984"

I consider myself lucky because I can boast that I have not one, not two, but three thesis advisors. Allen Mincer is the main one and I thank you for taking risk in allowing me to proceed with the dark matter search project. I also thank you for taking responsibility for me while I was a graduate student at NYU. There are countless reasons why I am grateful to you so I will just thank the fate who had given you to me.

I would like to thank Todd Haines from Los Alamos National Laboratory who had been my advisor from the moment my foot landed on the steps of the Milagro building at the laboratory. Not only am I obliged for your help and support of my work on Milagro detector itself, but also for your guidance in scientific research. I am thankful to you for proposing the dark matter search as the main topic of my thesis.

I also mention Peter Nemethy who has been my advisor as well. While your official duties were to guide my brother through his research, you payed considerable attention to me as well. I thank you for introducing me to Milagro in the first place.

During my work on Milagro I met many people whom I consider as founts of knowledge and I am thankful to them for allowing me to glean the knowledge. These people are Gaurang Yodh, Cy Hoffman, Gus Sinnis, Don Coyne, Jim Ryan, Jordan Goodman, David Berley, David Williams, Tony Shoup and Bob Ellsworth. Thank you.

I also cherish my experience with the many post docs and graduate students who made my life in Los Alamos more enjoyable. These are Rob Atkins, Wystan Benbow, Diane Evans, Isabel Leonor, Joe McCullough, Julie McEnery, Richard Miller, Frank Samuelson, Andy Smith, Kelin Wang, Morgan Wascko and Stefan Westerhoff. Thank you again.

I am also in debt to Gerard Jungman and Salman Habib from the T-division at the

Los Alamos Laboratory for their contribution to this project.

To the names listed above I would like to add my twin-brother Roman. Roman has always been and always will be a special person in my life. The person who understands me from "half a word", my ally, my critic, my friend and my co-dreamer. Without him many dreams would still be dreams.

There are people whose help and support is often taken for granted. These are my parents and grandparents. They are the people who made me, who taught me what "right" and what "wrong" is, who nourished and diversified my interests. These are the people who taught me that an educated person can do a job better regardless of whether it is conducting esoteric research, moving furniture, weeding vegetable fields or climbing telephone poles. Thank you for giving me all that and much more.

I would also like to thank my wife Asya Shpiro and our daughter Sonya for their understanding and support during the final stages of my thesis research.

I am also grateful to all my friends who supported and inspired me during the "dark" phases of my life and shared joy and happiness during the "bright" ones.

I was honored by the presence of professors Allen Mincer, Georgi Dvali, Todd Haines, Peter Nemethy and Engelbert Schucking at my dissertation defense.

Lazar Fleysher
New York University
April 14, 2003

Abstract

The neutralino, the lightest stable supersymmetric particle, is a strong theoretical candidate for the missing astronomical "dark matter". Depending on their annihilation cross section, relic neutralinos from early formation of the Universe trapped in orbits around massive objects may currently be annihilating at measurable rates. The Minimal Supersymmetric extension of the Standard Model predicts that the gamma rays emerging from one of the annihilation modes will give a distinct monochromatic signal with energy between 100GeV and 10TeV, depending on the neutralino mass. An additional "continuum" spectrum signal of photons will be produced by the decay of secondaries produced in the non-photonic annihilation modes.

Milagro is an air shower array which uses the water Cherenkov technique and is capable of detecting TeV gamma rays from the direction of the Sun with an angular resolution of less than a degree. It is the first instrument capable of establishing a limit on the gamma-ray flux from neutralino annihilations near the Sun.

In this report results of a search for neutralino to photon annihilation with the Milagro gamma-ray observatory are presented. Results of a Monte Carlo computer simulation of the neutralino annihilation density in the Solar System suggest that a large portion of neutralino annihilations ($40 - 50\%$) happens outside the Sun which may give rise to a detectable gamma-ray signal from the solar region. No significant gamma-ray signal was observed from the Sun resulting in an upper limit on the sought for photon flux. The upper limit can be translated to a neutralino-mass dependent limit on the product of the neutralino-proton scattering crossection $\sigma_{p\chi}$, the integrated photon yield per neutralino in neutralino-neutralino annihilation b_γ and the local galactic halo dark matter density ρ_0. For example, assuming a 1TeV neutralino and ignoring the continuum contribution to the signal gives an upper limit of $\frac{\rho_0}{0.3\ (GeV\,cm^{-3})}\frac{\sigma_{p\chi}}{10^{-41}\ (cm^2)}b_\gamma^\delta < 2.3$.

Contents

Dedication **iv**

Acknowledgements **v**

Abstract **vii**

List of Figures **xi**

List of Tables **xiv**

List of Appendices **xv**

1 Introduction **1**
1.1 The dark matter problem. 1
1.2 Supersymmetry. 4
1.3 Detection Methods. 4
1.3.1 Direct detection. 5
1.3.2 Indirect Detection. 6

2 Extensive Air Showers **8**
2.1 Development of EAS. 9
2.1.1 Longitudinal Development of Extensive Air Showers. 9
2.1.2 Lateral Development of Extensive Air Showers. 11
2.1.3 Temporal Distribution of Extensive Air Shower Particles. 12
2.2 Cosmic rays. 13
2.3 Air shower detection methods. 14

3 The Milagro Detector **15**
3.1 General description. . . . 16
3.1.1 Photomultiplier tube. . . . 17
3.1.2 PMT pulse model, time over threshold. . . . 18
3.1.3 The Detector trigger. . . . 20
3.2 Event Reconstruction. . . . 20
3.2.1 Pre-processing. . . . 21
3.2.2 Processing: angle, time, energy, type. . . . 23
3.2.3 Post-Processing: Analysis Techniques. . . . 25
3.3 Detector performance and simulations. . . . 26
3.3.1 Effective area. . . . 27

4 Analysis Techniques **28**
4.1 Coordinates on the Celestial Sphere. . . . 28
4.1.1 Celestial Sphere. . . . 28
4.1.2 J2000 reference. . . . 31
4.1.3 Diurnal parallax. . . . 32
4.1.4 Milagro event coordinates. . . . 32
4.2 Sky Mapping. . . . 33
4.3 Statistical Nature of Signal Establishment. . . . 35
4.3.1 General test construction. . . . 35
4.3.2 Testing a composite hypothesis. . . . 37
4.3.3 Significance of a measurement. . . . 38
4.3.4 Setting an upper limit. . . . 41
4.4 Background estimation. . . . 43
4.5 Performing test for a source presence. . . . 45
4.6 Gamma-Ray flux measurement. . . . 46
4.7 Optimal bin. . . . 47

5 Photon flux at the Earth due to near solar neutralino annihilations **52**
5.1 General formulation of the problem. . . . 53
5.2 General idea of the solution. . . . 55
5.2.1 Solution of the Fredholm equation. . . . 56
5.2.2 Transition tables $\{(X_\infty, cap), (X_0, cap)\}$. . . . 58
5.2.3 Distribution of neutralinos at infinity $P(X_\infty)$. . . . 59
5.2.4 Capture probability $P(cap|X_\infty)$. . . . 61

5.3 Predicted photon flux. 64

6 Outcome of the test for presence of the photon flux from the Sun and its implications 68

6.1 The data set. 69

6.2 A limit on possible gamma-ray flux due to near-Solar neutralino annihilations. 71

7 Conclusion 75

Appendices 77

Bibliography 123

List of Figures

1.1 A "typical" rotation curve of a "typical" galaxy, determined from 21cm observations.[45] 2
1.2 Exclusion regions for neutralino-nucleon crossections obtained from different direct-search experiments. Closed contour is allowed region at 3σ confidence level from the DAMA experiment. The plot is adopted from [8]. 5

2.1 Longitudinal development of electron (left) and photon (right) compontents of gamma-ray showers with $E_{th} = 1\ (MeV)$ particle detection threshold. 10
2.2 Density of electrons (left) and photons (right) in a gamma-ray shower at atmospheric depth of 20 radiation lengths as a function of the core distance with $E_{th} = 1\ (MeV)$. Curves are normalized to the total number of respective particles. 11
2.3 Average arrival time of the shower front as a function of core distance (illustration). 12

3.1 Schematic view of the Milagro pond. 16
3.2 Illustration of HiToT, LoToT and edge-train 19
3.3 Block diagram of detector electronics 20

4.1 Definitions of main points and arcs on the Celestial sphere 29
4.2 Concept of the auxiliary coordinate system on the Celestial sphere centered on L (left) and corresponding sky projection (right). The "y"-axis of the sky projection always points to a pole M and the circles are the lines of $\chi = const$ at $\chi = \pi/6,\ \pi/3,\ \pi/2$. 34
4.3 Critical region illustration for the statistic U when $\lambda_1 > \lambda$. 42

4.4 Conceptual diagram of a small angular reconstruction error parameterization. 49
4.5 Optimal bin size $\tilde{\omega}^{\sigma}_{opt}$ as a function of the size source $\bar{\omega}^{\sigma}$. 51

5.1 Radial distribution of the annihilation points for $m_{\chi} = 200\ (GeV)$ and $\sigma_{p\chi} = 10^{-43}\ (cm^2)$. Vertical scale is in arbitrary units, horizontal scale is in $R_{\odot}$. above $25 \cdot 10^6$ neutralino annihilations 66
5.2 Radial distribution of the annihilation points for $m_{\chi} = 1000\ (GeV)$ and $\sigma_{p\chi} = 10^{-43}\ (cm^2)$. Vertical scale is in arbitrary units, horizontal scale is in $R_{\odot}$. above $22 \cdot 10^6$ neutralino annihilations 67

6.1 Significance maps of the regions of the sky around the daytime Moon(left) and the Sun(right) and the corresponding source exposure as function of zenith angle in hours per degree. The color code is the value of U (see equation (4.7)). 70
6.2 The values of (F_{δ},F_c) below the lines are allowed based the constructed upper limit for corresponding neutralino masses. 72
6.3 The values of $\left(\rho_0 \sigma_{p\chi} b^{\delta}_{\gamma},\ \rho_0 \sigma_{p\chi} b^{c}_{\gamma}\right)$ below the lines are allowed based the constructed upper limit for corresponding neutralino masses. 74

B.1 Calibration system setup 80
B.2 Illustration of the electronic slewing. Stronger pulses cross the discriminator threshold earlier than the weaker ones. 82
B.3 Plots show T_{start} vs ToT data obtained for calibration (left) and the polynomial fit to the data (right). The units of both axes are TDC counts. 82
B.4 Filter wheel calibration with and without noise suppression. (Bank 2,3 represent laser balls 11-20 and 21-30 respectively, while AS and MU represent PMTs from "top" and "bottom" layers used for filter calibration.) 87

C.1 Schematic of the map 95
C.2 Auxiliary coordinates on the Celestial sphere 95

D.1 Elliptical trajectory inside the Sun. 100
D.2 Elliptical trajectory outside the Sun. 103
D.3 Rotation of the outside orbit due to passage through the Sun. 104
D.4 Finalize 109

D.5 Scattering diagram. $\vec{AO} = \frac{m_\chi}{m_\chi+m_p}(\vec{p}_\chi + \vec{p}_p)$, $\vec{OB} = \frac{m_p}{m_\chi+m_p}(\vec{p}_\chi + \vec{p}_p)$, $\vec{OC} = |\mu\vec{v}|\vec{n}$. 113

List of Tables

2.1 Values of parameters A, a and b for modified Greisen and NKG formulae. 10

4.1 Significance ξ_c and corresponding critical value u_c. 42
4.2 Source size $\bar{\omega}^\sigma$ and corresponding optimal bin size $\tilde{\omega}^\sigma_{opt}$. 51

5.1 Summary of the simulation/computation results. Capture integral I and the fraction f_{out} of annihilations between 1 and 2 solar radii as a function of neutralino mass m_χ. 64

6.1 Number of events in the optimal bin centered on the Sun and the Moon (see section 4.5). 69
6.2 Coefficients of the flux limit calculation (see equation (6.1)). 71
6.3 The upper limit on the monochromatic photon flux due to near-solar neutralino annihilations and corresponding upper limit on the $\sigma_{p\chi}\rho_0 b^\delta_\gamma$. . 71
6.4 The upper limit on the continuum photon flux due to near-solar neutralino annihilations and corresponding upper limit on the $\sigma_{p\chi}\rho_0 b^c_\gamma$. . . . 72

B.1 Occupancy accuracy test results to satisfy the error $q = \frac{\Delta\lambda}{\lambda} = 0.01$ on measured λ with $n = 2000$ laser shots. 88

List of Appendices

A Poisson distribution **77**

A.1 Definition 77
A.2 Gaussian Limit of Poisson Distribution 78

B Calibration **79**

B.1 Calibration system setup. 80
B.2 Timing calibration. 81
B.2.1 TDC Conversion Factor. 81
B.2.2 Electronic slewing correction. 81
B.2.3 Speed of light in water, fiber delay. 83
B.3 Photo-Electron calibration. 84
B.3.1 Low light level calibration and the Occupancy method. 84
B.3.2 High light level calibration. 85
B.3.3 Filter calibration. 86
B.3.4 Dynamic Noise Suppression. 86
B.3.5 Statistical error of the occupancy method. 87
B.3.6 Threshold effect on the occupancy measurement. 89
B.4 Calibration Extrapolation. 91
B.4.1 Slewing extrapolation. 91
B.4.2 PE extrapolation. 92
B.5 Energy calibration. 93

C Auxiliary Celestial Coordinate system **94**

D Kinematics of the particles in the Solar system (Simulations appendix) 96

D.1 `propagate_infinity()` . . . 96
D.2 Conserved quantities. . . . 97
D.3 Which orbits cross the Sun. . . . 98
D.4 Rotation of a vector $\vec{B}$ around a vector $\vec{L}$ by an angle γ. . . . 98
D.5 Some facts about elliptical trajectories. . . . 99
D.5.1 Equation of the ellipse. . . . 99
D.5.2 Ellipse inside the Sun. . . . 100
D.5.3 Angle between $\vec{r}$ and $\vec{v}$. . . . 102
D.5.4 Ellipse outside the Sun. . . . 102
D.5.5 Rotation of outside orbit due to passage through the Sun. . . . 103
D.6 Motion inside the Sun `propagate_in_sun()`. . . . 104
D.6.1 Particle is inside the Sun. . . . 105
D.6.2 Orbit exits the Sun, but the particle doesn't. . . . 106
D.6.3 Particle exits the Sun. . . . 106
D.7 Motion outside the Sun `propagate_outside_sun()`. . . . 107
D.7.1 Find the scattering point. . . . 107
D.7.2 Particle on an unbound orbit crossing the Sun. . . . 109
D.7.3 Velocity at infinity. . . . 109
D.8 SolvePath4Psi. . . . 110
D.8.1 Bracketing the root. . . . 111
D.8.2 Circular bracketing. . . . 112
D.8.3 The solution. . . . 112
D.9 Scattering in the Sun. . . . 112
D.9.1 Elastic scattering. . . . 113
D.9.2 Choosing the axis of rotation. . . . 114
D.10 Generate path inside the Sun. . . . 115

E Comments on the upper limit construction procedure 116

E.1 Sensitivity and upper limit. . . . 117
E.2 Problem with the current approach. . . . 118
E.3 Example I. . . . 118
E.4 Example II. . . . 119
E.5 Example III. . . . 120
E.6 When is the new theory valid? . . . 122

Chapter 1

Introduction

Chapter 1, like Chapter 3, had not actually told him anything that he did not know; it had merely systematized the knowledge that he possessed already.

George Orwell, "1984"

1.1 The dark matter problem.

Perhaps, there is no problem of greater importance to cosmology and astrophysics than that of the "dark matter". It is centered around the notion that there may exist an enormous amount of non-luminous matter in the Universe. The presence of the matter, which does not radiate and can not be seen directly, can only be inferred by observing the effects it has on other directly observable astronomical objects.

It has always been known that there is matter in the sky which does not emit any kind of radiation. For instance, the planets do not shine, but their contribution to the mass of the solar system is negligible, so worrying about non-luminous matter was not of a great concern.

The first evidence that there is a significant amount of dark matter came from Zwicky [53], in the thirties, from investigations of clusters of galaxies. It was found that velocities of the galaxies in a cluster were about 10 times larger than expected, indicating that there is invisible gravitating matter in a cluster, holding the galaxies together.

Somewhat more reliable evidence was found in the 1970s by Rubin [44] by studying

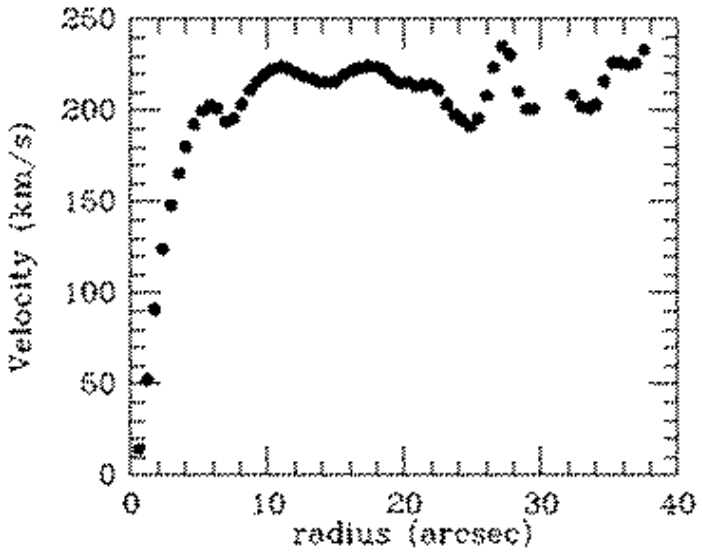

Figure 1.1: A "typical" rotation curve of a "typical" galaxy, determined from 21cm observations.[45]

the rotation curves of spiral galaxies. Kepler's law states that the rotational velocity around a gravitational center depends only on the distance from the center and on the total mass contained within the orbit. Thus, one expects:

$$GM(r) \cong v^2 r$$

where v – is the circular velocity at a distance r from the center of the galaxy, $M(r)$ is the mass enclosed in the sphere r and spherical symmetry is assumed.

If the mass were associated with light (luminous matter) v would decrease as $r^{-1/2}$ beyond the point where the light cuts off. However, it was found (See, for instance [45, 41], or fig 1.1) that $v \approx const$, corresponding to $M(r) \propto r$, implying existence of dark halos around spiral galaxies. The halos could be made of brown dwarf stars, jupiters, planets and $100 M_\odot$ black holes. Collectively, these objects are called MACHOs[1] and are the main baryonic dark matter candidates.

Dark matter has important consequences for the evolution of the Universe. The standard, Hot Big Bang cosmology is remarkably successful: it provides a reliable and tested

[1]MaCHO is Massive Compact Halo Object

account of the history of the Universe from at least $t \sim 10^{-2} s$ until today ($t \sim 14\, Gyr$). At present, there is no strong experimental evidence contradicting the theory. According to the theory, the Universe must conform to one of three possible types with negative, positive or zero curvature. The value of the cosmological density parameter,[2] Ω_{total}, determines which of the three possibilities applies to our world. There is, however, a somewhat philosophical or even aesthetical argument that makes $\Omega_{total} = 1$ attractive. The point is that as the Universe evolves, the value of Ω_{total} changes. In fact, the value of $\Omega_{total} = 1$ is unstable. If the Universe is open $\Omega_{total} < 1$, it will expand forever, until it is totally empty $\Omega \stackrel{t\to\infty}{\longrightarrow} 0$. On contrary, if it is closed $\Omega_{total} > 1$, it will recollapse to a state with extremely high density $\Omega \stackrel{t\to\infty}{\longrightarrow} \infty$. The inflationary cosmology [31], which provides the most compelling explanation for the smoothness of the Cosmic Microwave Background Radiation (CMBR), predicts that the early Universe was extremely close to flat $|\Omega_{total} - 1| < \mathcal{O}(10^{-60})$, leading to the belief that Ω_{total} is exactly one.

In fact, the most recent results from the studies of the CMBR with the WMAP [7] observatory yield $\Omega_{total} = 1.02 \pm 0.02$. The same study implies that the matter component of the total energy density is $\Omega_m = 0.27 \pm 0.04$ while ordinary baryonic component constitutes only about 15% of all matter in the Universe $\Omega_b = 0.044 \pm 0.004$. The rest of the energy density $\Omega_\Lambda = (\Omega_{total} - \Omega_b) = 0.73 \pm 0.04$ is an unknown from of energy (so-called "dark energy").

In any event, the abundance of baryons is not likely to account for all matter even if Ω_{total} turns out to be slightly less than unity and non-baryonic dark matter is almost required to dominate the Universe. The particles or fields which comprise nonbaryonic dark matter must have survived from the Big Bang, and therefore, must either be stable or have lifetimes in excess of the current age of the Universe. Among the non-baryonic dark matter candidates there are massive neutrinos, axions [49] and stable supersymmetric particles.

[2] $\Omega = \rho/\rho_c$, ρ – energy density of the Universe, ρ_c – critical parameter;

$$\Omega \begin{cases} < 1 & \text{negative curvature, the Universe will expand forever} \\ = 1 & \text{zero curvature Universe} \\ > 1 & \text{positive curvature, the Universe will recollapse, eventually} \end{cases}$$

1.2 Supersymmetry.

The main goal of the elementary particle physics is to devise a model which combines all particles and their interactions into one theory. The hope is that the development of supersymmetric theories (See, for example, [47]) is a step towards the stated goal. In these theories, bosonic and fermionic fields are allowed to transform into one another, and each particle is described by a multiplet containing bosons and fermions. In such models, loops, divergent in quantum field theories, cancel. Theoretical strong points of supersymmetry have motivated many accelerator searches for supersymmetric particles. Most of these have been guided by the Minimal Supersymmetric extension of the Standard Model (MSSM) and are based on a missing-energy signature caused by the escape of the lightest supersymmetric particles. In the MSSM, the convergence of the renormalized gauge couplings at the grand unification scale requires all masses of supersymmetric particles to appear between $100\ (GeV)$ and $10\ (TeV)$ [2]. Laboratory searches have set lower mass limits, requiring lightest supersymmetric particles in MSSM to possess masses greater than $20 - 30\ (GeV)$ [11]. Even though no convincing evidence for existence of supersymmetric particles has been found, they all have been given names. Bosonic ordinary particles have fermionic superpartners with the same name except with the suffix "ino" added, while fermionic ordinary particles have bosonic superpartners with prefix "s" added. For example, Higgsino is a superpartner for Higgs boson and selectron is a superpartner for electron. There are several superpartners which have the same quantum numbers and so can mix together in linear combinations. Since those do not necessarily correspond to any ordinary particle, they are given different names. For instance, the photino, Higgsino and Zino can mix into arbitrary combinations called the neutralinos. The lightest neutralino is a stable supersymmetric particle and makes the "best" candidate for a solution of the "dark matter problem"(first suggested in [42], also see [29] for an extensive review).

1.3 Detection Methods.

There are several ways to test the hypothesis that stable neutralinos exist and contribute to the dark matter. They include direct searches with extremely sensitive devices which can detect energy deposited by an elastically scattered neutralino off a nucleus and indirect searches which look for products of neutralino-neutralino annihilations.

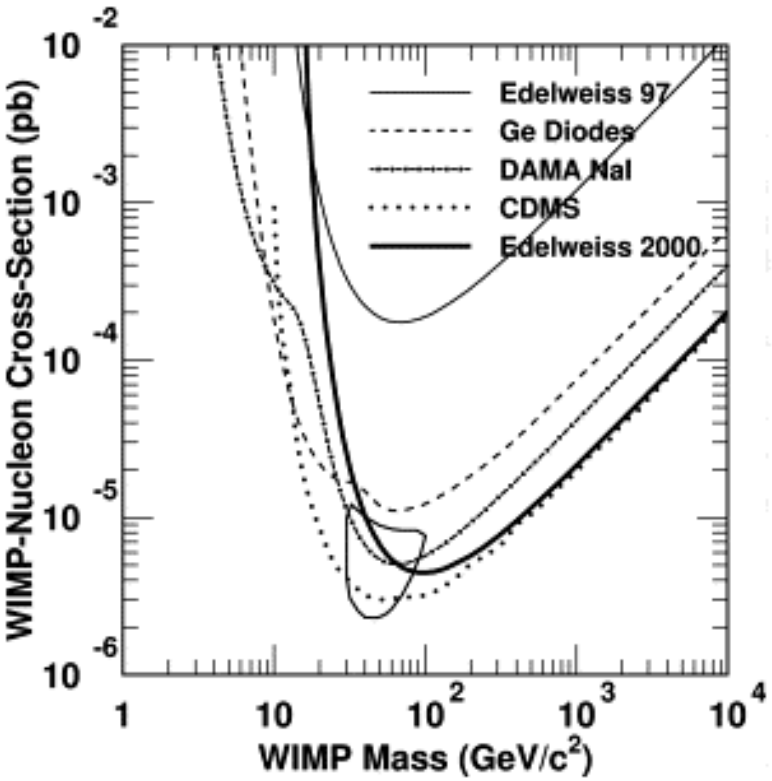

Figure 1.2: Exclusion regions for neutralino-nucleon crossections obtained from different direct-search experiments. Closed contour is allowed region at 3σ confidence level from the DAMA experiment. The plot is adopted from [8].

1.3.1 Direct detection.

The Italian/Chinese collaboration (DAMA) has reported an annual modulation in the total count rate over 4 years. They interpret this as consistent with the annual modulation predicted for WIMPs [10]. This, however, is not a widely accepted result because of some possible modulating systematic errors. The CDMS experiment has obtained data that appear to exclude the DAMA result [1]. They reach a spin-independent WIMP-nucleon scrossection limit around $2 \cdot 10^{-42}\ (cm^2)$ in the mass range $20 - 100\ (GeV)$. Edelweiss has also released results that significantly cut into the DAMA allowed region [8]. The summary of the limits of direct searches is shown on the figure 1.2.

1.3.2 Indirect Detection.

Indirect searches also have received considerable attention from experimenters. For example, the Kamiokande and SuperKamiokande underground neutrino detectors have set limits on solar and terrestrial neutralino-induced muon fluxes [37, 25].

Another possible method for detecting dark matter particles is from their annihilation into γ-rays. One of the many possible gamma-producing channels is production of monochromatic gamma-rays:

$$\chi\chi \quad \rightarrow \quad \gamma\gamma, \quad \chi\chi \quad \rightarrow \quad Z\gamma$$

Even though it is difficult to estimate the rates of these processes because of uncertainties in the supersymmetric parameters, cross sections and the neutralino distribution, since the annihilating neutralinos move at galactic velocities $v/c \sim 10^{-3}$ the outgoing photons will give very distinct monochromatic signals[3] in each annihilation mode:

$$E_\gamma = M_\chi, \quad E_\gamma = M_\chi \left(1 - \left(\frac{m_Z}{2M_\chi}\right)^2\right)$$

which has no conceivable origin from any known astrophysical sources.

As was mentioned earlier, neutralinos, if they are to be the dark matter, should have non-zero relic abundance today, but their number density is so small that almost no annihilations happen. An observation of such an event from some random point in the Universe is not feasible. However, since the density of neutralinos in the vicinity of a gravitational center will be larger than in other parts of the Universe and because the annihilation rate is proportional to the square of the neutralino density, there will be an enhanced flux of high energy γ-rays from such regions. Therefore, it is tempting to look at signals from well studied gravitating objects, such as nearby galaxies and the Milky Way Galaxy, and examine the energy spectrum for a monoenergetic signal.

The present high energy gamma-ray experiments, such as EGRET and the Whipple atmospheric Cherenkov Telescope, lack the sensitivity to detect annihilation line fluxes predicted for most of the allowed supersymmetric models and halo profiles. However, the next generation ground-based and satellite gamma-ray experiments, such as

[3] If these two lines can be resolved, the relative strength of the two could give a handle on the composition of the neutralino. This is because despite the fact that the two processes are closely related, there are some differences which depend on the composition.

GRANITE-III, VERITAS and GLAST, will allow exploration of large portions of the MSSM parameter space, assuming that the dark matter density is peaked at the galactic center. [9]

The Sun is also a large gravitating object and one could study the solar spectrum for the neutralino annihilation signal. Of course, that is possible only with a non-optical high resolution instrument, capable of monitoring the Sun at energies between $100\ (GeV)$ and $10\ (TeV)$. Several semi-analytical estimates for the detection rates for several ground-based and satellite experiments are available in the literature. However, a more careful computer simulation following the decaying 3-D neutralino orbits with detailed elastic scattering and planetary perturbations accompanied by simulations of the solar magnetic field smearing and shadowing of the galactic cosmic rays by the Sun will provide a more definitive prediction on the neutralino annihilation rate.

The structure of this work is the following: chapter 2 discusses how high energy cosmic particles can be detected. This is followed by a brief description of the Milagro detector, capable of monitoring the overhead sky at energies near $1\ (TeV)$, in chapter 3. A presentation of the data analysis techniques employed in the current work is given in chapter 4. Chapter 5 discusses the computer simulations which are used to predict the gamma ray flux from the near-solar neutralino annihilations. Chapter 6 discusses the results of the search for the relic neutralinos and is followed by a summary in chapter 7.

Chapter 2

Extensive Air Showers

All one knew was that every quarter astronomical numbers of boots were produced on paper, while perhaps half the population of Oceania went barefoot.

George Orwell "1984"

There are several main reasons which govern the choice of a detector type to be used in high energy photon search from the Sun. First of all, it should be a non-optical device capable of monitoring the solar region. Because, the Earth's atmosphere is opaque to gamma rays, satellite-based detectors need to be constructed to detect gamma rays. Indeed, small detectors sensitive to gamma rays at energies below a few GeV have been constructed and used successfully.[1] These detectors employ techniques developed for accelerator experiments where an incoming photon's direction is determined by e^+e^- tracking detectors and the photon's energy is usually measured by a total-absorption calorimeter. However, the expected low and rapidly decreasing with photon energy γ-ray flux requires detectors with rather large collection areas and long exposure periods. Such detectors can be built on the surface of the Earth only.

Even though direct detection of γ-rays is not possible by ground-based instruments, at energies above several GeV indirect gamma-ray detection is possible. Such very high energy photons initiate extensive air shower (EAS) cascades of secondary particles which are detectable by ground-based detectors. Knowledge of the EAS structure is

[1] Future satellite detectors such as GLAST should register particles with energies as high as 300 (GeV) [21].

required to infer information about the primary photon.

2.1 Development of EAS.

Although an extrapolation from known particle physics might be necessary to describe the initial phase of the shower development, it is believed that the structure of the EAS is well understood. A high-energy primary photon interacts with electromagnetic fields of air molecules in the upper atmosphere producing an electron-positron pair which in turn produces high-energy photons via bremsstrahlung. The resulting electro-magnetic cascade grows geometrically as it propagates through the atmosphere. The shower growth stops when the mean energy of electrons and positrons falls below the critical energy ($E_c \sim 85\ (MeV)$) where the ionization energy-loss mechanism, which does not produce additional shower particles, becomes dominant. After this point (called the shower maximum) the energy of particles and their number in the shower start to decrease as the shower continues its propagation towards the ground level. Nevertheless, a large number of shower particles may reach the ground and may be detected.

Moreover, because the secondary particles are ultra-relativistic, they retain the directionality of the incident gamma ray and the cascade arrives to the ground as a thin front perpendicular to the direction of the primary photon. The density of shower particles in the front will decrease with distance from the extrapolated incident gamma-ray trajectory. This trajectory is called the core of the shower.

The shower development is a stochastic process and while some analytical calculations have been performed, computer simulations are generally employed to study the properties of the air shower cascades.

2.1.1 Longitudinal Development of Extensive Air Showers.

The average number of electrons N_e and photons N_γ in an electromagnetic shower can only depend on the primary energy E_0 and the thickness of the traversed matter t. Moreover, if E_0 is expressed in units of critical energy E_c and t is in units of radiation lengths X_0, the number of electrons and photons is almost independent of the specific shower propagation medium. Usually, however, detectors can register particles with energies above some E_{th}, thus, often, it is desired to know the number of particles in a shower with energies greater than E_{th}. According to [46] the average number of particles $N_k(E_0, E_{th}, t)$ of type k with energy above E_{th} at atmospheric depth t in a shower

E_{th},	k=electron			k=photon		
MeV	A	a	b	A	a	b
1	0.92	0.00	0.45	4.80	-0.88	0.83
5	0.75	0.19	-1.22	2.98	-0.69	-1.49
10	0.63	0.35	-2.57	2.13	-0.57	-3.45
20	0.50	0.53	-4.22	1.45	-0.36	-5.51

Table 2.1: Values of parameters A, a and b for modified Greisen and NKG formulae.

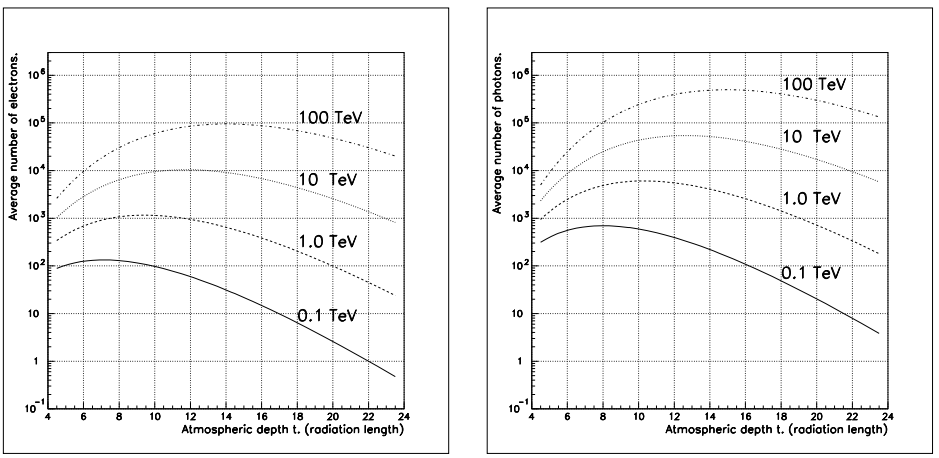

Figure 2.1: Longitudinal development of electron (left) and photon (right) compontents of gamma-ray showers with $E_{th} = 1\ (MeV)$ particle detection threshold.

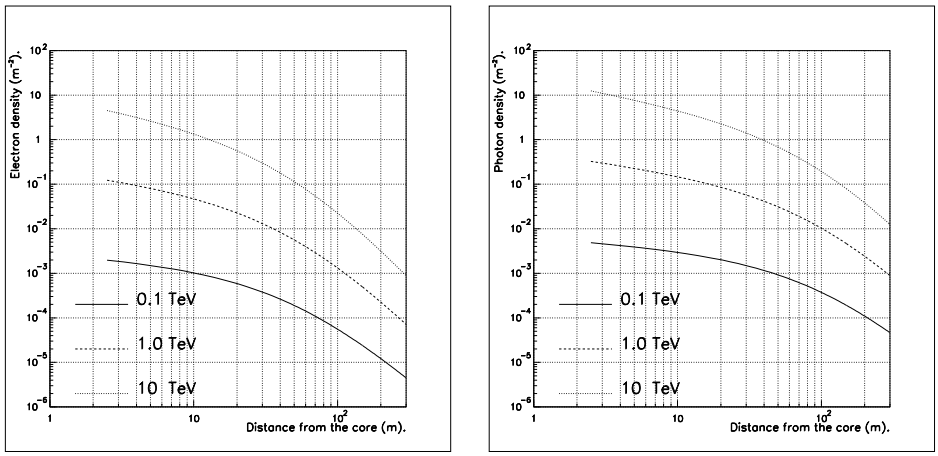

Figure 2.2: Density of electrons (left) and photons (right) in a gamma-ray shower at atmospheric depth of 20 radiation lengths as a function of the core distance with $E_{th} = 1\ (MeV)$. Curves are normalized to the total number of respective particles.

initiated by a photon with energy E_0 can be described by a modified Greisen formula:

$$N_k(E_0, E_{th}, t) = A_k(E_{th}) \frac{0.31}{\sqrt{y}} e^{t_k(1-1.5 \ln s_k)}$$

$$y = \ln \frac{E_0}{E_c}, \quad t_k = t + a_k(E_{th}), \quad s_k = \frac{3t_k}{t_k + 2y}$$

The parameterization is valid for $4 < t < 24$ and $0.1 < E_0 < 10^3\ (TeV)$. The coefficients $A_k(E_{th})$ and $a_k(E_{th})$ are given in the table 2.1 The graphical illustration of the number of particles in a shower is presented in figure 2.1.

2.1.2 Lateral Development of Extensive Air Showers.

The average surface density $\rho_k(E_0, E_{th}, t, r)$ of particles of type k in the shower front with energies greater than E_{th} at a distance r from the shower axis and at the atmospheric depth t can be described by a modified Nishimura-Kamata-Greisen (NKG) function [46]

$$\rho_k(E_0, E_{th}, t, r) = \frac{N_k(E_0, E_{th}, t)}{R_k^2} f(r/R_k, \tilde{s}_k)$$

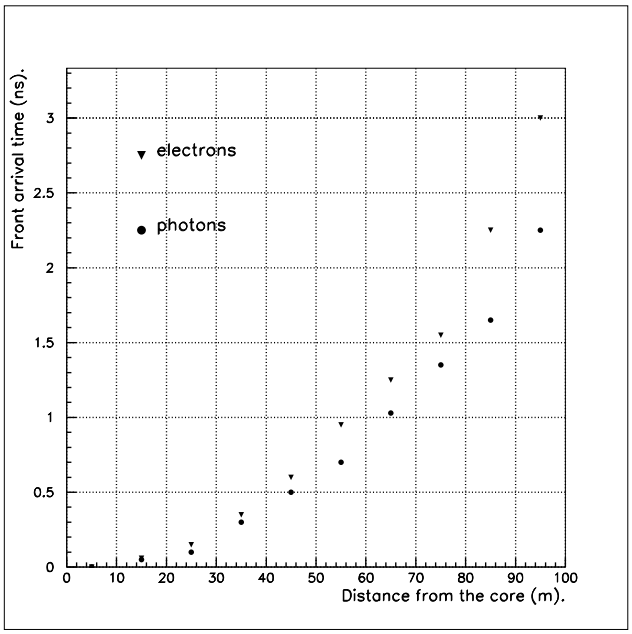

Figure 2.3: Average arrival time of the shower front as a function of core distance (illustration).

$$\tilde{s}_k = \frac{3(t + b_k(E_{th}))}{t + b_k(E_{th}) + 2y}, \quad f(x,z) = \frac{1}{2\pi} \cdot \frac{1}{B(z, 4.5 - z)} x^{z-2}(1+x)^{z-4.5}$$

where $B(z,w)$ is the beta-function so that $2\pi \int_0^\infty f(x,z)xdx = 1$. The characteristic scattering length for photons $R_\gamma = \frac{m_e c^2 \sqrt{4\pi/\alpha}}{E_c} X_0$ is the Molière scattering unit and for electrons — $R_e = R_\gamma/2$.

The values of parameters $b(E_{th})$ are given in the table 2.1 and the average density of photons and electrons per unit area is shown of figure 2.2 as a function of distance from the shower axis.

2.1.3 Temporal Distribution of Extensive Air Shower Particles.

Because the air shower detectors determine the primary particle direction using particle arrival times, knowledge of the shape of the shower front is important for achieving the

best possible angular resolution. Results of Monte Carlo simulations [46] of shower front are shown on figure 2.3. The shower front appears to have a parabolic shape as a function of distance from the core. At large atmospheric depths air shower photons travel faster than air shower electrons thus the photonic front is curved less than the electronic one. The thickness of the shower is defined by the distribution of the shower particle arrival times at distance r from the shower core and increases with the core distance r. At small core distances the fluctuations of arrival time around its average appear to be smaller for the photon component than for the electron one and, consequently, photonic thickness is smaller than the electronic one. At large core distances, however, the electronic contribution to the shower is quite small due to electron ionization losses in the atmosphere compared to the photonic component.

2.2 Cosmic rays.

Among the particles which enter the Earth's atmosphere gamma rays present a very small fraction. Most of the particles are so-called cosmic rays consisting of protons, helium nuclei and the nuclei of the heavier elements such as carbon, oxygen and iron. Just as gamma rays, cosmic rays initiate cascades in the atmosphere. Heavier cosmic rays may interact with air nuclei and produce high energy nucleons. High energy protons interacting with air nuclei may produce neutral and charged pions. Neutral pions have a rather short lifetime and decay, dominantly into photons which may, in turn, produce electromagnetic cascades. Charged pions have longer lifetime and may decay into muons and neutrinos or may interact with the air nuclei creating secondary high energy hadrons and replenish the cascade. Muons, produced in the cascade, may also survive to the ground level. The shower stops its growth when secondary high energy hadrons and photons can not be produced.

Because cosmic rays are charged particles they interact with the interstellar and interplanetary magnetic fields and do not provide directional information about their sources. Thus, cosmic rays may constitute an unwanted background for a gamma-ray telescope. Presence of muons in hadronic cascades is often exploited to differentiate cosmic-ray cascades from the gamma-ray ones.

2.3 Air shower detection methods.

The detectors used in high-energy astrophysical experiments are based on those developed for laboratory ones. Since the showers extend over large areas large detectors are necessary to sample the shower. Cloud/bubble chambers are not suitable for electronic data recording and gas-filled discharge tubes are not practical for large area detectors. Because charged particles constitute a large fraction of the shower particles scintillation and Cherenkov radiation detection techniques are employed in modern air shower detectors. Cherenkov detectors detect radiation produced when a charged particle moves through a dielectric medium at velocity greater than that of light in the medium. Scintillation counters detect light (luminescence) produced as a result of recombination of the electron-hole pairs created by ionizing particles traversing the scintillation medium.

If the Earth's atmosphere is used as the detection medium this results in the air-Cherenkov and "fluorescence" detectors. Air-Cherenkov detectors typically have energy thresholds of about several hundreds of GeV, while fluorescence ones can detect high energy cosmic rays with energies above $100\ (PeV)$. Such detectors typically have good angular resolution but are very narrow field-of-view devices and can operate only on cloudless, moonless nights.

Scintillation arrays have also been built and, due to their sparseness, have rather high energy thresholds (typically above several tens of TeV). Such detectors have worse angular resolution but can observe the entire overhead sky 24 hours a day regardless of weather conditions.

The goal of the Milagro project is to built a detector sensitive to cosmic gamma rays at energies around 1 TeV and capable of continuously monitoring the overhead sky with angular resolution of less than 1 degree.

Chapter 3

The Milagro Detector

In a sense it told him nothing that was new, but that was part of the attraction. It said what he would have said, if it had been possible for him to set his scattered thoughts in order.

George Orwell "1984"

Milagro employs the water Cherenkov detection technique which is widely used in particle physics experiments but is new to air shower detection. The use of water as a detection medium has several advantages: it is possible to construct a large instrument that can detect nearly every relativistic charged shower particle falling within its area by observing the Cherenkov radiation the particle produced. At a typical detector altitude, there are 4-5 times more photons in an extensive air shower than charged particles. In a conventional EAS array these photons are undetected. When these photons enter the water, they convert to electron-positron pairs or Compton scatter electrons which, in turn, produce Cherenkov radiation that can be detected. Consequently, Milagro has a very low energy threshold for an EAS array.[1]

This chapter presents the Milagro detector with its physical and electronic components, event reconstruction methodology and performance characteristics. For a more detailed description see references [4] and [3].

[1] Tibet is a conventional EAS array with energy threshold of several TeV. Such a low threshold could be achieved only due to its high altitude of 4300 m above sea level [28].

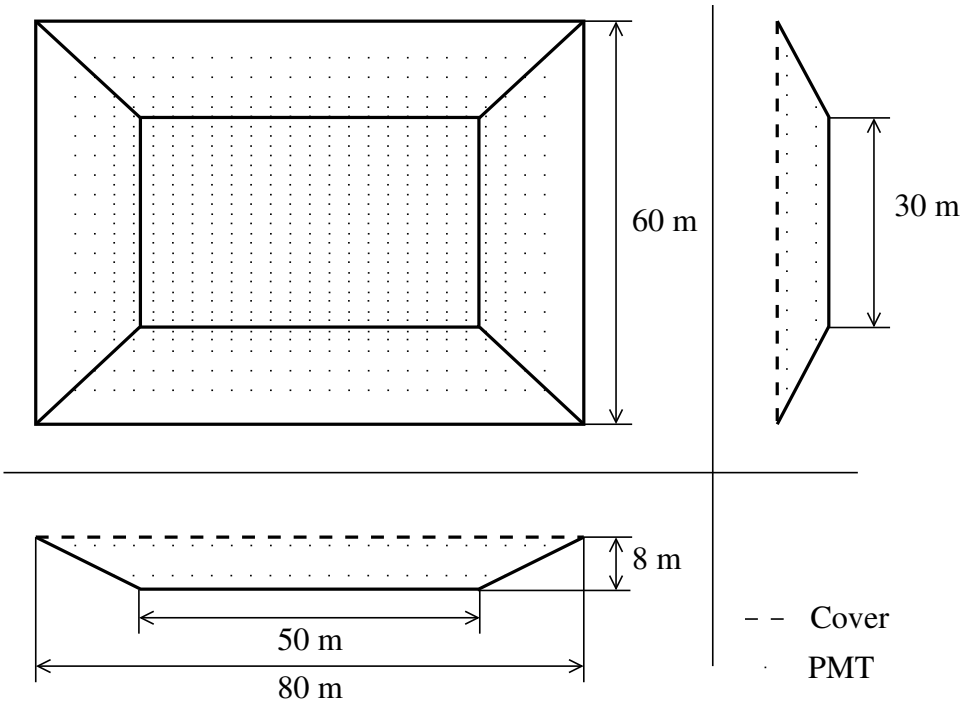

Figure 3.1: Schematic view of the Milagro pond.

3.1 General description.

The Milagro experiment is a part of what is now known as the Fenton Hill Observatory located at 35.88° North latitude and 106.68° West longitude in the Jemez Mountains near Los Alamos, New Mexico. At an altitude of $2650\ (m)$ above the sea level, its atmospheric overburden is about $750\ (g/cm^2)$. The Milagro detector, commissioned in June of 1999, records about 1700 extensive air shower events per second and is sensitive to gamma-showers with energies above $100\ (GeV)$. The duty-cycle of the detector is about 90%. The remaining time the detector is off for scheduled maintenance and/or when the environmental conditions do not warrant its operation (forest fires, loss of electrical power, etc). Milagro is built in a pre-existing 21 (metric) kilo-ton trapezoidal water reservoir (see figure 3.1) filled with pure water and instrumented with two horizontal planar layers of photomultiplier tubes (PMT). The top layer (AS) has 450 PMTs arranged on a $2.8 \times 2.8\ (m)$ grid, $1.5\ (m)$ below the water surface. The second layer (MU) has 273 PMTs located under about $6\ (m)$ of water on an interlaced $2.8 \times 2.8\ (m)$

grid. The photo-tube assembly is buoyant with the weight distribution allowing the photo-cathode to face upward when the assembly is submerged and anchored to the bottom of the pond with a Kevlar string. A reflecting conical baffle is installed in each PMT assembly to increase the light collection area and block horizontal and upward traveling light. The signals from the PMTs are delivered to the data-acquisition (DAQ) system for processing and recording. A high-density polypropylene liner and cover are installed to ensure water-tight bottom and walls of the pond and light impermeability of the whole detector.

3.1.1 Photomultiplier tube.

As was mentioned above, the Cherenkov radiation produced in the detector volume is detected by photo-multiplier tubes. Unlike conventional electro-vacuum tubes where electrons are injected into the tube due to thermal emission from its cathode, the injection of electrons (photoelectrons or PE for short) into the photo-tube is caused by light via the photo-electronic effect. Due to an externally applied voltage, the electrons travel towards the anode of the tube. However, on the way they encounter a dynode chain which plays the role of an amplifier. When electrons hit a dynode, secondary electrons are emitted which bombard the next dynode on their way to anode. In such a setup, enormous amplification can be reached with a relatively short dynode chain.

The amplification is not the only important parameter of a PMT, the others include:

Spectral Sensitivity: PMT should be sensitive to the wavelengths produced in the Cherenkov radiation.

Quantum efficiency: The ratio of the number of photoelectrons produced to the number of incident on photocathode photons is called quantum efficiency. Ideally it is equal to unity.

Time resolution: Time resolution of a PMT is thought to be limited by fluctuations in the photoelectron cascade development, especially on its early stages, especially between the photocathode and the first dynode. Lower light intensities generally lead to poorer time resolution.

Pre-pulsing: Pre-pulses on the PMT output are thought to occur when photoelectrons are produced by the first dynode, exposed to the incident light. Higher light intensities generally lead to higher pre-pulsing probability.

Late pulsing: Late pulses on the PMT output are thought to occur when all photoelectrons are reflected off the first dynode and re-enter the dynode chain producing a PMT pulse later than should have. Higher light intensities generally lead to lower late pulsing probability.

After pulsing: After pulses on the PMT output are thought to occur when residual gas molecules in the PMT are being ionized by the photoelectrons. The ions hitting the photocathode may cause secondary electron emission which would produce a secondary pulse. Higher light intensities generally lead to higher after pulsing probability.

Saturation: Saturation is the effect of decreased PMT amplification for higher intensity input. This is caused by inability of dynode chain to accelerate increased numbers of secondary electrons to sufficiently high energy.

After testing several PMT models, the Hamamatsu 8-inch 10-stage R5912SEL was selected for this application. It has relatively high quantum efficiency $(0.2 - 0.25)$ at wavelengths of $325 - 450\ (nm)$, good timing resolution ($2.7\ (ns)$ at 1PE), relatively low late/pre/after pulsing rates (about 5%) and relatively long linear response (up to about 75 PE). For a more detailed description of the PMT characteristics see references [4] and [33].

3.1.2 PMT pulse model, time over threshold.

Each PMT should provide information about the intensity of light incident on the PMT photocathode and the time when the light was registered. Since the total charge in a PMT pulse (number of photoelectrons) is proportional[2] to the incident light intensity, if the PMT pulse quickly charges a capacitor which is then slowly discharged via a load resistor, the total charge in the PMT pulse can be measured by the capacitor discharge time. This suggests that the time spent by a pulse over a preset threshold level is associated with the input light level[3] and is the main assumption of the time-over-threshold (ToT) method employed by Milagro. The PMT signal can be digitized with logical "one" when the PMT pulse exceeds the discriminator threshold and logical "zero" otherwise. A time-to-digital converter (TDC) attached to such a digital output will record the ToT. The beginning of the logical "one" provides the PMT pulse arrival time (T_{start}).

[2] Provided that the PMT saturation limit is not reached

[3] In fact, in this model ToT is proportional to the logarithm of the number of PEs.

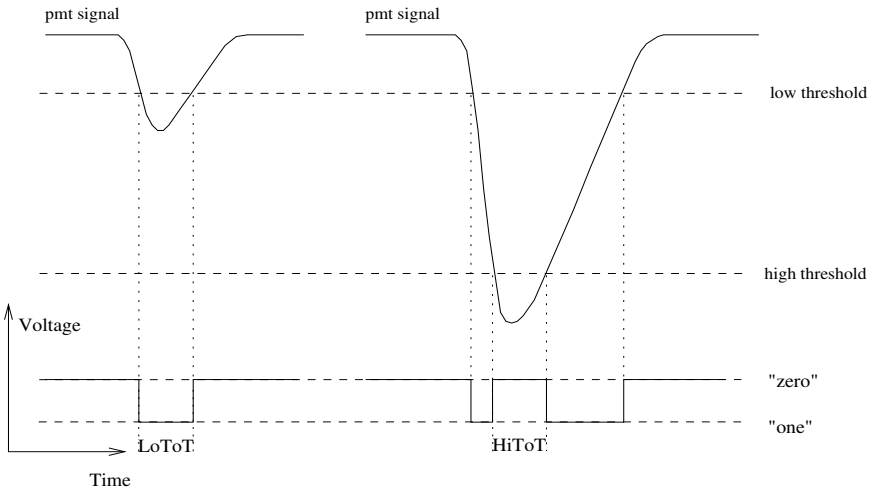

Figure 3.2: Illustration of HiToT, LoToT and edge-train

This method of measuring PMT pulse charge has several advantages over a conventional method when the PMT pulse is sent to an analog-to-digital converter (ADC). ADCs usually have narrow dynamic range, and are relatively slow and expensive devices.

Presence of pre- and after- pulses will distort the PMT pulse and it will not conform to the ToT model described above. Since strong pulses are more likely to be distorted, two thresholds, high (at the level of about 7 PE) and low (at about 1/4 PE) are introduced in the Milagro electronics. Large pulses will therefore cross both thresholds and the time-over-high-threshold (HiToT) is a much better measure of the pulse charge. Two close weak pulses will cross only the low threshold leading to excessively long time-over-low-threshold (LoToT), but absence of HiToT will flag such signals. To avoid use of two TDCs on a single PMT channel a logical exclusive OR operation is executed on LoToT and HiToT digital outputs leading to a train of raising and falling edges corresponding to each threshold crossing (see figure 3.2). If a PMT pulse is weak and only low threshold is crossed, the edge train contains only two edges (2-edge pulse), if both thresholds are crossed — four edges are recorded (4-edge pulse). Each TDC installed in Milagro is capable of recording up to 16 discriminator level crossings.

The train of edges with their TDC counts constitute the raw PMT signal.

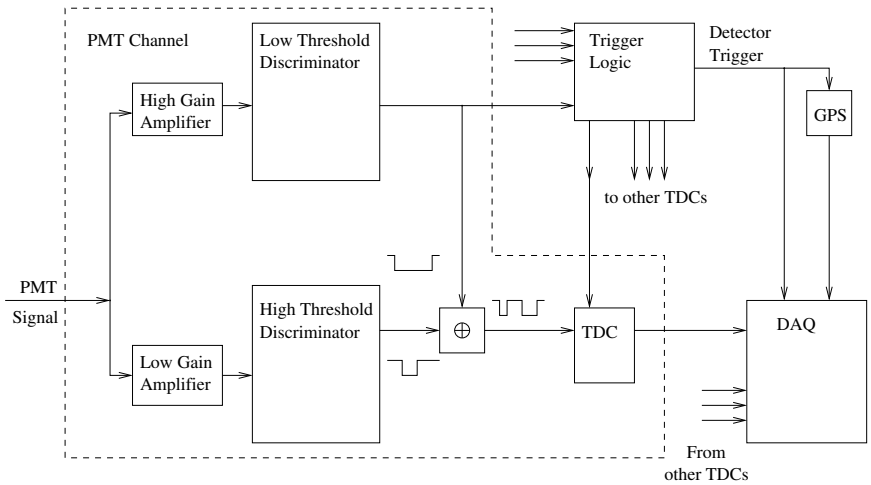

Figure 3.3: Block diagram of detector electronics

3.1.3 The Detector trigger.

All PMT channels in Milagro were manufactured as uniformly as possible, facilitating a simple multiplicity triggering logic. Indeed, as an extensive air shower front hits the detector a majority of PMT signals arriving at the outputs of the PMT channels will be in close coincidence with each other. The coincidence window was chosen to be $300\ (ns)$. If more than 60 PMT signals arrived within the window, a trigger was generated to the DAQ system. TDC modules are then read out with look back time of $1.5\ (\mu s)$ and the event is saved. It is desirable to trigger the detector at a low multiplicity requirement to lower the detector energy threshold. However, lowering it beyond 60 would increase the probability of triggering on muon events which is not the goal of the project. The generated trigger was sent to a Global Positioning System clock for absolute event time readout.

The TDC readouts from all PMTs channels and the trigger time constitute the raw event data and are sent for further software conditioning and processing.

3.2 Event Reconstruction.

The ultimate goal of any high energy gamma-ray telescope project is to study the properties of the objects which emitted the particles. This means that the characteristic param-

eters of the particles must be defined. Such parameters are: arrival time and direction, energy of the particle and its type[4]. (The shower impact parameter on the detector (core distance) is also an important parameter, which, however, is not related to the source.) As was mentioned in chapter 2, the particles of interest (primary) do not reach the detector level and disintegrate in the Earth's atmosphere creating extensive air showers of secondary particles. These secondary particles can be detected and constitute the observed event. The process of inferring the characteristics of the primary particle given the observed event is called event reconstruction. This is a multi-step process which requires deep understanding of the structure of the extensive air showers, detector hardware limitations and statistical nature of detection itself.

Currently, the signals from the PMTs in the top layer are used for shower direction determination and from the bottom — to distinguish photon and hadron induced air showers.

3.2.1 Pre-processing.

As was described above, the raw event data contains "edge-train information" registered by each PMT's TDC in the event. These data are not immediately suitable for primary particle characterization because the data is tainted by noise and systematic effects in the detector. Systematic effects include systematic off-sets of TDCs on different PMT channels (called time pedestals), TDC conversion factors (number of TDC counts per unit time) and delayed electronics response to lower PMT signals compared to higher ones (called electronic slewing). These systematic effects are studied with the help of the calibration system (see appendix B) and can be taken into account. Noise effects are random by nature and thus are more difficult to study and correct. Noise could be due to signals not associated with the main shower event (thermal/electronic/radioactive noise, non-shower particle hitting a PMT) or partially recorded edge-trains due to hardware constraints.

Noise filtering.

The main purpose of the edge-finding filter is to check that each PMT signal in an event conforms to the PMT signal model described in section 3.1.2. This should eliminate some thermal/electronic noise and partially recorded signals. The behavior of all PMT-

[4]major types are photon and hadron

electronic channels was studied in great detail and based on that, a set of criteria was developed which would select viable signals. (See [27].)

If a PMT signal does not satisfy the criteria, an attempt is made to convert the signal to the proper form. This is done by checking the number of edges, their polarity[5] and timing within the PMT signal. This filter is applied for each PMT in each event registered by the detector. After such filtering only about eight percent of all PMT signals are considered as unrecoverable and are discarded.

A completely different problem arises when valid PMT signals from non-shower particles are recorded with the main shower event. Presence of these signals will degrade the quality of event reconstruction as such signals do not carry any useful information about the shower. An idea of a method for filtration of such PMT signals was first proposed in [26] and [50] and then used in [23] and is based on the fact that PMT signals produced by a shower must be causally related, i.e. the time interval between any two PMT pulses multiplied by the speed of light in water should not be larger than the spatial distance between the PMTs. If a PMT signal is causally disconnected from the main shower event, it should be discarded. Unfortunately, at the moment of writing, this idea is not developed enough to be a part of the standard Milagro event reconstruction. This filter is applied to calibrated event.

TDC conversion factors.

TDC conversion factors were monitored with the help of the calibration system (see appendix B) and were found to be stable. Of most importance is the fact that all TDC modules operated at a common conversion rate of 2 counts per nanosecond with extremely high precision (see section B.2.1). This means that TDC counts can be used as time measure directly and there is no need to convert TDC counts to time for each PMT channel separately. This simplified the structure of the reconstruction code.

Raw to Calibrated event.

As was mentioned before, time response of PMT-electronic channels is dependent on the light intensity input. Since each PMT signal remaining after filtration conforms to the signal model, it is possible to correct for the effects of electronic delays to signals of varying strength. Based on that and auxiliary data obtained from the calibration process (see appendix B) the measured Time-over-Threshold (LoToT for weak signals

[5]polarity means correct sequence of rising/falling edges

and HiToT for strong ones) can be converted to PMT pulse arrival time (T_{start}) and number of photoelectrons emitted from PMT photocathode (PE). PMT coordinates and observed T_{start} and PE for each PMT in an event constitute a calibrated event and contain all information needed for event reconstruction.

3.2.2 Processing: angle, time, energy, type.

Even though at this processing stage all information obtainable from the PMTs is known, to reconstruct the particle characteristics the general structure of the showers and detector capabilities should be taken into account. For instance, since the PMT efficiency is only about 20 percent, there is no guarantee that the observed PMT signal is generated by the shower-front particles. Particles trailing the front may generate a PMT pulse too, but if the PMT happened to register the shower-front particles, the PMT pulse might be discarded as the ToT pulse model does not allow for more than a single PMT pulse in a shower event. Another example is that it is almost impossible to differentiate a low energy shower with small detector impact parameter from a high energy one with large impact parameter without knowledge of the shower structure. Thus, any method of event reconstruction must take into account detector and shower features.

Shower impact parameter.

As discussed in chapter 2 while the primary particle impact parameter does not provide any information about the source and the particle it created, it helps to understand the detector response to the shower produced.

Currently, the PMT PE distribution in the top layer in an event is analyzed to infer the location of the shower core. If the decision is made that the core is inside the Milagro pond, a PE-weighted average of PMT positions is used as the core location, while if it is decided that the core is outside the pond, it is placed at the distance of $50\ (m)$[6] from the center of the pond. The direction to the core, in the later case, is reconstructed by connecting the center of the pond with the $\sqrt{PE}$-weighted PMT positions. The decision of whether the core is inside or outside the pound is made based on the radial profile distribution of the number of PEs observed in the top layer PMTs.

The information inferred about the shower core is used in the sampling correction, angular and energy reconstruction. Full details of this method are described in [48].

[6]Computer simulations indicate that this is the most probable core distance for the showers which trigger the detector and have cores outside of the detector.

Sampling correction.

A great care has been take to eliminate systematic and random effect in the detector on event reconstruction. There is, however, a remaining one. This has to do with the finite probability of a PMT-electronic channel to detect light. Thus, the light, produced by the shower particles may be lost. The situation is complicated by the fact that showers have thickness and detection of trailing particles, if interpreted as the shower front, will degrade the quality of the angular reconstruction.

Luckily, knowing that the thickness of the shower is a function of impact parameter and that the number of particles in the shower falls off quickly with longitudinal distance from the shower front, the amount of light produced by the trailing particles is generally lower than by the front of the shower. Using that knowledge, the shower sampling effect can be observed based on measured light level at a given PMT and its distance from the shower axis and PMT pulse time can then be corrected to represent the shower front arrival time.

The Milagro sampling correction has been developed based only on number of PEs registered by a PMT in [35] and [22] and assumes that the shower arrived vertically when the impact parameter is equal to the core distance.

Time of event.

The time of an event is recorded as time of arrival of the PMT multiplicity trigger and is read from a GPS clock.

Angular reconstruction.

After detector sampling effects have been taken into account, the obtained PMTs' T_{start} times represent the best knowledge of the shower front. Knowing that the shower front forms a paraboloid, its main axis can be found and will give the arrival direction of the progenitor particle.

The algorithm utilized by Milagro first assumes that the shower arrived vertically and given the shower core position the curvature of the shower front can be "taken out" with what is called "curvature correction".[7] Following that, the shower direction is sought as the directrix of the plane fitted to the PMTs' T_{start} times ("time-lag" method) using a weighted χ^2-method. (See for instance [15].) The weights for the χ^2-fit are prescribed

[7]The functional form of the curvature correction was obtained from data and computer simulations in [35].

based on the number of PEs observed, as the quality of PMT time resolution increases with increase in the input light level [35].

Energy reconstruction.

Energy estimation is based on the amount of light deposited in the detector, distance to the core and the angle of the shower arrival and relies heavily on computer simulations of the shower propagation in the atmosphere and in the detector. At this time, primary particle energy is not being inferred in online data processing.

Primary particle type identification.

Because of their hadronic cores, air-showers generated by incident cosmic rays develop differently from purely electromagnetic cascades. The probability of photons to produce electron-positron pairs is several orders of magnitude higher than that of any process that might lead to muon production. In contrast, interactions of high energy hadrons with atmospheric nuclei lead to the production of charged pions which may decay into muons. In addition, multi-GeV hadronic particles may also survive to the ground. Simulations indicate that 80% of proton and only 6% of photon induced air showers that trigger Milagro will have at least one muon or hadron entering the pond.

Hadrons that reach the ground level and produce hadronic cascades in the detector or muons that penetrate to the bottom layer will illuminate a relatively small number of neighboring PMTs in that layer. Photon induced showers, on the other hand, generally will produce rather smooth light intensity distributions. Based on this simple observation a technique for identification of photon/hadron initiated showers has been formulated [51, 5] and according to computer simulations can correctly select about 90% of hadron initiated showers and about 50% of photon induced ones.

In a search for sources of high energy photons where hadron initiated showers represent unwanted background, the proposed identification scheme will allow increase of signal to noise ratio.

3.2.3 Post-Processing: Analysis Techniques.

After characteristics of the primary particle have been established further analysis has to be done, based on the concrete task under investigation. While many different tasks use similar techniques to answer stated questions, many employ unique methods. For

this reason the discussion of methods and algorithms used in the present work is delayed until chapter 4.

3.3 Detector performance and simulations.

After a device have been built and tuned, it is desirable to test its operation and gauge its response. Usually, this is done by comparing the device's response with the expected one given a known input signal. Needless to say that such a test is not possible to perform with Milagro due to unavailability of controllable test sources of high energy particles above the Earth's atmosphere, and one is forced to resort to computer simulations to estimate the detector performance. A simulated extensive air shower is sent to a simulated detector. The output of the simulated detector is sent for standard analysis and the result is compared with the input primary particle parameters.

The air shower simulation is done with the CORSIKA package [30] in the standard US atmosphere down to the detector level. The simulated shower front is then input into the GEANT-based detector simulation package. The output of this procedure is the Milagro "calibrated" event which can be sent for the standard particle characteristics reconstruction described earlier.

The most important parameters of the detector which are obtained based on computer simulations are angular resolution, energy response, impact parameter information, particle type identification quality and the detector's effective area.

Extensive air showers were generated over an energy range of $100\ (GeV)$ to $100\ (TeV)$, with zenith angles ranging from 0 to 45 degrees and core locations uniformly distributed over $1000\ (m)$ radius around the detector. Probability of triggering on a shower with energy outside the selected range or with higher zenith angles is very small which motivated the choice.

Angular resolution is characterized by the difference between the reconstructed and the known input particle direction. The overall accuracy of the angular reconstruction is believed to be 0.75°. The report [52] suggests that the energy of an incident particle can be reconstructed by Milagro with a fractional error of about 50% for particles with energies above $1\ (TeV)$.[8] Core location is reconstructed with error of about $20\ (m)$ if the shower lands on the detector and with error of about $50\ (m)$ otherwise.

[8]The same report also implies that since the quality of energy reconstruction relies on the quality of the core reconstruction, it is not possible to reach the 50% energy resolution with the current Milagro configuration. An upgrade with an outrigger array is necessary.

3.3.1 Effective area.

As was already mentioned, a shower event can be detected even if its core lands outside the detector. This leads to the notion of effective area as the area of imaginary detector which has perfect sensitivity to events which land on it and zero outside. This parameter describes sensitivity of the detector to particles of different type, energy and arrival direction.

If $N_0(k, E, \Theta)$ showers induced by particles of type k are simulated with core locations uniformly distributed over sufficiently large area A_0, local arrival directions $(\Theta, \Theta + \delta\Theta)$ and energies in the range of $(E, E + \delta E)$ then the effective area $A_k(E, \Theta)$ can be computed using the number of events $N_t(k, E, \Theta)$ which satisfy detector trigger condition in the simulations:

$$A_k(E, \Theta) = \frac{N_t(k, E, \Theta)}{N_0(k, E, \Theta)} A_0$$

Base simulations of proton and photon initiated showers $A_k(E, \theta)$ were obtained where θ is the local zenith angle only.

Chapter 4

Analysis Techniques

. . . if all others accepted the lie which the Party imposed — if all records told the same tale — then the lie passed into history and became truth.

George Orwell "1984"

4.1 Coordinates on the Celestial Sphere.

4.1.1 Celestial Sphere.

Because the stars are distant objects, they *appear* to lie on a sphere concentric with the Earth. This imaginary sphere is known as the Celestial Sphere. Astronomy uses a number of different coordinate systems to specify the positions of celestial objects and only those relevant to this work ones are discussed here.

The Celestial sphere has North and South Celestial poles as well as the celestial equator which are projected reference points of the same positions on the Earth's surface. A coordinate system which is based on these reference points on the celestial sphere is called the equatorial celestial coordinate system and is similar to the geographical coordinate system on the Earth's surface. A point on the celestial sphere can be described by two coordinates named "declination" (δ) and "right ascension" (α). The declination of a star is the analog of the latitude and is the angular distance from the star to the celestial equator. Right ascension is the analog of longitude with the zero of

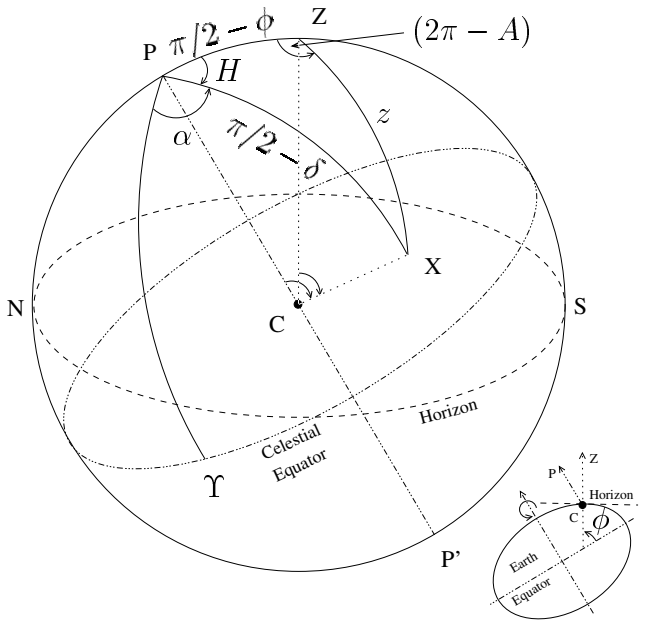

Figure 4.1: Definitions of main points and arcs on the Celestial sphere

right ascension at the point of vernal equinox.[1] Because of the Earth's rotation, right ascension and declination are not measurable directly by the ground-based observer and additional local to the observer coordinate system is introduced. The local coordinates are azimuth (A) and zenith distance (z) which can be converted to declination (δ) and hour angle (H). The list below defines the main points and arcs on the celestial sphere which are illustrated on figure 4.1.

C — Observer

CP — Axis parallel to the axis of rotation of the Earth passing through the observer C.

P, P' — North and South Celestial poles.

Z — Zenith, CZ is the continuation of the plumb line at observer C.

Horizon — intersection of a plane perpendicular to CZ at point C and the celestial sphere.

[1] Vernal equinox is the point where the Sun crosses the celestial equator on its south to north path through the sky and is stationary in space.

Local Reference Meridian — The arc PZP' of the great circle[2] containing points P, Z and P'.

N,S — North and South on the horizon as defined by the intersection of the great circle PZP' with the horizon.

$\overset{\smile}{PZ}$ — $\angle PCZ = \pi/2 - \phi$, ϕ is geographical latitude of the observer on the Earth.

Celestial Equator — intersection of the plane perpendicular to CP at point C with the Celestial sphere.

X — A celestial object on the sky (a star).

$\overset{\smile}{ZX}$ — Zenith distance (z) of the star X is the angle $\angle ZCX$.

$\angle PZX$ — Azimuth (A) of the star X is the dihedral[3] angle between the reference meridian and the ZCX plane measured from North towards East.

$\overset{\smile}{PX}$ — $\angle PCX = \pi/2 - \delta$, declination ($\delta$) of the star is the angle between $\overrightarrow{CX}$ and the Celestial equator.

$\angle ZPX$ — Hour angle (H) of the star is the dihedral angle between the reference meridian $\overset{\smile}{PZ}$ and the PCX plane measured from South towards West.

Υ — Point of vernal equinox

$P\overset{\smile}{\Upsilon}P'$ — Celestial reference meridian.

ΥPX — Right ascension (α) of the star is the dihedral angle between the ΥCP and XCP planes.

Given the definitions above, the law of cosines for the trihedron[4] applied to the spherical triangle ZPX two times yields the relationship between the (A, z) and (δ, H) coordinate systems:

[2] A great circle is a section of a sphere that contains a diameter of the sphere.

[3] The dihedral angle is the angle between two planes and is defined as the angle between their normal vectors.

[4] Three vectors with common vertex, often called a trihedral angle since they define three planes.

$$\begin{cases} \cos(\pi/2-\delta) = \cos z \cos(\pi/2-\phi) + \sin z \sin(\pi/2-\phi)\cos(2\pi - A) \\ \cos z = \cos(\pi/2-\delta)\cos(\pi/2-\phi) + \sin(\pi/2-\delta)\sin(\pi/2-\phi)\cos H \end{cases}$$

$$\begin{cases} \sin\delta = \sin\phi\cos z + \cos\phi\sin z\cos A \\ \tan H = \frac{-\sin z \sin A}{\cos\phi\cos z - sinz\sin\phi\cos A} \end{cases}$$

Since the local reference meridian is defined relative to the Earth, due to Earth's rotation the hour angle of a fixed in space point will grow with time (that is why it is called hour angle) while the local coordinate declination will remain constant. The hour angle of vernal equinox H_Υ links the local observer's coordinate system (H,δ) and the celestial equatorial coordinate system (α,δ) by providing the position of a fixed point (vernal equinox) on the celestial sphere in local coordinates: $\alpha = H_\Upsilon - H$. Hour angle of vernal equinox is also called the local sidereal time since it should be consistent with the observer's geographical longitude and the time required for one Earth's revolution, called a sidereal day. In contrast, the solar (or universal) day is defined as time between two consecutive appearances of the Sun on the local reference meridian. The solar day is longer than the sidereal one due to Earth's rotation and orbital motion around the Sun, though both days are divided into 24 hours.

4.1.2 J2000 reference.

Because the Earth's rotation is not uniform, its axis of rotation is not fixed in space and even its shape and relative positions on its surface are not fixed; because the introduced celestial equatorial coordinate system follows the motion of the Earth's pole and equator, the coordinate grid "drifts" on the surface of the celestial sphere.[5] Therefore, the introduced coordinate system provides only apparent right ascension and declination of the stars at the observation moment.

To solve this problem, all coordinates on the celestial sphere are reported relative to the position of the Earth's pole and equator at specified moments of time which are called epochs. Each epoch lasts for 50 years and the current one is defined with respect to the Earth's position at noon on the January 1, 2000. Thus, the apparent celestial coordinates need to be reduced to the J2000 reference.[6]

[5]These drifts include, but not limited to precession, nutation, celestial pole offset and polar motion.

[6]The major contribution to the "drift" of a celestial reference frame is due to the Earth's pole precession. Newcomb (Newcomb, S. Astron.J. **17**, 20 1897) derived the formulae for precession parameters

4.1.3 Diurnal parallax.

The Equatorial coordinate system had been defined under the assumption that the observer is located at its origin — the center of the Earth. All observing stations, however, are located on the Earth's surface. Due to Earth's rotation, the observing station moves and the observation of a celestial body is being made from different points in space. This will cause an apparent difference in position of celestial body when made at different moments of time. The effect is called *diurnal parallax*. For measurements of distant stars this has a negligible effect, but there could be a substantial diurnal parallax on objects inside the Solar system. Diurnal parallax on the Moon, for example, can be as large as 0.95°.

4.1.4 Milagro event coordinates.

The local hour angle and declination of an event on the celestial sphere are calculated from the zenith and azimuth which are provided by the event reconstruction section 3.2.2 (see also [19] for a discussion on local coordinates). Local sidereal time as well as the geographic coordinates of the detector can be obtained from a Global Positioning

---

$\zeta_A(t)$, $z_A(t)$ and $\theta_A(t)$ which specify the position of mean equinox and the equator of a date with respect to the mean equinox and equator of the initial epoch. Astronomical Almanac on page B18 supplies these parameters for the J2000.0 epoch in degrees:

$$\begin{aligned}\zeta_A &= 0.6406161T + 0.0000839T^2 + 0.0000050T^3\\ z_A &= 0.6406161T + 0.0003041T^2 + 0.0000051T^3\\ \theta_A &= 0.5567530T - 0.0001185T^2 - 0.0000116T^3\end{aligned}$$

where T stands for the time from the basic epoch J2000.0 in Julian centuries, $T = (\text{Julian Day} - 2451545.0)/36525$.

If subscript 0 refers to the coordinates at the epoch J2000.0 and no subscript to the epoch of the date, the transformation formulae are:

$$\left\{\begin{array}{rcl}\sin(\alpha - z_A)\cos\delta &=& \sin(\alpha_0 + \zeta_A)\cos\delta_0\\ \cos(\alpha - z_A)\cos\delta &=& \cos(\alpha_0 + \zeta_A)\cos\theta_A\cos\delta_0 - \sin\theta_A\sin\delta_0\\ \sin\delta &=& \cos(\alpha_0 + \zeta_A)\sin\theta_A\cos\delta_0 + \cos\theta_A\sin\delta_0\end{array}\right.$$

$$\left\{\begin{array}{rcl}\sin(\alpha_0 + \zeta_A)\cos\delta_0 &=& \sin(\alpha - z_A)\cos\delta\\ \cos(\alpha_0 + \zeta_A)\cos\delta_0 &=& \cos(\alpha - z_A)\cos\theta_A\cos\delta + \sin\theta_A\sin\delta\\ \sin\delta_0 &=& -\cos(\alpha - z_A)\sin\theta_A\cos\delta + \cos\theta_A\sin\delta\end{array}\right.$$

System receiver which facilitates the conversion from local to celestial coordinates. In Milagro, the coordinates of reconstructed events are reduced from the epoch of date to the J2000 reference in real time and are saved to disk for further processing.

As will be clarified in the sections to follow, the signal processing method employed in this work expects the event coordinates in a local reference frame. Thus, even though the events are saved in J2000 reference which seems to be convenient, the conversion to J2000 must be undone during the offline/online signal processing.[7]

4.2 Sky Mapping.

In counting-type astrophysical experiments, the brightness of a particular point in the sky is characterized by the number of events observed from that point during the exposure time. Such experiments measure the density of events on the surface of the Celestial sphere. Therefore, the procedure used to generate the sky images (projections of a sphere onto a plane surface) should conserve the density of events. To meet this requirement an equal area projection of a sphere onto a plane must be used. This requirement, however, is not enough to uniquely fix the projection, and several different projections are available. It is crucial to understand that any area preserving projection is not conformal and might distort the distances and/or directions on the map. That is why different area preserving mappings should be used for different tasks. For example, the sinusoidal projection[8] has minimal distortions near the equator and that is why is it very convenient for galactic plane studies. When the same mapping is used for an object far from the galactic equator, linear distortions become significant.

[7] It would be prudent to save the local hour angle and declination of the registered events during the online realtime processing. This would force the coordinates of celestial bodies which are known in J2000 from catalogues, to be reduced to epoch of date then to be reduced to the apparent Right Ascension-Declination by application of the parallax correction (if necessary) then to local hour angle-declination using local time. This approach would save some computer time during online and offline data processing because the Milagro event rate is above $1\ (kHz)$ and the detector angular of resolution (several tenths of a degree) allows for rare (once per several seconds (in 24 seconds the Earth rotates on 0.1° of arc)) computation of local coordinates of the celestial bodies.

[8] The *Sinusoidal Equal Area Projection* is defined as:

$$\begin{cases} x = l\cos b \\ y = b \end{cases}$$

where (l, b) are galactic coordinates

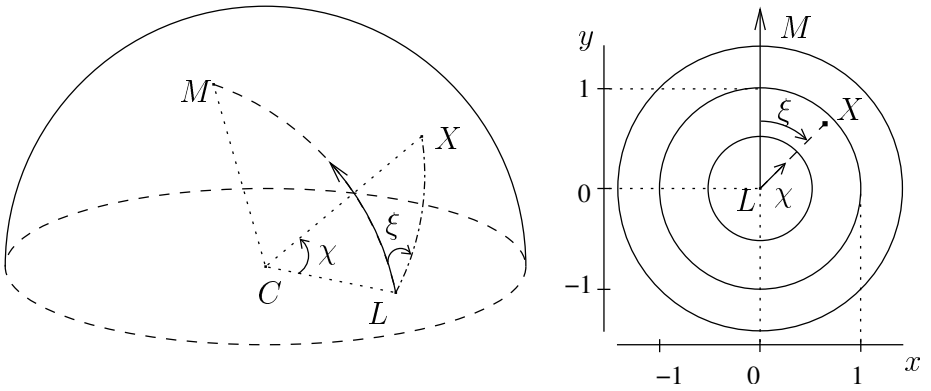

Figure 4.2: Concept of the auxiliary coordinate system on the Celestial sphere centered on L (left) and corresponding sky projection (right). The "y"-axis of the sky projection always points to a pole M and the circles are the lines of $\chi = const$ at $\chi = \pi/6,\ \pi/3,\ \pi/2$.

In addition to the previously discussed constraints, all events with identical spatial orientation with respect to the point of interest must be mapped into a unique location. This is especially important if the point of interest moves on the Celestial sphere. However, a simple algebraic difference in Celestial coordinates of any two points does not define their relative spatial orientation. One way to address this problem is to introduce auxiliary coordinates on the Celestial sphere: an analog of latitude (χ) and longitude (ξ) which are measured with respect to the preselected point. (See figure 4.2 and appendix C for the definition of the $(\chi - \xi)$ coordinate system.) Using these coordinates, the sky image centered on the selected point can be produced with the help of the Azimuthal Equal Area Projection in the polar case defined as:

$$\begin{cases} x = \sqrt{2(1-\cos\chi)}\sin\xi \\ y = \sqrt{2(1-\cos\chi)}\cos\xi \end{cases} \tag{4.1}$$

This mapping not only satisfies the above requirements, it has several other important features such as conservation of the directions as seen from its origin, the locus of points equidistant from the center of the mapping is projected into a circle (see figure 4.2) and it can be easily oriented along the lines of the Earth's magnetic field.

4.3 Statistical Nature of Signal Establishment.

In a typical counting type astrophysical experiment during observation time t_1 the number of events observed due to some physical process is N_1. Assuming that an event contains no information about any other one, the number of observed events is a random variable which is distributed according to the Poisson distribution.[9] In other words, the probability to observe exactly N_1 events during time t_1 is given by:

$$p(N_1;\lambda) = \frac{(\lambda t_1)^{N_1}}{N_1!} e^{-\lambda t_1}$$

where λ has a meaning of average event rate.

However, an observed event could be due to either a source or background. Since the average count rate due to background is not known, based on this one observation it is not possible to decide whether there were any "source" events observed. Therefore without altering the conditions of the experiment a second measurement N_2 during t_2 is made where it is believed that all observed events are due to background only. Now, a decision should be made as to whether there is a difference between these numbers which can be interpreted as a detection of a source. Since the observed N_1 and N_2 are random numbers, this question should be approached from the statistical point of view. Note that a statistical test cannot verify that a given hypothesis[10] is true or false, but can only suggest which of the two or more hypotheses is the more plausible explanation of the observation.

4.3.1 General test construction.

Suppose[11] that a result of an observation is described by the values of n variables:

$$\{x\} = x_1, x_2, \ldots, x_n$$

The $\{x\}$ may represent outcomes of n repeated measurements made under identical conditions or a sample from a population. All possible outcomes of a measurement are

[9] Some of the properties of the Poisson distribution are discussed in appendix A

[10] Any statement concerning the unknown distribution of a random variable is called a statistical hypothesis.

[11] This subsection is based on the section II of the paper [40].

said to form a sample space W. A hypothesis about the origin of the observed events H defines the probability of occurrence of every possible observation

$$p(x_1, x_2, \ldots, x_n)$$

and thus, the probability that the observed event will fall into some region w of all possible outcomes is

$$P(w) = \int_w p(x_1, \ldots, x_n)\, dx_1 \ldots dx_n$$

Of course, $P(W) = 1$. Different hypotheses H with their corresponding probability distributions $p(\{x\})$ will be endowed by the same subscripts, such as H_0 and p_0.

A statistical test is formulated so that all prior knowledge strongly supports H_0 called the null hypothesis. Hypothesis H_0 is rejected if the observed event $\{x\}$ lies within a certain critical region w_c and accepted or doubted otherwise. Such a formulation of a test implies that it is possible to reject H_0 when, in fact, it is true. The danger of falsely rejecting the null hypothesis is characterized by the error of the first kind or significance ξ_c and:

$$\xi_c = P_0(w_c) = \int_{w_c} p_0(x_1, \ldots, x_n)\, dx_1 \ldots dx_n$$

The choice of the value of ξ_c depends on the penalty for making the error, therefore, the risk ξ_c must be set in advance, not after the results of a measurement are available. Even though the error of the first kind can be chosen to be arbitrary small, the equation $\xi_c = P_0(w_c)$ has, in general, infinitely many solutions on configuration w_c with the same level of significance ξ_c.

Since H_0 is being tested, it implies the existence of an alternative hypothesis H_1 or there would be no question about H_0.[12] But, as the risk ξ_c is required to be smaller and smaller, the risk ζ of accepting H_0, when H_1 is true may increase. This error is called the error of the second kind and is given by:

$$\zeta = P_1(W \setminus w_c) = \int_{W \setminus w_c} p_1(x_1, \ldots, x_n)\, dx_1 \ldots dx_n$$

The two errors ξ and ζ can rarely be eliminated, and in some cases it is more impor-

[12] While it may not be constructive, "H_0 is false" is an admissible alternative hypothesis.

tant to avoid the first, in others — the second. When H_0 and H_1 are specified it is the choice of the critical region which allows control of the errors.

A prescription to resolve the apparent vagueness in the provided formulation of the test was proposed in [40]. It is proposed that given the two hypotheses H_0 and H_1 and the desired risk level ξ_c, the corresponding best critical region w_c^{best} minimizes the error ζ.

If based on the outcome of the experiment, the observed x is inside of the critical region w_c^{best}, it is said that the null hypothesis is rejected in favor of the alternative one with significance ξ_c and power $(1-\zeta)$. If, however, $x \notin w_c^{best}$, it is said that the null hypothesis is not rejected in favor of the alternative one with significance ξ_c and power $(1-\zeta)$.

Often, however, rather than use the full data sample $\{x\}$ it is convenient to define a test statistic[13] U. Each hypothesis for the distribution of $\{x\}$ will determine a distribution for U, and a specific range of values of U will be mapped to a critical region in W-space. In constructing U one attempts to reduce the volume of data without loss of the ability to discriminate between different hypotheses.

4.3.2 Testing a composite hypothesis.

If the hypothesis being tested does not specify the probability of occurrence of every possible observation, it is called a composite hypothesis. It will be assumed that the composite hypothesis depends on an unspecified parameter λ as:

$$p(x_1, x_2, \ldots, x_n; \lambda)$$

As before, the null hypothesis should be rejected if the observed event lies within a critical region w_c.

In order to control the error of the first kind ξ, the critical region must satisfy:

$$\xi_c = P_0(w_c) = \int_{w_c} p_0(x_1, \ldots, x_n; \lambda_0)\, dx_1 \ldots dx_n$$

for every value of the parameter λ_0. In other words, the error of the first kind should not depend on the unknown value of the parameter λ_0. If such critical regions exist, it is necessary to choose the best one which minimizes the error of the second kind. It

[13] Statistic is a random variable which is a function of the observed sample of data.

should be noted that the error of the second kind may, in general, depend on the values λ_0 and λ_1 of the alternative hypothesis $p_1(x_1, \ldots, x_n; \lambda_1)$.

This problem has been solved in [40] for a special class of the null hypotheses when $p_0(\{x\}; \lambda_0)$ is infinitely differentiable function of λ_0 in every point $\{x\} \in W$ and the function $p_0(\{x\}; \lambda_0)$ satisfies the equation:

$$\frac{d\phi}{d\lambda_0} = A + B\phi, \quad \phi = \frac{d \ln p_0(\{x\}; \lambda_0)}{d\lambda_0} \tag{4.2}$$

and the coefficients A and B are functions of λ_0 only and do not depend on $\{x\}$. It is shown in [40] that the best critical region w_c^{best} is constructed of pieces of hypersurfaces $\phi = C = const$ such that:

$$\frac{p_1(\{x\}; \lambda_1)}{p_0(\{x\}; \lambda_0)} > q, \quad \forall \{x\} \in w_c^{best} \tag{4.3}$$

where q is a constant whose value is governed by w_c^{best} chosen subject to constraint:

$$\xi_c \int_{\{x\} \in W \cap \phi = C} p_0(\{x\}; \lambda_0) dx = \int_{\{x\} \in w_c^{best} \cap \phi = C} p_0(\{x\}; \lambda_0) dx \tag{4.4}$$

4.3.3 Significance of a measurement.

In as much as an attempt is being made to identify the presence of a source, the null-hypothesis H_0 will be formulated in the following way:

> *The source is not present. The results N_1 and N_2 of two independent observations come from a single Poisson distribution with parameter λ.*

with an alternative hypothesis H_1 that:

> *The independent counts N_1 and N_2 come from Poisson distributions with different parameters λ_1 and λ, correspondingly.*

Mathematically, if H_0 is true the probability $p_0(N_1, N_2; \lambda)$ to observe N_1 and N_2 is:

$$p_0(N_1, N_2; \lambda) = \frac{(\lambda t_1)^{N_1}}{N_1!} e^{-\lambda t_1} \frac{(\lambda t_2)^{N_2}}{N_2!} e^{-\lambda t_2}$$

while, if H_1 is true the probability $p_1(N_1, N_2; \lambda_1, \lambda)$ is:

$$p_1(N_1, N_2; \lambda_1, \lambda) = \frac{(\lambda_1 t_1)^{N_1}}{N_1!} e^{-\lambda_1 t_1} \frac{(\lambda t_2)^{N_2}}{N_2!} e^{-\lambda t_2}$$

where the values of λ and λ_1 are unspecified and the only requirement is that $\lambda_1 \neq \lambda$.

The formulated H_0 satisfies the conditions of a theorem presented in [40] which states that there exists the best critical region w_c^{best} corresponding to significance ξ_c independent of the value of the parameter λ.

Following the algorithm for construction of the best critical region from [40], the equations (4.2) and (4.3) become:

$$\phi = N_t = N_1 + N_2 = const$$

$$\frac{p_1}{p_0} > q \;\; \Rightarrow \;\; \left(\frac{\lambda_1}{\lambda}\right)^{N_1} e^{-(\lambda_1 - \lambda)t_1} \geq q \;\; \Leftrightarrow \;\; \left[\begin{array}{ll} N_1 \geq N_\xi, & \lambda_1 > \lambda \\ N_1 \leq N_\xi, & \lambda_1 < \lambda \end{array} \right.$$

It is thus clear that the best critical region for testing $\lambda_1 = \lambda$ against $\lambda_1 \neq \lambda$ does not exist, however, it does exist for testing $\lambda_1 = \lambda$ against $\lambda_1 > \lambda$ or $\lambda_1 < \lambda$ separately.

The value N_ξ corresponding to the error of the first kind ξ is found as the solution of the equation (4.4):

$$\left[\begin{array}{ll} \xi \sum_{k=0}^{N_t} p_0(k, N_t - k; \lambda) = \sum_{k=N_\xi}^{N_t} p_0(k, N_t - k; \lambda), & \lambda_1 > \lambda \\ \\ \xi \sum_{k=0}^{N_t} p_0(k, N_t - k; \lambda) = \sum_{k=0}^{N_\xi} p_0(k, N_t - k; \lambda), & \lambda_1 < \lambda \end{array} \right.$$

Immediately, it should be noted that the solution N_ξ does not depend on the values of the parameters λ_1 and λ and the best critical region exists for the H_0 with regard to all alternative hypotheses H_1. After explicitly writing the probability $p_0(N_1, N_2)$, one arrives to the following equation on N_ξ:

$$\left[\begin{array}{ll} \xi = (1+\alpha)^{-N_t} \sum_{k=N_\xi}^{N_t} C_{N_t}^k \alpha^k, & \lambda_1 > \lambda \\ \\ \xi = (1+\alpha)^{-N_t} \sum_{k=0}^{N_\xi} C_{N_t}^k \alpha^k, & \lambda_1 < \lambda \end{array} \right| \quad \alpha = t_1/t_2 > 0, \quad C_n^m = \frac{n!}{m!(n-m)!}$$

The error of the second kind ζ can be computed as:

$$\left[\begin{array}{ll} \zeta = \sum_{N_t=0}^{\infty} \sum_{k=0}^{N_\xi - 1} p_1(k, N_t - k; \lambda_1, \lambda), & \lambda_1 > \lambda \\ \zeta = \sum_{N_t=0}^{\infty} \sum_{k=N_\xi+1}^{N_t} p_1(k, N_t - k; \lambda_1, \lambda), & \lambda_1 < \lambda \end{array}\right.$$

$$\left[\begin{array}{ll} \zeta = e^{-\lambda_1 t_1 - \lambda t_2} \sum_{N_t=0}^{\infty} (\lambda t_2)^{N_t} \sum_{k=0}^{N_\xi - 1} \frac{(\frac{\lambda_1 t_1}{\lambda t_2})^k}{k!(N_t - k)!}, & \lambda_1 > \lambda \\ \zeta = e^{-\lambda_1 t_1 - \lambda t_2} \sum_{N_t=0}^{\infty} (\lambda t_2)^{N_t} \sum_{k=N_\xi+1}^{N_t} \frac{(\frac{\lambda_1 t_1}{\lambda t_2})^k}{k!(N_t - k)!}, & \lambda_1 < \lambda \end{array}\right.$$

The explicit solution for the critical region is needed if an ability to compute the error of the second kind ζ is desired. As expected, this error will depend on the values of the parameters λ and λ_1 of the alternative hypothesis H_1. It is, however, possible to decide if the null hypothesis should be rejected or not without the explicit solution. To do this, N_ξ must be set to N_1 and ξ must be computed from the equations above using $N_t = (N_1 + N_2)$. If it is found that the ξ obtained in this fashion is smaller than the critical value ξ_c, the null hypothesis should be rejected and should not be rejected otherwise.

As will be explained below, because the procedure for setting an upper limit is based on the error of the second kind ζ, expression for which is not known in a closed form, a "practical" statistic which was proposed in [34] is considered in this work:

$$U = \frac{N_1 - \alpha N_2}{\sqrt{\alpha(N_1 + N_2)}} \qquad \alpha = t_1/t_2 > 0 \tag{4.5}$$

The denominator in (4.5) is the maximum likelihood estimate on dispersion of $(N_1 - \alpha N_2)$ given the null hypothesis is true. Then, under the null hypothesis the mean value of the statistic U is zero and the dispersion is equal to unity. If both N_1 and αN_2 have not deviated far from the expected value of λt_1, then N_1 and αN_2 can be regarded as coming from Gaussian distributions with the means equal to λt_1 and dispersions λt_1 and $\alpha \lambda t_1$ correspondingly (See discussion on Gaussian limit to Poisson distribution in appendix A.). Hence, the values of the statistic U are distributed according to a Gaussian distribution with zero mean and unit variance $p_0(u) = \frac{1}{\sqrt{2\pi}} e^{-\frac{u^2}{2}}$. This statement is valid

for all $u \leq u_0$[14]:

$$|u| \leq |u_0| << \min\left(\sqrt[6]{36\alpha(1+\alpha)^2(N_1+N_2)}, \sqrt[6]{36\alpha^{-3}(1+\alpha)^2(N_1+N_2)}\right) \quad (4.6)$$

If, however, the $H_1(\lambda_1)$ is true, the U will have approximately Gaussian distribution with unit dispersion and shifted mean:

$$p_1(\lambda_1) = \frac{1}{\sqrt{2\pi}} e^{-\frac{(u-u_1(\lambda_1))^2}{2}}$$

where $u_1(\lambda_1)$ is monotonically increasing function of λ_1 and is equal to the average value of U computed when $H_1(\lambda_1)$ is true.

$$u_1(\lambda_1) \simeq \frac{(\lambda_1 - \lambda)t_1}{\sqrt{(\alpha\lambda_1 + \lambda)t_1}} \approx \frac{\lambda_1 - \lambda}{\sqrt{\lambda(1+\alpha)}}\sqrt{t_1}$$

Let us define the critical range of values of the statistic U corresponding to significance ξ_c in the following way (see figure 4.3 for an illustration):

If $\lambda_1 > \lambda$**:** $u > u_c$, $\xi_c = \int_{u_c}^{+\infty} p_0(u)du$.

If $\lambda_1 < \lambda$**:** $u < u_c$, $\xi_c = \int_{-\infty}^{u_c} p_0(u)du$.

For the reasons of tradition, in astrophysics, it is customary to report the level of significance not as probability ξ_c, but as "number of sigmas" u_c which motivated the choice of statistic. The table 4.1 provides the translation between the critical value u_c and the significance ξ_c with the approximation error on ξ not exceeding $\frac{1}{\sqrt{2\pi}} \int_{u_0}^{+\infty} e^{-\frac{u^2}{2}} du$.

4.3.4 Setting an upper limit.

Some times, when the null hypothesis can not be rejected based on the results of a test and there are several alternative hypotheses available, it is meaningful to ask the question of which of the alternatives provides error of the second kind larger than ζ_u. For instance, in the case considered here, there are many alternative hypothesis parametrized

[14]The value of u_0 is obtained by substituting k with $N_{1,2}$ and λ with corresponding maximum likelihood estimates $\frac{N_1+N_2}{t_1+t_2}t_{1,2}$ into the equation (A.2).

$\lvert u_c \rvert$	ξ_c
1.0	$1.587 \cdot 10^{-1}$
2.0	$2.275 \cdot 10^{-2}$
3.0	$1.350 \cdot 10^{-3}$
3.5	$2.326 \cdot 10^{-4}$
4.0	$3.167 \cdot 10^{-5}$
4.5	$3.398 \cdot 10^{-6}$
5.0	$2.867 \cdot 10^{-7}$

Table 4.1: Significance ξ_c and corresponding critical value u_c.

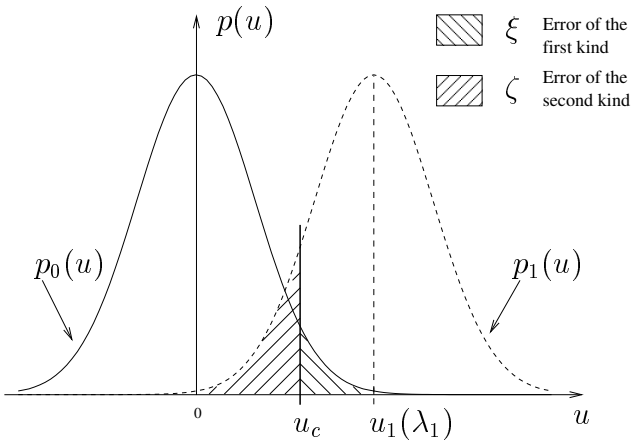

Figure 4.3: Critical region illustration for the statistic U when $\lambda_1 > \lambda$.

by the values of λ_1[15]. Since each alternative hypothesis $H_1(\lambda_1)$ defines a probability distribution $p_1(u, \lambda_1)$ in the sample space, the error $\zeta(\lambda_1)$ is (see figure 4.3 for an illustration):

If $\lambda_1 > \lambda$**:** $\zeta(\lambda_1) = \int_{-\infty}^{u_c} p_1(u, \lambda_1) du$.

If $\lambda_1 < \lambda$**:** $\zeta(\lambda_1) = \int_{u_c}^{+\infty} p_1(u, \lambda_1) du$.

For the case of $\lambda_1 > \lambda$, $\zeta(\lambda_1)$ is monotonically decreasing function of λ_1. Therefore, λ_1^u corresponding to the largest allowed error ζ_u is called the upper limit on λ_1 ($\zeta(\lambda_1^u) = \zeta_u$). It means that the probability of making the error of the second kind by accepting the null hypothesis when in fact one of the alternative hypotheses with parameter λ_1 ($\lambda_1 > \lambda_1^u > \lambda$) is true is less than ζ_u. For a discussion on the upper limit construction procedure, please, see appendix E.

4.4 Background estimation.

One method of searching for a source is by counting the number $N_{on}(\Theta)$ of events from local direction $(\Theta; \Theta + d\Theta)$ while it was exposed to a source region Ω on the sky (the "on-source" bin) and comparing it with the number of background events $N_{on}^b(\Theta)$ expected from this region. The number of background events expected from the "on-source" region is given by:

$$N_{on}^b(\Theta) = \int_{\Theta} [1 - \phi(\Theta', t)] \, R_b(\Theta', t) d\Theta' dt$$

where $R_b(\Theta, t)$ is background event rate from local direction Θ at an observation moment t and

$$\phi(\Theta, t) = \begin{cases} 0, & (\Theta, t) \in \Omega \\ 1, & (\Theta, t) \notin \Omega \end{cases}$$

Since the function $R_b(\Theta, t)$ is not known *a priori*, it should be determined from the observed data. To accomplish that one is forced to introduce some assumptions about the structure of $R_b(\Theta, t)$. Probably, the most natural simplification comes from the assumptions that the background events are distributed uniformly on the sky (their distri-

[15]Remember that λ_1 is not a source strength, but merely the average event count rate due to possible presence of a source.

bution is independent of local coordinates Θ)[16] and that the conditions of the experiment (hardware, software, field of view, everything) remain constant (at least for periods of time long enough to allow measurement of $R_b(\Theta, t)$ to the necessary accuracy). Then, $R_b(\Theta, t)$ can be factorized:

$$R_b(\Theta, t) = G(\Theta) \cdot R_b(t)$$

where $R_b(t)$ is overall event rate due to background only and is independent of local coordinates and $G(\Theta)$ is the detection efficiency of the instrument and does not depend on time. Thus, the problem of determining $R_b(\Theta, t)$ is reduced to the one of $R_b(t)$ and $G(\Theta)$.

Knowing that the number of background events expected from any point on the sky at some time is:

$$dN^b(\Theta, t) = R_b(\Theta, t)d\Theta dt = R_b(t)G(\Theta)d\Theta dt$$

the total number of background events $N^b_{out}(\Theta)$ which are to be observed within some large time T from the local direction Θ outside of the source region[17] [18] and the total rate $R^b_{out}(t)$ from all viewed sky except for the source region are:

$$\begin{cases} N^b_{out}(\Theta) = \int_T \phi(\Theta, t)G(\Theta)R_b(t)dt &= G(\Theta)\int_T \phi(\Theta, t)R_b(t)dt \\ R^b_{out}(t) = \int \phi(\Theta, t)G(\Theta)R_b(t)d\Theta &= R_b(t)\int \phi(\Theta, t)G(\Theta)d\Theta \end{cases}$$

The functions $N^b_{out}(\Theta)$ and $R^b_{out}(t)$ are not distorted by the presence of any source (by assumption) and can be measured directly. Then, the set of equations can be solved for $R_b(t)$ and $G(\Theta)$ numerically with the initial approximation to $R_b(t)$ taken from the observed total event rate.

Thus, the expected number of background events in the source region can be found from:

[16] Charged particles which form the background are isotropized by galactic and inter-galactic magnetic fields.

[17] The outside region should not contain any known source in the field of view of the detector. The events from other sources and their source regions should be removed from the analysis as they would bias the background estimation.

[18] Due to the Earth's rotation, the local direction Θ will fall within the source region Ω at some times and outside at the others. If for a particular source region Ω, Θ is exposed to Ω only, N^b_{on} can not be estimated with the presented method.

$$N^b_{on}(\Theta) = \int_\Theta \left[1 - \phi(\Theta', t)\right] R_b(t) G(\Theta') d\Theta' dt$$

4.5 Performing test for a source presence.

If $N_{on}(\Theta)$ and $N^b_{on}(\Theta)$ are the number of events observed from the local direction Θ inside of some bin Ω in the on-source and off-source measurements respectively, the value of the statistic U from (4.5) is:

$$U(\Theta) = \frac{N_{on}(\Theta) - N^b_{on}(\Theta)}{\sqrt{N^b_{on}(\Theta) + \alpha(\Theta) N_{on}(\Theta)}}$$

where

$$N_1 = N_{on}(\Theta) \quad \alpha N_2 = N^b_{on}(\Theta) \quad \alpha(\Theta) = N^b_{on}(\Theta)/N^b_{out}(\Theta)$$

Since the measurements made from different local directions Θ are independent, all measurements from Θ's which fall into the bin Ω can be easily combined to obtain compounded statistic of the measurement in the bin Ω:

$$U(\Omega) = \frac{\sum_\Theta N_{on}(\Theta) - \sum_\Theta N^b_{on}(\Theta)}{\sqrt{\sum_\Theta N^b_{on}(\Theta) + \sum_\Theta \frac{N^b_{on}(\Theta) N_{on}(\Theta)}{N^b_{out}(\Theta)}}} = \frac{N_{on}(\Omega) - N^b_{on}(\Omega)}{\sqrt{N^b_{on}(\Omega) + \sum_\Theta \frac{N^b_{on}(\Theta) N_{on}(\Theta)}{N^b_{out}(\Theta)}}} \quad \Theta \in \Omega \tag{4.7}$$

The critical value u_c of the statistic $U(\Omega)$ is set to five. If $U(\Omega)$ is greater than five, the null hypothesis will be rejected and it will be said that the observed counts must have come from an astrophysical source. A measurement of the source strength can be performed.

If the observed $U(\Omega)$ is less than five, the null hypothesis will not be rejected and an upper limit corresponding to 2.3% error of the second kind will be made. A measurement of the source strength can be performed only if it is known (from other experiments) that the source exists.

It should be remembered for probability interpretation according to the table 4.1 to be valid, the inequality (4.6) needs to be satisfied and for $u_c = 5$ and typical value of $\alpha = 1/15$ the number of events observed in the observation bin $N_{on}(\Omega)$ should be about $2 \cdot 10^6$.

4.6 Gamma-Ray flux measurement.

Given the detector response to particles of different types and assumed source features, it is possible to predict the number of events $\hat{N}(\tilde{\Omega})$ to be observed in the bin $\tilde{\Omega}$ due to the source. Then, $\hat{N}(\tilde{\Omega})$ can be compared with the actually observed number $N(\tilde{\Omega})$ and some statement regarding the assumed source features can be made. Indeed, let $P(k, \tilde{k}, E, \tilde{E}, \Theta, \tilde{\Theta}, \vec{r}, \vec{R})$ be the probability that the detector registers a particle of type k coming from local direction Θ with energy E distance $\vec{r}$ from the apparatus and reconstruction output information about the particle is $\tilde{k}$, $\tilde{\Theta}$, $\tilde{E}$, $\vec{R}$. Then, the total number of events due to particles of type k to be observed from a region $\tilde{\Omega}$ is:

$$\hat{N}_k(\tilde{\Omega}) = \sum_{\tilde{k}} \int_{\tilde{\Theta}\in\tilde{\Omega}} P(k, \tilde{k}, E, \tilde{E}, \Theta, \tilde{\Theta}, \vec{r}, \vec{R}) F(k, E, \Theta) T(\Theta)\, dE\, d\tilde{E}\, d\Theta\, d\tilde{\Theta}\, d\vec{r}\, d\vec{R}$$

where $F(k, E, \Theta)$ is the number of particles of type k with energy E emitted by the source in local direction Θ per unit area per unit time, $T(\Theta)$ is the time during which the source is located in local direction Θ. The integration is performed over all possible values of energies E and $\tilde{E}$, all possible distances $\vec{r}$ and $\vec{R}$ and all directions in the field of view Θ, but $\tilde{\Theta} \in \tilde{\Omega}$.

The integration over core distances $\vec{r}$, $\vec{R}$, measured energy $\tilde{E}$ and the summation over identified particle type $\tilde{k}$ can be performed:

$$P(k, E, \Theta, \tilde{\Theta}) = \sum_{\tilde{k}} \int P(k, \tilde{k}, E, \tilde{E}, \Theta, \tilde{\Theta}, \vec{r}, \vec{R})\, d\tilde{E}\, d\vec{r}\, d\vec{R}$$

$$\hat{N}_k(\tilde{\Omega}) = \int F(k, E, \Theta) T(\Theta) \left[\int_{\tilde{\Theta}\in\tilde{\Omega}} P(k, E, \Theta, \tilde{\Theta})\, d\tilde{\Theta} \right] dE\, d\Theta$$

If it is believed that the error in measuring event's direction does not depend on particle energy, $P(k, E, \Theta, \tilde{\Theta})$ can be factored as:

$$P(k, E, \Theta, \tilde{\Theta}) = A_k(E, \Theta) R_k(\tilde{\Theta}|\Theta)$$

The function $A_k(E, \Theta)$ is known as the "effective area" introduced in section 3.3.1; $R_k(\tilde{\Theta}|\Theta)$ is known as the angular resolution (or point spread) function. Then, the number of events to be detected from the directions in the bin $\tilde{\Omega}$ is:

$$\hat{N}_k(\tilde{\Omega}) = \int F(k, E, \Theta) T(\Theta) A_k(E, \Theta) \left[\int_{\tilde{\Theta}\in\tilde{\Omega}} R_k(\tilde{\Theta}|\Theta)\, d\tilde{\Theta} \right] dE\, d\Theta \qquad (4.8)$$

The integration should be performed over the exposure time to the whole source and given $A_k(E,\Theta)R_k(\tilde{\Theta}|\Theta)$ can be done during data processing. Thus, by counting the number of events in an observation bin $N_k(\tilde{\Omega})$ and comparing it with $\hat{N}_k(\tilde{\Omega})$, it is possible to deduce some properties of the source function $F(k,E,\Theta)$. If the null hypothesis is rejected, the difference $N^s_{on}(\tilde{\Omega}) = (N_{on}(\tilde{\Omega}) - N^b_{on}(\tilde{\Omega}))$ should be interpreted as γ-ray count.

For instance, if a point source is considered with the source function $F(\gamma,E,\Theta) = F_0\delta(E-E_0)\delta(\Theta-\Theta_0(t))$ where $\Theta_0(t)$ is the source path in the local coordinates, the equation (4.8) gives:

$$\hat{N}^s_{on}(\tilde{\Omega}) = F_0 \int \delta(\Theta-\Theta_0(t))T(\Theta)A_\gamma(E_0,\Theta)\left[\int_{\tilde{\Theta}\in\tilde{\Omega}} R_\gamma(\tilde{\Theta}|\Theta)\,d\tilde{\Theta}\right]\,d\Theta =$$

$$= F_0 \int A_\gamma(E_0,\Theta_0(t))\left[\int_{\tilde{\Theta}\in\tilde{\Omega}} R_\gamma(\tilde{\Theta}|\Theta_0(t))\,d\tilde{\Theta}\right]\,dt$$

$$F_0 = \frac{\hat{N}^s_{on}(\tilde{\Omega})}{\int A_\gamma(E_0,\Theta_0(t))\left[\int_{\tilde{\Theta}\in\tilde{\Omega}} R_\gamma(\tilde{\Theta}|\Theta_0(t))\,d\tilde{\Theta}\right]\,dt}$$

If the null hypothesis is not rejected, an upper limit corresponding to the error ζ_u can be set as (see equation (4.7)):

$$N^s_{on}(\tilde{\Omega}) < u_1(\zeta_u)\sqrt{\sum_{\tilde{\Theta}} N^b_{on}(\tilde{\Theta}) + \sum_{\tilde{\Theta}} \frac{N^b_{on}(\tilde{\Theta})N_{on}(\tilde{\Theta})}{N^b_{out}(\tilde{\Theta})}} \qquad \tilde{\Theta}\in\tilde{\Omega}$$

leading to:

$$F_0 < \frac{u_1(\zeta_u)\sqrt{\sum_{\tilde{\Theta}} N^b_{on}(\tilde{\Theta}) + \sum_{\tilde{\Theta}} \frac{N^b_{on}(\tilde{\Theta})N_{on}(\tilde{\Theta})}{N^b_{out}(\tilde{\Theta})}}}{\int A_\gamma(E_0,\Theta_0(t))\left[\int_{\tilde{\Theta}\in\tilde{\Omega}} R_\gamma(\tilde{\Theta}|\Theta_0(t))\,d\tilde{\Theta}\right]\,dt}$$

4.7 Optimal bin.

If the Milagro detector had perfect angular resolution, then processing events from an infinitesimally small region of the sky around a point source would yield the maximum achievable sensitivity for source search as described in section 4.5. However, due to

detector's finite angular resolution, source events should be expected and accepted from some finite region around it. This, on the other hand, will increase the number of cosmic ray background events collected. Clearly, the optimal source acceptance region (called the "optimal bin") should have a configuration which provides the maximum power for the source search algorithm described in section 4.5. That is, for a given detector angular resolution function and given background event distribution on the sky, the optimal bin will provide the maximum value of the statistic U.

In fact, the procedure for optimal bin construction, like the procedure for the construction of the best critical region, should be a part of the statistical test formulation and can not be modified based on observed data. Since, in the case considered here, the critical region on the values of the statistic U has been defined, the optimal bin construction should be considered within the same framework. The optimal configuration $\tilde{\Omega}_{opt}$ should maximize the value of statistic $U(\tilde{\Omega})$, thus the equation on the optimal search region $\tilde{\Omega}_{opt}$ is:

$$\frac{\delta U(\tilde{\Omega})}{\delta \tilde{\Omega}} = 0$$

Using the definition of $U(\tilde{\Omega})$ from the equation (4.7):

$$U(\tilde{\Omega}) = \frac{\hat{N}^s_{on}(\tilde{\Omega})}{\sqrt{\hat{N}^b_{on}(\tilde{\Omega})[1 + (\sum_{x\in\tilde{\Omega}} \frac{\hat{N}^b_{on}(x)\hat{N}_{on}(x)}{\hat{N}^b_{out}(x)})/\hat{N}^b_{on}(\tilde{\Omega})]}}$$

and neglecting $\tilde{\Omega}$-dependence of the term in the square brackets one arrives at:

$$\frac{2}{\hat{N}^s_{on}(\tilde{\Omega})} \cdot \frac{\delta \hat{N}^s_{on}(\tilde{\Omega})}{\delta \tilde{\Omega}}\Big|_{\tilde{\Omega}_{opt}} = \frac{1}{\hat{N}^b_{on}(\tilde{\Omega})} \cdot \frac{\delta \hat{N}^b_{on}(\tilde{\Omega})}{\delta \tilde{\Omega}}\Big|_{\tilde{\Omega}_{opt}} \tag{4.9}$$

The solution of this equation will be performed under the assumptions that the shape of the observation bin is circular with opening angle $\tilde{\omega} << 1$; that the bin is centered on a source occupying not more than a solid angle with opening $\bar{\omega} << 1$ and that the number of background events in the bin is proportional to its area (this is reasonable in the small angle limit). Then:

$$\hat{N}^b_{on}(\tilde{\omega}) \sim \tilde{\omega}^2 \quad \text{and} \quad \frac{1}{\hat{N}^b_{on}(\tilde{\omega})} \cdot \frac{d\hat{N}^b_{on}(\tilde{\omega})}{d\tilde{\omega}}\Big|_{\tilde{\omega}_{opt}} = \frac{2}{\tilde{\omega}}$$

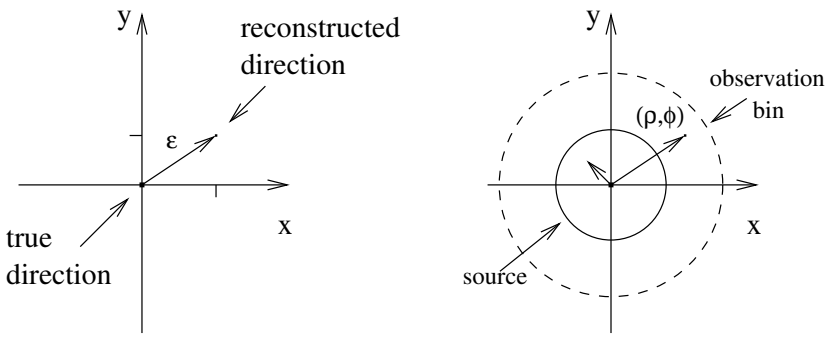

Figure 4.4: Conceptual diagram of a small angular reconstruction error parameterization.

Also, it will be assumed that the detector's angular resolution is described by a 2-D Gaussian with dispersion σ^2. This means that the error ϵ on the reconstructed angle can be parametrized by two variables x and y which form a Cartesian coordinate system (see figure 4.4) and $\epsilon = \sqrt{x^2 + y^2}$. The probability of observing event (x, y) away from the true direction is:

$$dR(x, y) = \frac{1}{2\pi\sigma^2} e^{-(x^2+y^2)/2\sigma^2} dxdy$$

This representation is valid for small errors since the sphere may be treated as a plane.

Under these assumptions, a point source with the source function $F_\gamma(E, \Theta) = F(E)\delta(\Theta - \Theta_0)$ will produce the signal (see equation (4.8)):

$$\hat{N}^s_{on} = \left(T(\Theta_0) \int_E F(E) A_\gamma(E, \Theta_0) dE\right) \times \int_{x^2+y^2 \le \tilde{\omega}^2} \frac{1}{2\pi\sigma^2} e^{-(x^2+y^2)/2\sigma^2} dxdy =$$

$$= \left(T(\Theta_0) \int_E F(E) A_\gamma(E, \Theta_0) dE\right) \times \int_0^{\tilde{\omega}} \frac{\epsilon}{\sigma^2} e^{-\epsilon^2/2\sigma^2} d\epsilon =$$

$$= \left(T(\Theta_0) \int_E F(E) A_\gamma(E, \Theta_0) dE\right) \times \left[1 - e^{-\tilde{\omega}^2/2\sigma^2}\right]$$

Then, the equation (4.9) becomes the equation on the optimal bin opening $\tilde{\omega}$:

$$\left(\frac{\tilde{\omega}_{opt}}{\sigma}\right)^2 = 2 \ln\left[1 + \left(\frac{\tilde{\omega}_{opt}}{\sigma}\right)^2\right] \quad \Rightarrow \quad \tilde{\omega}_{opt} \approx 1.585\sigma$$

For a source whose source function $F_\gamma(E, \Theta)$ is smooth within some opening angle

$\bar{\omega} << 1$ and zero outside and which is located in local direction Θ_0, the number of events detected from the source in the observation bin is (from equation (4.8)):

$$\hat{N}^s_{on}(\Theta_0, \tilde{\omega}, \bar{\omega}) = \frac{1}{2\pi\sigma^2} \int \int_{x^2+y^2 \leq \bar{\omega}^2} T(\Theta_0 + \vec{\epsilon}) F_\gamma(E, \Theta_0 + \vec{\epsilon}) A(E, \Theta_0 + \vec{\epsilon}) \times$$

$$\times \left[\int_{\tilde{x}^2+\tilde{y}^2 \leq \tilde{\omega}^2} e^{-((x-\tilde{x})^2+(y-\tilde{y})^2)/2\sigma^2} d\tilde{x} d\tilde{y} \right] dx dy dE$$

where $\vec{\epsilon} = (x, y)$ — describes coordinate of a point inside the source bin relative to its center Θ_0. Introducing the notations $\bar{\omega}^\sigma = \bar{\omega}/\sigma$ and $\tilde{\omega}^\sigma = \tilde{\omega}/\sigma$ and substituting the coordinate system parameterization from Cartesian to polar as $x = \rho\sigma\cos\phi,\ y = \rho\sigma\sin\phi$ the integration over $\tilde{\phi}$ can be performed and one arrives at:

$$\hat{N}^s_{on}(\Theta_0, \tilde{\omega}^\sigma, \bar{\omega}^\sigma) = \sigma^2 \int_0^{2\pi} \int_0^{\bar{\omega}^\sigma} \int T(\Theta_0 + \vec{\epsilon}) F_\gamma(E, \Theta_0 + \vec{\epsilon}) A(E, \Theta_0 + \vec{\epsilon}) dE \times$$

$$\times \left[\rho e^{-\rho^2/2} \int_0^{\tilde{\omega}^\sigma} e^{-\tilde{\rho}^2/2} I_0(\rho\tilde{\rho}) \tilde{\rho} d\tilde{\rho} \right] d\rho\, d\phi \tag{4.10}$$

where $I_0(\rho)$ is the zeroth order modified Bessel function of the first kind and $\vec{\epsilon} = (\rho\sigma\cos\phi, \rho\sigma\sin\phi)$.

In the expression (4.10) the integration over the angle ϕ can be performed by expanding the $T(\Theta_0 + \vec{\epsilon}) F_\gamma(E, \Theta_0 + \vec{\epsilon}) A(E, \Theta_0 + \vec{\epsilon})$ in to Taylor series:

$$T(\Theta_0 + \vec{\epsilon}) F_\gamma(E, \Theta_0 + \vec{\epsilon}) A(E, \Theta_0 + \vec{\epsilon}) = T(\Theta_0) F_\gamma(E, \Theta_0) A(E, \Theta_0) +$$

$$+ \vec{\epsilon} \cdot \nabla_\Theta \Big(T(\Theta_0) F_\gamma(E, \Theta_0) A(\Theta_0) \Big) + \mathcal{O}(\epsilon^2)$$

All even order corrections in $\vec{\epsilon}$ will give zero contribution to the integral (4.10) because the ϕ integration is performed over 2π range. Keeping only the first order correction in the source size $\bar{\omega}^\sigma$ the number of events in the observation bin factors as:

$$\hat{N}^s_{on}(\Theta_0, \tilde{\omega}^\sigma, \bar{\omega}^\sigma) = \left(\sigma^2 \int T(\Theta_0) F_\gamma(E, \Theta_0) A(E, \Theta_0) dE \right) \times$$

$$\times \int_0^{\bar{\omega}^\sigma} \rho e^{-\rho^2/2} \left(\int_0^{\tilde{\omega}^\sigma} e^{-\tilde{\rho}^2/2} I_0(\rho\tilde{\rho}) \rho d\tilde{\rho} \right) d\rho$$

Hence, in the equation (4.9) the Θ_0-dependent factor will cancel and the optimal bin

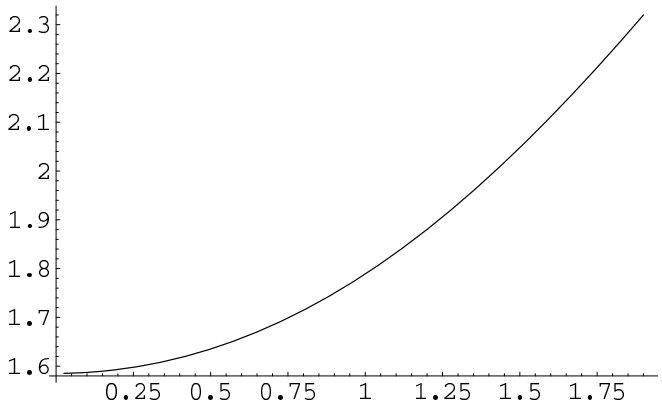

Figure 4.5: Optimal bin size $\tilde{\omega}^{\sigma}_{opt}$ as a function of the size source $\bar{\omega}^{\sigma}$.

$\bar{\omega}^{\sigma}$	0.00	0.35	0.40	0.50	0.60	0.70	0.80	0.90	1.05
$\tilde{\omega}^{\sigma}_{opt}$	1.585	1.610	1.617	1.635	1.657	1.684	1.715	1.750	1.810

Table 4.2: Source size $\bar{\omega}^{\sigma}$ and corresponding optimal bin size $\tilde{\omega}^{\sigma}_{opt}$.

size will loose its dependence of the source location. The figure 4.5 shows the solution $\tilde{\omega}^{\sigma}_{opt}$ of the optimal bin size problem (4.9) for the smooth source of size $\bar{\omega}^{\sigma}$. In the limiting case of the zero source size, the solution converges to the previously obtained $\tilde{\omega}^{\sigma}_{opt} = 1.585$. It is also interesting to note that the fraction $f^{opt}_{\gamma}(\bar{\omega}^{\sigma})$ of the signal events retained in the optimal bin is a very weak function of the source size:

$$f^{opt}_{\gamma}(0.0) = 0.715 \quad f^{opt}_{\gamma}(1.05) = 0.721 \quad f^{opt}_{\gamma}(1.9) = 0.751$$

The assumption that the number of background events in a bin is proportional to the bin's area is a good one for the Milagro data and the considered examples provide a good guideline for the choice of the observation bin size. Note that the constructed optimal bin is the optimal among the source centered circular bins and some other bin shape could be better. Nevertheless, the circular bin will be used in this analysis.

Chapter 5

Photon flux at the Earth due to near solar neutralino annihilations

'Yes,' I says to 'er, 'That's all very well,' I says. 'But if you'd been in my place you'd of done the same as what I done. It's easy to criticize,' I says, 'but you ain't got the same problems as what I got.'
'Ah,' said the other, 'that's jest it. That's jest where it is.'

George Orwell, "1984"

While some introduction to the main goal of the current work has been done, the proper formulation of the problem is long overdue.

There is overwhelming evidence that the Universe, and the galaxies in particular, are full of the "dark matter". There is no reason to assume that the Milky Way is any different. In this work, it is supposed that the weakly interacting particle (neutralino), predicted by super-symmetric theories, is the solution of the "dark matter" problem. If this is indeed the case, the neutralinos will form a halo around the Milky Way Galaxy and at the location of the Solar System the density of the halo neutralinos is often assumed to be $\rho_0 = 0.3\ (GeV/cm^3)$.

The neutralinos entering the Solar system may loose energy via elastic scattering with ordinary matter scatterers and become trapped in the Solar system. For simplicity, the Solar system is assumed to consist of the uniform density Sun only. This means that only the particles whose orbits cross the Sun can be captured on near-solar bound orbits

and their orbits will always cross the Sun. Due to the capture and repeated scatterings in the Sun, there will be a near-solar enhancement in the density of the neutralinos. This process is responsible for dark matter accretion in the Solar system. The dark matter diminution is due to neutralino-neutralino annihilations. The annihilation can not happen faster than accretion, otherwise, all dark matter would have annihilated by now. On the other hand, if accretion happens faster than annihilation, the Sun would constantly increase its mass. Thus, it is reasonable to assume that the Solar system has reached dynamic equilibrium and that the capture rate is equal to the annihilation one. Also, it is reasonable to assume that all possible elliptical orbits, not crossing the Sun have annihilated by now, as there is no mechanism to populate them by the incoming particles. Given that one of the annihilation channels is γ-ray production, one might expect an enhanced γ-ray signal from the neighborhood of the Sun due to neutralino annihilations. The purpose of this chapter is to estimate the γ-ray flux due to this process.

5.1 General formulation of the problem.

The problem of finding the density distribution of the particles in the Solar system can be addressed by kinetic theory.[1] If $g(p,x)$ is the density of particles in phase space, then it should satisfy the Boltzmann equation[2]:

$$\frac{d}{dt}g(p,x) = \frac{\partial g(p,x)}{\partial p^i}\dot{p_i} + \frac{\partial g(p,x)}{\partial x^i}\dot{x_i} = C[g(p,x)]$$

where $C[g(p,x)]$ is the collision integral and the explicit dependence of $g(p,x)$ on time has been dropped since in the considered model the process is assumed to be stationary: $\partial g(p,x)/\partial t = 0$. The spatial density of particles $n(x)$ is:

$$n(x) = \int g(p,x)dp$$

The collision integral consists of two terms: one is due to neutralino annihilations $C_a[g(p,x)]$ and the other is due to scattering in the Sun $C_s[g(p,x)]$.

[1] The hydro-dynamic approach is not justifiable since the neutralinos do not interact with each other.

[2] Summation over repeated indices is assumed.

$$C_a[g(p,x)] = -\int \sigma(p,p')g(p,x)g(p',x)dp' = -\langle\sigma v\rangle_a g(p,x)n(x)$$

$$C_s[g(p,x)] = \Theta(x,R_\odot)\int \{W(p+q,q)g(p+q,x) - W(p,q)g(p,x)\}\,dq$$

$$\Theta(x,R_\odot) = \begin{cases} 1, & |x| \le R_\odot \\ 0, & |x| > R_\odot \end{cases}$$

where q is the particle momentum change in a collision, $W(p,q)$ is the probability that a particle will change its momentum from p to $(p-q)$ in a collision.

A simplification can be made by noting that neutralino mass is much greater than that of any scatterer in the Sun and relative energy loss and momentum change of neutralino in a scattering are small. Thus, $W(p,q)$ is a quickly decreasing function of $|q|$ and diffusion approximation can be made:

$$W(p+q)g(p+q,x) \approx$$

$$\approx W(p,q)g(p,x) + q_i\frac{\partial}{\partial p^i}\Big(W(p,q)g(p,x)\Big) + \frac{1}{2}q_iq_j\frac{\partial^2}{\partial p^i\partial p^j}\Big(W(p,q)g(p,x)\Big) + \cdots$$

$$C_s[g(p,x)] \approx \frac{\partial}{\partial p^i}\Big\{\tilde{A}_i(p)g(p,x) + \frac{\partial}{\partial p^j}\Big(B_{ij}(p)g(p,x)\Big)\Big\}$$

where

$$\tilde{A}_i(p) = \int q_iW(p,q)dq \quad B_{ij}(p) = \frac{1}{2}\int q_iq_jW(p,q)dq$$

The function $W(p,q)$ can be constructed by considering a structure-less elastic scattering process where the angle of deflection of the incident particle in the center of mass reference frame is uniformly distributed between 0 and π.

The boundary condition for the problem can be formulated by assuming a Maxwellian distribution of velocities of galactic neutralinos. Then, in the Sun's reference frame the distribution will be shifted by the velocity of the Sun V_0 in the Galactic disk:

$$\lim_{x\to\infty} g(p,x) = g_\infty(p) = \rho_0\left(\frac{1}{2\pi v_0^2 m_\chi^2}\right)^{3/2} e^{-\frac{(p-m_\chi V_0)^2}{2v_0^2m_\chi^2}}d^3p$$

where m_χ is the neutralino mass. It will also be assumed that $\sqrt{2v_0^2} = \sqrt{V_0^2} = 220\ (km/s)$.

The sought for annihilation rate density at a point x is simply:

$$I_a(x) = -\int C_a[g(p,x)]dp = \langle \sigma v \rangle_a n^2(x)$$

Needless to say, the task of solving the stated problem analytically or numerically is daunting even when $W(p,q)$ has a simple structure. Direct computer simulations of the system will require enormous amounts of computer time. However, the distribution function $g(p,x)$ is not the immediate goal of the project and only the distribution of the annihilation points is of interest. Therefore, it is proposed to perform computer simulations of annihilating particles only. This poses two problems: how to know that the particle will annihilate and what the boundary condition on the annihilated particles is.

5.2 General idea of the solution.

The stated problem is solved with "backward in time" simulation. The particles generated at the annihilation points (so, it is known that the particles annihilated) are then propagated backward in time gaining energy in each scattering in the Sun until they exit the Solar system. If the distribution of the annihilation points is correct, the correct distribution of the annihilating particles at the boundary will be restored automatically. Thus, an algorithm should be devised to adjust an *a priori* distribution of the annihilation points in such a way as to reconstruct the correct distribution of annihilating particles at the Solar system boundary. This is possible if the particles carry information about their origin right until the annihilation point. The last assumption is reasonable since the neutralinos interact in the Sun only and their momentum does not change much in each scattering.

Since two particles are required in the act of annihilation, the particle pairs will be considered. Let X describe the state of a pair of particles, then X_0 will denote the pair state at the annihilation point and X_∞ — the state at the boundary. The trajectory pairs can be divided into two classes: the first class containing the trajectories with both particles trapped in the Solar system via scattering in the Sun and the second — the trajectories when at least one of the trajectories was not trapped and annihilated in its first flight through the Solar system. Supposing that the time of flight through the Solar

system is much smaller than the mean life time of the particle, the contribution from the second class can be neglected and only captured trajectory pairs can be considered. Let the joint probability that a pair of captured particles annihilated at X_0 and entered the Solar system at X_∞ be $P(X_\infty, cap, X_0)$. The task of the project is to find the distribution of the annihilation points or $P(X_0, cap)$ and according to Bayes' theorem, the joint probability $P(X_\infty, cap, X_0)$ is:

$$P(X_\infty, cap, X_0) = P(X_0|X_\infty, cap)P(X_\infty, cap) = P(X_\infty|cap, X_0)P(X_0, cap) \quad (5.1)$$

$$\int P(X_\infty, cap, X_0)\, dX_0 = P(X_\infty, cap) = \int P(X_\infty|cap, X_0)P(X_0, cap)\, dX_0 \quad (5.2)$$

and

$$P(X_\infty, cap) = P(cap|X_\infty)P(X_\infty)$$

where $P(X_\infty)$ is the known distribution of all trajectories entering the Solar system at infinity and $P(cap|X_\infty)$ is the conditional probability that the trajectories X_∞ will be captured.

The probabilities $P(X_\infty)$ and $P(cap|X_\infty)$ can be found analytically (see sections 5.2.3 and 5.2.4 correspondingly) and $P(X_\infty|cap, X_0)$ can be constructed using a backward in time computer simulation (see section 5.2.2). Also a method of solving the equation (5.2) for $P(X_0, cap)$ is described in section 5.2.1.

5.2.1 Solution of the Fredholm equation.

The equation (5.2) is the Fredholm equation of the first kind with respect to the sought for function $P(X_0, cap)$:

$$P(X_\infty, cap) = \int P(X_\infty|cap, X_0)P(X_0, cap)\, d(X_0, cap) \quad (5.3)$$

The kernel $P(X_\infty|cap, X_0)$ of this equation is not known analytically and is constructed in simulations (see section 5.2.2). It should be noted that due to the nature of the kernel construction method, the kernel $P(X_\infty|cap, X_0)$ represents a "list" of "(X_0, cap)"s and "(X_∞, cap)"s which are "connected" by the simulation process. Because the initial state (X_0, cap) is random and the propagation process is stochastic, it is statistically improbable to have repeated pairs in the list. This implies that all knowledge regarding the kernel can be expressed as:

$$P(X_\infty|cap, X_0) = \begin{cases} 1, & \{(X_\infty, cap), (X_0, cap)\} \in \text{list} \\ 0, & \{(X_\infty, cap), (X_0, cap)\} \notin \text{list} \end{cases}$$

Thus, the equation (5.3) becomes:

$$P(X_0, cap) = P(X_\infty, cap)$$

In other words, when annihilation state (X_0, cap) of a captured particle is associated with a state at the boundary (X_∞, cap) by the propagation process from section 5.2.2 the relative contribution $P(X_0, cap)$ from the state (X_0, cap) is $P(X_\infty, cap)$.

Thus, generating the initial states (X_0, cap) such that all final states (X_∞, cap) are sampled will lead to the solution of the equation (5.3).

To construct the histogram of the radial distribution of the annihilation points it should be noted that the state $X_0 = (\vec{r}_0, \vec{v}_1, \vec{v}_2)$ is the position and the velocities of the two particles at the annihilation point, thus:

$$P(\vec{r}_0, cap) = \int_{\omega(\vec{r}_0)} P(X_0, cap)\, d\vec{v}_1\, d\vec{v}_2 = \int_{\omega(\vec{r}_0)} P(\vec{r}_0, \vec{v}_1, \vec{v}_2)\, d\vec{v}_1\, d\vec{v}_2$$

where $\omega(\vec{r}_0)$ is the velocity volume over which the integration is being performed. This volume should include all particles which are captured and is finite. If the above integration is performed by the means of the Monte Carlo method with uniform sampling in the velocity volume $P(\vec{r}_0, cap)$ becomes:

$$P(\vec{r}_0, cap) = \frac{\omega^2(\vec{r}_0)}{N_v(\vec{r}_0)} \sum_{\vec{v}_1, \vec{v}_2} P(\vec{r}_0, \vec{v}_1, \vec{v}_2)$$

where $N_v(\vec{r}_0)$ is the number of sampled points.

Because the histogram of the annihilation points $H(\vec{r}_0)$ is defined is the average of $P(\vec{r}_0, cap)$ in the $\vec{r}_0$ bin, $H(\vec{r}_0)$ is:

$$H(\vec{r}_0) = \frac{1}{N_{r_0}} \sum_{\vec{r}_0} P(\vec{r}_0, cap) = \frac{1}{N_{r_0}} \sum_{\vec{r}_0} \frac{\omega^2(\vec{r}_0)}{N_v(\vec{r}_0)} \sum_{\vec{v}_1, \vec{v}_2} P(\vec{r}_0, \vec{v}_1, \vec{v}_2)$$

where N_{r_0} is the number of entries in the $\vec{r}_0$ bin.

The obtained expression for the histogram $H(\vec{r}_0)$ of the annihilation points may be

simplified by choosing a fixed large volume of the velocity space $\omega(\vec{r}_0) = \Omega$ and by noting that in any finite random sample the probability to observe two different pairs of orbits passing through the same point $\vec{r}_0$ is zero leading to $N_v(\vec{r}_0) = 1$.

$$H(\vec{r}_0) = \frac{\Omega^2}{N_{r_0}} \sum_{\vec{r}_0, \vec{v}_1, \vec{v}_2} P(\vec{r}_0, \vec{v}_1, \vec{v}_2)$$

5.2.2 Transition tables $\{(X_\infty, cap), (X_0, cap)\}$.

The transitions from X_∞ to X_0 for captured particles are found with backward in time simulations and was mentioned before. Because the particles evolve independently, each particle is propagated from its initial state (annihilation point) backward in time until it encounters an interaction in the Sun. At this point, momentum is changed according the rules of elastic scattering, the energy is gained, and the new angular momentum is computed. Afterwards, the particle is propagated until it encounters the next scattering. This process repeats until the accumulated energy is greater than zero, which means that the particle is no longer bound to the Solar system and its state at infinity is found and recorded.

Because the particle may spend long periods of time between interactions in the Sun, one must solve the equations of particle motion analytically and use the results. The motion in central potential fields is integrable and each trajectory is defined by integrals of motion: the total energy of neutralino E and its angular momentum $\vec{J}$. However, the kinematics depends only on mass densities of these quantities: $\mathcal{E} = E/m$ and $\vec{\mathcal{J}} = \vec{J}/m$ and mostly those will be used in the calculations.

The major simplification in the trajectory calculation comes from the fact that the energy and angular momentum are conserved between the scatterings. This means that between the scatterings the motion is executed in one plane and only rotation of the whole orbit is possible. The Runge-Lenz vector $\vec{\mathcal{K}}$, which fixes the orientation of the particle orbit and is conserved outside the Sun may change its direction only when particle passes through the Sun. Since between the scatterings the trajectory inside the Sun does not change its properties, the particle passage through the Sun can be tracked by rotation of the Runge-Lenz vector. Any point on the particle trajectory can be specified by its angle relative to the current direction of the Runge-Lenz vector.

The trajectory length inside the Sun plays the main role in the propagation process because it is the quantity which defines when the next scattering should occur. Given an initial point and the path-length inside the Sun until the next scattering, the point of

next scattering can be found by rotating the Runge-Lenz vector on the appropriate angle. Thus, the task is to convert the trajectory length inside the Sun into the angle of rotation. This problem can be solved analytically for the specified solar model.

The act of scattering can also be described as rescaling and the rotation of the velocity. Thus the whole process of particle propagation from its annihilation point back to infinity can be described as a sequence of rotations applied to the Runge-Lenz vector and the velocity rotation with rescaling.

The details of the simulation process are described in the appendix D.

5.2.3 Distribution of neutralinos at infinity $P(X_\infty)$.

Because the state X_∞ describes the state of two identical particles at the boundary, the $P(X_\infty)$ function is constructed as the product of two identical distributions describing a single particle:

$$P(X_\infty) = g_\infty(x_1) g_\infty(x_2)$$

The expression for $g_\infty(x)$ is a simple generalization of the results obtained earlier in [24] and [43]. However, a self-consistent derivation is provided here for completeness.

Let us choose a sphere of a large radius R around the Sun so that the effects of Sun's gravity are negligible and the velocity distribution of the particles is a known function $f(\vec{v})d^3\vec{v}$ and does not depend on the point on the sphere. Let n_χ be the concentration of particles at the sphere. The number of particles entering the Solar system per unit time with velocity $\vec{v}$ from the surface element $d\vec{A}$ is then:

$$dN = n_\chi f(\vec{v}) \left(\vec{v} \cdot d\vec{A}\right) d^3\vec{v}\, dt$$

where we are interested in the particles with $(\vec{v} \cdot d\vec{A}) < 0$ since the particles should enter the sphere.

Since we are considering the sphere $dA = R^2 \sin\theta\, d\theta\, d\phi_J$ and $d\vec{A} \uparrow\uparrow \vec{R}$ we can choose the coordinate system $(\theta,\, \phi_J)$ so that θ is counted from the direction of the velocity $\vec{v}$, then:

$$\left(\vec{v} \cdot d\vec{A}\right) = (\vec{v} \cdot \vec{R}) R \sin\theta d\theta d\phi_J = \frac{1}{2v} d\left(v^2 R^2 \sin^2\theta\right) d\phi_J = \frac{d\mathcal{J}^2 d\phi_J}{2v}$$

Then, the number of particles entering the Solar system is:

$$dN = n_\chi f(\vec{v}) \frac{dt\, d^3\vec{v}\, d\mathcal{J}^2 d\phi_J}{2v}, \quad (\vec{v} \cdot \vec{R}) < 0$$

If we are interested in the total distribution, we must note that since the velocity distribution does not depend on the spatial point, for every particle with $(\vec{v} \cdot \vec{R}) < 0$ there will be exactly one particle with $(\vec{v} \cdot \vec{R}) > 0$. Hence, the number of particles entering the Solar system with the velocity $\vec{v}$ and magnitude of angular momentum $\mathcal{J}$ per unit time is:

$$dN = n_\chi f(\vec{v}) \frac{dt\, d^3\vec{v}\, d\mathcal{J}^2 d\phi_J}{4v}, \quad P(X_\infty) = \frac{dN}{dt\, d^3\vec{v}\, d\mathcal{J}^2 d\phi_J} = \frac{n_\chi f(\vec{v})}{4v} \tag{5.4}$$

Consider the case when the velocity distribution at infinity is spherically symmetric as in [43],

$$f(v)v^2 dv = 4\pi(2\pi\sigma^2)^{-3/2} e^{-v^2/2\sigma^2} v^2 dv$$

then after integration over the spherical coordinates of the velocity and $d\phi_J$ one arrives at:

$$\frac{dN}{dt} = 2\pi^2 n_\chi f(\vec{v}) v\, dv\, d\mathcal{J}^2 = 2\pi^2 n_\chi f(\vec{v})\, d\mathcal{E}\, d\mathcal{J}^2$$

This is the formula (2.7) from [43].

If the motion of the Sun with speed V_0 in the locally isotropic Galactic halo is taken into account, then, as in [24]:

$$\tilde{f}(v)v^2 dv = \int_{\theta,\phi} f(\vec{v}) \frac{d^3\vec{v}}{v} = \frac{\sinh \frac{vV_0}{\sigma^2}}{\frac{vV_0}{\sigma^2}} e^{-V_0^2/2\sigma^2} \left[4\pi(2\pi\sigma^2)^{-3/2} e^{-v^2/2\sigma^2} v^2 dv\right]$$

and the rate at which the particles enter the Solar system per angular momentum per speed is:

$$dN = \pi n_\chi dt\, d\mathcal{J}^2 \int_{\theta,\phi} f(\vec{v}) \frac{d^3\vec{v}}{2v} = \frac{\pi}{2} n_\chi dt\, d\mathcal{J}^2 \tilde{f}(v) v^2 dv$$

This is the expression which will be used for calculation of the distribution of the particles at infinity.

5.2.4 Capture probability $P(cap|X_\infty)$.

Because the state X_∞ describes the state of two identical particles at the boundary and because each particle is captured independently, the $P(cap|X_\infty)$ function is constructed as the product of two identical capture functions describing a single particle:

$$P(cap|X_\infty) = g_{cap}(x_1)g_{cap}(x_2)$$

Also it will be assumed that the capture happens in one collision. In other words, after the first collision (forward time) the particle will have negative energy[3]. This will greatly simplify calculations, while higher order corrections can be considered. The argument for this is that the mean-free-path of neutralinos in the Sun $\lambda = 1/n_p\sigma_{p\chi}$ is of the order of $10^4 - 10^9$ $(R_\odot)$ for expected values of $\sigma_{p\chi}$. The energy loss in a collision is (see section D.9):

$$\Delta\mathcal{E} = \frac{2\eta(1-\cos\theta)}{(\eta+1)^2}\frac{v^2}{2} = \frac{2\eta(1-\cos\theta)}{(\eta+1)^2}\Big(\mathcal{E}-U(r)\Big) = \nu\Big(\mathcal{E}-U(r)\Big) \quad \eta = \frac{m_\chi}{m_p}$$

where $\mathcal{E}$ is the energy before the collision and $U(r)$ is the potential energy at the collision. Since θ is the scattering angle in the center-of-mass system and no cross-section structure is assumed, $\cos\theta$ is distributed uniformly between -1 and 1, this leads to the fact that ν is uniformly distributed between zero and $\frac{4\eta}{(\eta+1)^2}$.

$$\mathcal{E}_{after} = \mathcal{E}-\Delta\mathcal{E} < 0 \;\Rightarrow\; \mathcal{E}-\nu(\mathcal{E}-U(r)) < 0 \;\Rightarrow\; \begin{cases} \nu > \frac{\mathcal{E}}{\mathcal{E}-U(r)} & \text{need for capture} \\ 0 < \nu < \frac{4\eta}{(\eta+1)^2} & \text{allowed range} \end{cases}$$

Thus, the probability that a particle will be captured in one collision at the distance r from the center of the Sun is:

$$p_{cap}(\mathcal{E}, r) = \frac{(\eta+1)^2}{4\eta}\left[\frac{4\eta}{(\eta+1)^2} - \frac{\mathcal{E}}{\mathcal{E}-U(r)}\right]\Theta\left[\frac{4\eta}{(\eta+1)^2} - \frac{\mathcal{E}}{\mathcal{E}-U(r)}\right]$$

$$\Theta(z) = \begin{cases} 1, & z \geq 0 \\ 0, & z < 0 \end{cases}$$

The probability that a particle will travel distance y without scattering and scatter in

[3]The particle may scatter twice or more in the first pass through the Sun, but it is assumed to become trapped after the first collision.

$y, y + dy$ is:

$$dp = \frac{1}{\lambda} e^{-y/\lambda} dy \approx \frac{dy}{\lambda}$$

Again, this approximation is valid since the mean free path of neutralinos inside the Sun λ is much greater than the particle trajectory length inside the Sun.

The probability that the particle with energy $\mathcal{E}$ and angular momentum $\mathcal{J}$ will loose energy in one collision to become captured on the bound orbit is:

$$g_{cap}(x) = \int_0^{L(\mathcal{E},\mathcal{J})} \frac{1}{\lambda} p_{cap}(\mathcal{E}, r(y)) dy$$

where $L(\mathcal{E}, \mathcal{J})$ is the path-length inside the Sun.

From the energy conservation law:

$$\mathcal{E} = \frac{v^2}{2} + U(r) = \frac{\dot{r}^2}{2} + \frac{\mathcal{J}^2}{2r^2} + U(r)$$

$$\frac{dy}{dt} = \sqrt{2[\mathcal{E} - U(r)]}, \quad \frac{dr}{dt} = \sqrt{2[\mathcal{E} - U(r)] - \mathcal{J}^2/r^2}$$

$$g_{cap}(x) = \frac{2}{\lambda} \int_{r_{min}}^{r_{max}} \sqrt{\frac{2[\mathcal{E} - U(r)]}{2[\mathcal{E} - U(r)] - \mathcal{J}^2/r^2}} \left\{ \frac{(\eta+1)^2}{4\eta} \left[\frac{4\eta}{(\eta+1)^2} - \frac{\mathcal{E}}{\mathcal{E} - U(r)} \right] \right\} dr$$

The r_{min} is the minimal distance from the Sun's center to the orbit and can be found from the equation of motion:

$$\mathcal{E} = \mathcal{J}^2/2r_{min}^2 + U(r_{min}) = \mathcal{J}^2/2r_{min}^2 - \frac{\alpha}{2R_\odot} \left(3 - r_{min}^2/R_\odot^2\right) \Rightarrow$$

$$r_{min}^2 = R_\odot^2 \frac{(3\alpha R_\odot + 2\mathcal{E} R_\odot^2) - \sqrt{(3\alpha R_\odot + 2\mathcal{E} R_\odot^2)^2 - 4\alpha R_\odot \mathcal{J}^2}}{2\alpha R_\odot}$$

The r_{max} is computed from the restriction on maximum capturable energy and should not be greater than $R_\odot$ or less than r_{min}.

$$\frac{4\eta}{(\eta+1)^2} - \frac{\mathcal{E}}{\mathcal{E} - U(r)} > 0 \Rightarrow \mathcal{E} < -\frac{4\eta}{(\eta-1)^2} U(r)$$

$$r_{max}^2 = R_\odot^2 \left(3 - \frac{R_\odot}{\alpha}\frac{(\eta-1)^2}{2\eta}\mathcal{E}\right), \quad r_{min} \le r_{max} \le R_\odot, \quad \mathcal{E} < \frac{4\eta}{(\eta-1)^2}\cdot\frac{3\alpha}{2R_\odot}$$

The integrals which need to be executed to find $g_{cap}(x)$ are elliptical integrals. $g_{cap}(x)$ can be written in the form:

$$g_{cap}(x) = \frac{1}{\lambda}\int_{r_{min}^2}^{r_{max}^2}\sqrt{\frac{a-by}{ay-by^2-c}}dy -$$

$$-\frac{(\eta+1)^2}{2\eta}\cdot\frac{\mathcal{E}}{\lambda}\int_{r_{min}^2}^{r_{max}^2}\frac{dy}{\sqrt{(ay-by^2-c)(a-by)}}$$

where

$$a = 2\mathcal{E} + \frac{3\alpha}{R_\odot}, \quad b = \frac{\alpha}{R_\odot^3}, \quad c = \mathcal{J}^2$$

From Gradshtein and Rizhik(Russian 3.141-2 page 245):

$$\int_{r_{min}^2}^{r_{max}^2}\sqrt{\frac{a-by}{ay-by^2-c}}dy = \int_C^{r_{max}^2}\sqrt{\frac{y-A}{(y-B)(y-C)}}dy = 2\sqrt{(A-C)}\,EE(\gamma,q)$$

From Gradshtein and Rizhik(Russian 3.131-3 page 233):

$$\int_{r_{min}^2}^{r_{max}^2}\sqrt{\frac{1}{(ay-by^2-c)(a-by)}}dy = \frac{1}{b}\int_C^{r_{max}^2}\sqrt{\frac{1}{(y-A)(y-B)(y-C)}}dy =$$

$$= \frac{2}{b\sqrt{(A-C)}}EF(\gamma,q)$$

$$A > B \ge r_{max}^2 > C, \quad A = \frac{a}{b}, \quad B = \frac{a+\sqrt{a^2-4bc}}{2b}, \quad C = r_{min}^2 = \frac{a-\sqrt{a^2-4bc}}{2b}$$

$$\gamma = \arcsin\sqrt{\frac{r_{max}^2-C}{B-C}}, \quad q = \sqrt{\frac{B-C}{A-C}}$$

Further simplification comes from the fact that $A - C = B$

$m_\chi,\ (TeV)$	f_{out}	$I(m_\chi) \times \frac{\sigma_{p\chi}}{10^{-43}cm^2} \frac{\rho_0}{0.3GeV/cm^3},\ (s^{-1})$
0.1	0.195	$1.65\ 10^{18}$
0.2	0.195	$4.17\ 10^{17}$
0.5	0.196	$6.72\ 10^{16}$
1.0	0.199	$1.68\ 10^{16}$
2.0	0.201	$4.22\ 10^{15}$
5.0	0.2	$6.72\ 10^{14}$
10.0	0.2	$1.69\ 10^{14}$

Table 5.1: Summary of the simulation/computation results. Capture integral I and the fraction f_{out} of annihilations between 1 and 2 solar radii as a function of neutralino mass m_χ.

Where the elliptical integrals are:

$$EF(\phi,k) = \int_0^\phi 1/\sqrt{1-k^2\sin^2(t)}\,dt = \int_0^{\sin\phi} \frac{dt}{\sqrt{(1-t^2)(1-k^2t^2)}}, \quad |k|<1$$

$$EE(\phi,k) = \int_0^\phi \sqrt{1-k^2\sin^2(t)}\,dt = \int_0^{\sin\phi} \sqrt{\frac{1-k^2t^2}{1-t^2}}\,dt, \quad |k|<1$$

5.3 Predicted photon flux.

The results of the computer calculation are summarized in the table 5.1 for several selected neutralino masses. About $40-50\%$ of particles annihilate outside the Sun, but their distribution is a sharply falling function of distance from the Sun (see figures 5.1 and 5.2), so only the annihilations happening between one and two solar radii will be considered to produce detectable signal. The fraction of neutralinos annihilating between one and two radii of the Sun is denoted as f_{out} in the table.

Only a small fraction of the annihilated particles will produce photon signal. If photon yield for producing a photon with energy E_γ per neutralino in neutralino-neutralino annihilation is $b_\gamma(E_\gamma, m_\chi)$, the total number of photons produced per second is:

$$d\tilde{\Phi}_0 = I(m_\chi)\cdot f_{out}\cdot b_\gamma(E_\gamma, m_\chi)\,dE_\gamma$$

Some of the produced photons will be absorbed by the Sun. The fraction of the photons escaping the Sun is f_{escape} and is of the order of $1/2$. The distance between the Earth and the Sun is $L_\oplus$ which leads to the flux of number of photons per unit area per time at Earth from neutralino annihilations as:

$$dF_\chi(E_\gamma) = I(m_\chi) \cdot f_{out} \cdot b_\gamma(E_\gamma, m_\chi) \cdot f_{escape}/4\pi L_\oplus^2 \, dE_\gamma$$

$$dF_\chi(E_\gamma) =$$

$$= \frac{\rho_0}{0.3 \ (GeV/cm^3)} \cdot \frac{\sigma_{p\chi}}{10^{-43} \ cm^2} \cdot b_\gamma(E_\gamma, m_\chi) \cdot \frac{f_{out} \cdot f_{escape}}{0.2 \cdot 1/2} \cdot \frac{I(m_\chi)}{2.8 \cdot 10^{28}} \, dE_\gamma \quad (cm^{-2} s^{-1}) \tag{5.5}$$

The photon yield may have the following structure:

$$b_\gamma(E_\gamma, m_\chi) = b_\gamma^\delta(m_\chi)\delta\Big(E_\gamma - m_\chi\Big) + b_\gamma^c(m_\chi)P\Big(\frac{E_\gamma}{m_\chi}\Big)$$

where $P\Big(\frac{E_\gamma}{m_\chi}\Big)$ is the probability to produce photon with energy E_γ, $E_\gamma < m_\chi$ in the continuous spectrum neutralino to photon annihilation process.

There are indications (see [9]) that the continuum spectrum probability has the form:

$$P\Big(\frac{E_\gamma}{m_\chi}\Big) \sim \frac{1}{m_\chi} \cdot \Big(\frac{E_\gamma}{m_\chi}\Big)^{-1.5} e^{-7.8E_\gamma/m_\chi}$$

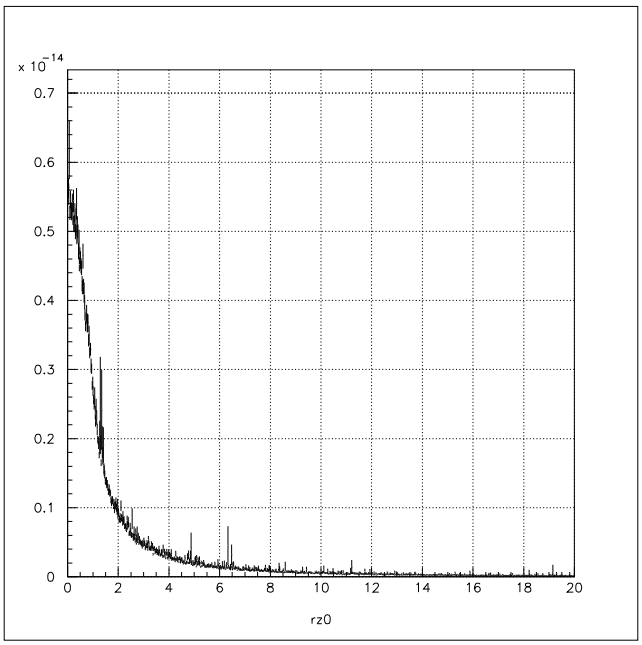

Figure 5.1: Radial distribution of the annihilation points for $m_\chi = 200\ (GeV)$ and $\sigma_{p\chi} = 10^{-43}\ (cm^2)$. Vertical scale is in arbitrary units, horizontal scale is in $R_\odot$. above $25 \cdot 10^6$ neutralino annihilations

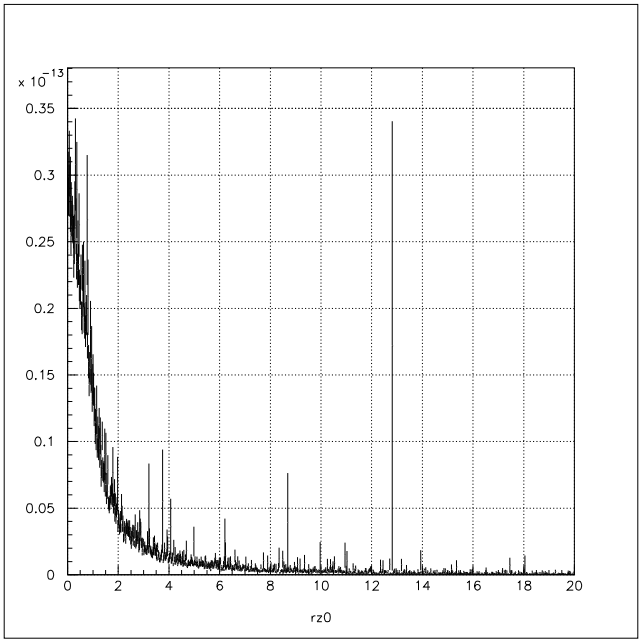

Figure 5.2: Radial distribution of the annihilation points for $m_\chi = 1000\ (GeV)$ and $\sigma_{p\chi} = 10^{-43}\ (cm^2)$. Vertical scale is in arbitrary units, horizontal scale is in $R_\odot$. above $22 \cdot 10^6$ neutralino annihilations

Chapter 6

Outcome of the test for presence of the photon flux from the Sun and its implications

His courage seemed suddenly to stiffen of its own accord.
George Orwell, "1984"

The gamma ray signal from neutralino annihilations near the Sun should appear as an excess number of events from the direction of geometrical center of the Sun over the expected background. Observation of the Solar region can be performed by tracking the Sun on the Celestial sphere using the one-arc-minute precision formulae for the Sun's Celestial coordinates from [12]. The interpretation of the observed signal, however, is not an easy problem. Largely, this is due to the fact that the cosmic ray background is not expected to be uniform; the Sun absorbs the cosmic rays impinging on it and forms a cosmic-ray shadow. The situation is complicated by the magnetic fields of the Earth and the Sun. Due to bending of charged particles trajectories in magnetic fields, the Sun's shadow will be smeared and shifted from the geometrical position of the Sun in the TeV range of particle energies. On the other hand, in the presence of strong Solar magnetic fields, lower energy particles can not reach the surface of the Sun and are reflected from it. Such particles are not being removed from the interplanetary medium and may not even form a cosmic-ray shadow of the Sun. Therefore, it is difficult to ascertain the exact shape of the cosmic-ray shadow at the Sun's position and deduce excess above it.

	N_{on}	N_{on}^{b}	U
Sun	137211	137728	-1.35
Moon	49762	50064	-1.31

Table 6.1: Number of events in the optimal bin centered on the Sun and the Moon (see section 4.5).

The effect of the Earth's magnetic field and the Solar wind can be studied by observing the shadow of the Moon during solar day. If the solar magnetic field is weak, the shadows of the Sun and the Moon should be very similar because of the geometry of the problem. The Sun and the Moon cover similar size regions on the celestial sphere and traverse similar paths on the local sky in one year of observation. In addition, the Moon is far enough from the Earth to be considered outside of the effect of the Earth's magnetic field, so is the Sun.

6.1 The data set.

The data to be used in this work was chosen to satisfy the following conditions: online reconstruction, the number of photo-tubes required to trigger the detector greater than 60, the number of photo-tubes used in the angular reconstruction (Nfit) greater than 20, zenith angles smaller than 45 degrees and all events should pass the gamma/hadron separation cut. The data used were collected between July 19 2000 and September 10 2001. The dates are motivated by introduction of the hadron separation parameter into the online reconstruction code on July 19, 2000 and detector turn-off for major repairs on the 11th of September 2001. Several data runs were disregarded from the dataset which included calibration runs and the data when the online DAQ was in an unstable regime.

For the Sun analysis a $\pm 5^{\circ}$ regions around the Moon and the Crab nebula were vetoed from the data set. For the Moon analysis, same size regions around the Sun and the Crab were vetoed. Overall, 1164.7 hours of exposure on the Sun and 423.5 hours of exposure on the Moon during the day time is obtained in this data set. The number of events in the optimal circular bin of 1.26° radius centered on the Moon and the Sun is given in table 6.1 and the sky maps with corresponding exposure graphs are presented in figure 6.1. The sky maps are generated according to the equation (4.1) with the vertical axis pointing to the Geocentric Geomagnetic North dipole pole.

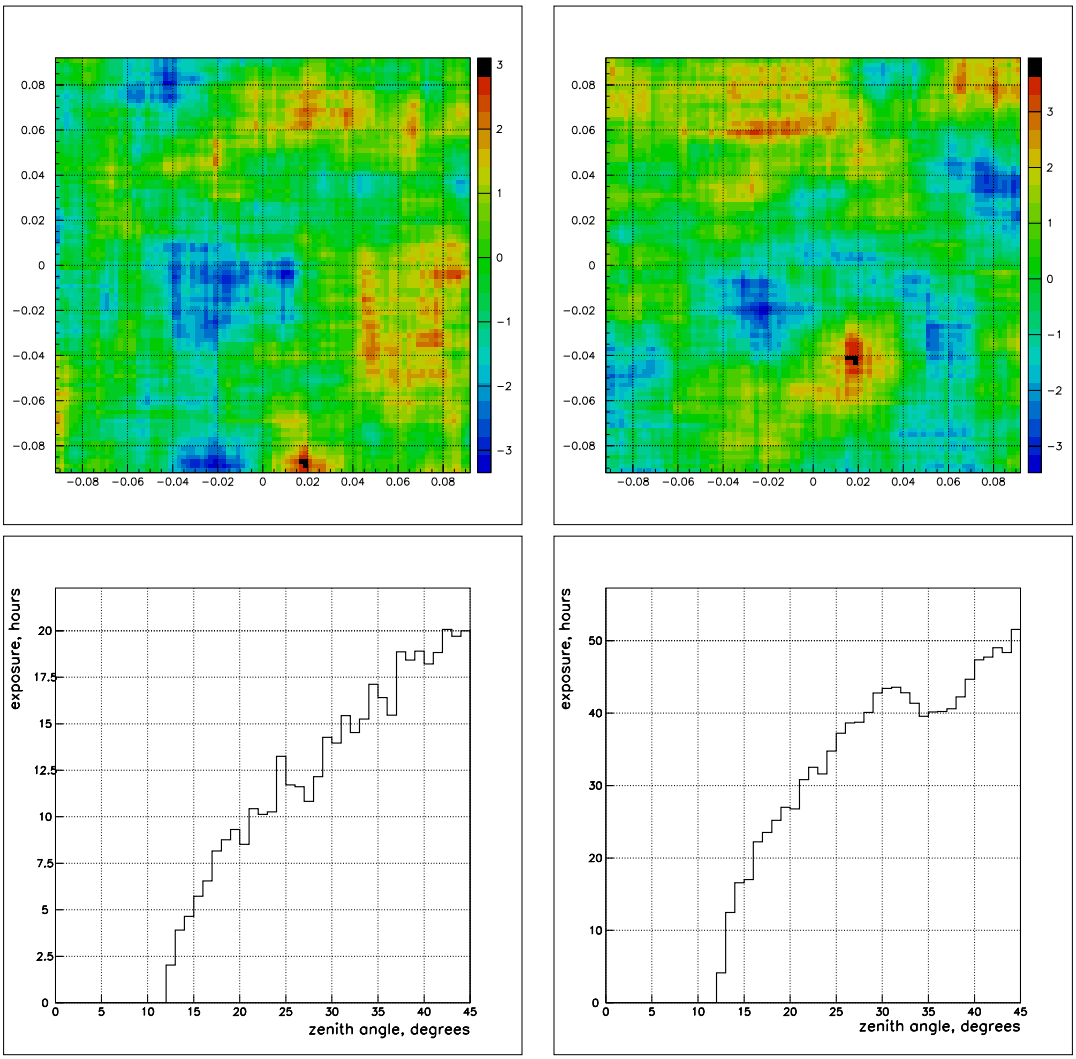

Figure 6.1: Significance maps of the regions of the sky around the daytime Moon(left) and the Sun(right) and the corresponding source exposure as function of zenith angle in hours per degree. The color code is the value of U (see equation (4.7)).

$m_\chi\ (TeV)$	$\Delta\ (cm^2 s)$	$\Sigma\ (cm^2 s)$
0.1	$1.055 \cdot 10^{11}$	0.000
0.2	$8.772 \cdot 10^{11}$	$4.969 \cdot 10^{7}$
0.5	$6.070 \cdot 10^{12}$	$2.634 \cdot 10^{9}$
1.0	$3.389 \cdot 10^{13}$	$2.127 \cdot 10^{10}$
2.0	$1.600 \cdot 10^{14}$	$1.280 \cdot 10^{11}$
5.0	$5.942 \cdot 10^{14}$	$1.208 \cdot 10^{12}$
10.0	$1.608 \cdot 10^{15}$	$5.575 \cdot 10^{12}$
20.0	$3.684 \cdot 10^{15}$	$2.136 \cdot 10^{13}$
50.0	$8.030 \cdot 10^{15}$	$1.035 \cdot 10^{14}$

Table 6.2: Coefficients of the flux limit calculation (see equation (6.1)).

$m_\chi\ (TeV)$	$F_\delta <\ (cm^{-2} s^{-1})$	$\frac{\sigma_{p\chi}}{10^{-43} cm^2} \frac{\rho_0}{0.3 GeV/cm^3} b_\gamma^\delta <$
0.1	$4.54 \cdot 10^{-8}$	770
0.2	$5.46 \cdot 10^{-9}$	351
0.5	$7.89 \cdot 10^{-10}$	328
1.0	$1.41 \cdot 10^{-10}$	234
2.0	$2.99 \cdot 10^{-11}$	204
5.0	$8.06 \cdot 10^{-12}$	339
10.0	$2.98 \cdot 10^{-12}$	512

Table 6.3: The upper limit on the monochromatic photon flux due to near-solar neutralino annihilations and corresponding upper limit on the $\sigma_{p\chi}\rho_0 b_\gamma^\delta$.

6.2 A limit on possible gamma-ray flux due to near-Solar neutralino annihilations.

Because the shape of the solar shadow is not known, not to claim a false signal the null hypothesis is formulated as cosmic-ray background is uniform and there is no γ-ray emission from the solar region. The mean value of the statistic U (see equation (4.5)) is equal to zero under this hypothesis. Based on the results of the measurement (see table 6.1) the formulated null hypothesis can not be rejected with significance $2.867 \cdot 10^{-7}$ (see table 4.1) and an upper limit on the possible γ-ray flux from the solar region should be obtained.

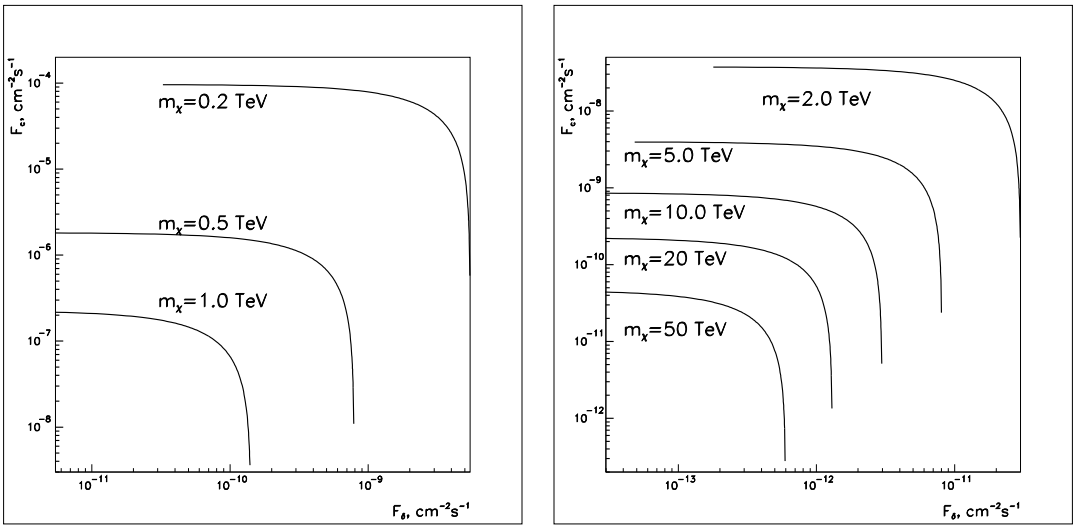

Figure 6.2: The values of (F_δ,F_c) below the lines are allowed based the constructed upper limit for corresponding neutralino masses.

$m_\chi\ (TeV)$	$F_c < \ (cm^{-2}s^{-1})$	$\frac{\sigma_{p\chi}}{10^{-43}cm^2}\frac{\rho_0}{0.3GeV/cm^3}b_\gamma^c <$
0.1	—	—
0.2	$9.64 \cdot 10^{-5}$	$6.47 \cdot 10^6$
0.5	$1.82 \cdot 10^{-6}$	$7.58 \cdot 10^5$
1.0	$2.25 \cdot 10^{-7}$	$3.75 \cdot 10^5$
2.0	$3.74 \cdot 10^{-8}$	$2.48 \cdot 10^5$
5.0	$3.97 \cdot 10^{-9}$	$1.65 \cdot 10^5$
10.0	$8.59 \cdot 10^{-10}$	$1.42 \cdot 10^5$

Table 6.4: The upper limit on the continuum photon flux due to near-solar neutralino annihilations and corresponding upper limit on the $\sigma_{p\chi}\rho_0 b_\gamma^c$.

The deficit of events from the direction of the Sun can not be greater than that produced by the Moon because of Sun/Moon similarities. To be conservative in setting the upper limit, the strongest event deficit produced by the Moon in 5° radius from its position should be used as a correction for possible presence of the shadow of the Sun. The smallest value of the statistic U observed in the sky map centered on the geometrical position of the Moon is -3.3 (see figure 6.1). The exposure on the Sun is about 2.75 greater than that on the Moon, leading to the estimated maximal deficit in the Sun's direction computed in terms of U as: $U_{sun}^{max} = -3.3\sqrt{2.75} = -5.5$.

Thus, the upper limit on the photon flux from the region of the Sun corresponding to the significance $2.867 \cdot 10^{-7}$ with error of the second kind $2.275 \cdot 10^{-2}$ (see table 4.1) is computed based on the value of the statistic U:

$$u_1 = 5.0 + 5.5 + 2.0 = 12.5$$

leading to the upper limit on the mean number of the gamma counts:

$$N < N_u = u_1\sqrt{N_b + \alpha N_s} = 4791$$

The differential photon flux due to neutralino annihilations taken from [9] has the form of:

$$\frac{dF(E)}{dE} = F_\delta \delta(E - m_\chi) + \frac{F_c(\frac{E}{m_\chi} > 0.01)}{m_\chi} \cdot \frac{\left(\frac{E}{m_\chi}\right)^{-3/2} e^{-7.8E/m_\chi}}{\int_{0.01}^{1} x^{-3/2} e^{-7.8x} dx}$$

where F_δ is the integral flux due to a δ-function-like photon annihilation channel and $F_c(\frac{E}{m_\chi} > 0.01)$ is the integral flux for $\frac{E}{m_\chi} > 0.01$ due to continuum photon spectrum annihilation channel of neutralinos with mass m_χ.[1]

Computing the number of events to be observed by the detector using the formula (4.8) for the given spectrum and following the procedure for setting an upper limit (from section 4.6), it is possible to set a constraint on the integral fluxes in the form:

$$F_\delta \cdot \Delta + F_c \cdot \Sigma < 4791 \tag{6.1}$$

F_δ and F_c are in the units of $cm^{-2}s^{-1}$ and the coefficients Δ and Σ are given in the table 6.2 for different neutralino masses. The figure 6.2 shows the region of parameter

[1] $\int x^{-3/2} e^{-ax} dx = -\frac{2e^{-ax}}{\sqrt{x}} - 2\sqrt{a\pi} Erf(\sqrt{ax})$

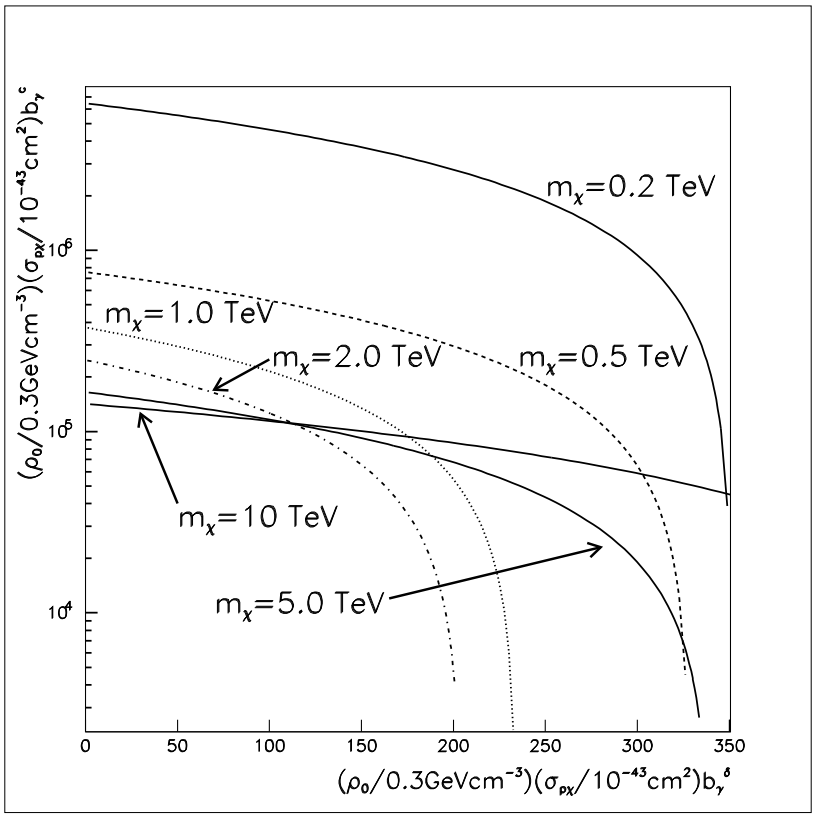

Figure 6.3: The values of $\left(\rho_0 \sigma_{p\chi} b_\gamma^\delta,\ \rho_0 \sigma_{p\chi} b_\gamma^c\right)$ below the lines are allowed based the constructed upper limit for corresponding neutralino masses.

space (F_c, F_δ) restricted by the upper limit.

The upper limit on the monochromatic photon flux due to neutralino annihilations and corresponding limit on $\sigma_{p\chi}\rho_0 b_\gamma^\delta$ (see equation (5.5)) are presented in table 6.3. The upper limit on the continuous photon flux with energies above $0.01 m_\chi$ due to neutralino annihilations and corresponding limit on $\sigma_{p\chi}\rho_0 b_\gamma^c$ (see equation (5.5)) are presented in table 6.4. The figure 6.3 depicts the combined limit on $\sigma_{p\chi}\rho_0 b_\gamma^c$ and $\sigma_{p\chi}\rho_0 b_\gamma^\delta$.

Chapter 7

Conclusion

The landscape that he was looking at recurred so often in his dreams that he was never fully certain whether or not he had seen it in the real world.

George Orwell "1984"

The Milagro data set collected during 2000-2001 has been analyzed and searched for the evidence of a steady near-1TeV γ-ray flux from near-solar neutralino annihilations. As a result of the analysis, it was argued that no evidence for the gamma-ray signal due to such a process has been found. The upper limit on the gamma-ray flux due to such a process with significance $2.867 \cdot 10^{-7}$ and the power $(1 - 2.275 \cdot 10^{-3})$ has been set. Even in the absence of a clear signal the constructed upper limit may constrain the values of free parameters of supersymmetric models.

The interpretation of the constructed limit on the gamma-ray flux is highly model dependent. It is based, for instance, on assumptions regarding the shape of the velocity distribution of the dark matter in the halo and the assumed structure of the Solar System. The current work presents a calculation of the neutralino annihilation rate density as a function of distance from the Sun and the neutralino capture rate onto near-solar bound orbits. It is shown that in the considered model only about 50% to 60% of annihilations happen inside the Sun. The calculation allowed translating the established limit on the gamma-ray flux from neutralino annihilations to the limit on the product of the neutralino-proton scattering crossection $\sigma_{p\chi}$, the integrated photon yield per neutralino in neutralino-neutralino annihilation b_γ and the local galactic halo dark matter density ρ_0.

To the knowledge of the author the current work presents a first attempt to set a constraint on the parameters of supersymmetric models by observing high energy gamma rays from the region of the Sun. Continuous improvements in reconstruction algorithms, detector modifications and longer observation times will led to a better upper limit. One of the factors which lead to a deterioration of the constructed upper limit is the inability to compensate for presence of the Solar cosmic-ray shadow due to the intricate structure of the Solar magnetic fields. Once the cosmic-ray shadow of the Sun is understood quantitatively, it may be possible to improve upon the limit.

Appendix A

Poisson distribution

A.1 Definition

The Poisson distribution arises in many problems as the distribution of the number of occurrences of some event over an interval of time or region of space. The distribution assumes that an event can occur at random at any time or point in space and that the probability of event occurrence does not depend on any other event. The Poisson distribution is defined as:

$$p(k;\lambda) = \frac{\lambda^k}{k!}e^{-\lambda} \tag{A.1}$$

$$\sum_{k=0}^{\infty} p(k;\lambda) = e^{-\lambda}\sum_{k=0}^{\infty}\frac{\lambda^k}{k!} = e^{-\lambda}e^{\lambda} = 1$$

$$< k >= \sum_{k=0}^{\infty} kp(k;\lambda) = e^{-\lambda}\sum_{k=0}^{\infty}\frac{k\lambda^k}{k!} = e^{-\lambda}\lambda\sum_{k=1}^{\infty}\frac{\lambda^{k-1}}{(k-1)!} = \lambda$$

$$D(k) =< k^2 > - < k >^2 = e^{-\lambda}\sum_{k=0}^{\infty}\frac{k^2\lambda^k}{k!} - \lambda^2 =$$

$$= e^{-\lambda}\sum_{k=1}^{\infty}\left[\frac{(k-1)\lambda^k}{(k-1)!} + \frac{\lambda^k}{(k-1)!}\right] - \lambda^2 = e^{-\lambda}\left[\lambda^2 e^{\lambda} + \lambda e^{\lambda}\right] - \lambda^2 = \lambda$$

A.2 Gaussian Limit of Poisson Distribution

Substituting the $k!$ in the Poisson distribution (A.1) by the approximate expression using the Stirling formula:

$$n! = \sqrt{2\pi n}\left(\frac{n}{e}\right)^n e^{\theta(n)}$$

the Poisson distribution becomes:

$$p(k;\lambda) \approx \sqrt{\frac{1}{2\pi\, k}}\left(\frac{e\lambda}{k}\right)^k e^{-\lambda}$$

or

$$\ln\left[p(k;\lambda)\sqrt{2\pi\, k}\right] \approx k\ln\left[\frac{e\lambda}{k}\right] - \lambda = k\left[1 - \ln\frac{k}{\lambda}\right] - \lambda$$

Let $k = \lambda + \delta$ than

$$\ln\left[p(k;\lambda)\sqrt{2\pi\, k}\right] \approx (\lambda+\delta)\left[1 - \ln\frac{\lambda+\delta}{\lambda}\right] - \lambda =$$

$$= (\lambda+\delta)\left[1 - \sum_{n=1}^{\infty}(-1)^{n+1}\frac{1}{n}\left(\frac{\delta}{\lambda}\right)^n\right] - \lambda = -\frac{1}{2}\frac{\delta^2}{\lambda} + \frac{1}{6}\frac{\delta^3}{\lambda^2} + \mathcal{O}(\frac{\delta^3}{\lambda^2})$$

Thus:

$$p(k;\lambda) \approx \sqrt{\frac{1}{2\pi\,(\lambda+\delta)}}\, e^{-\frac{\delta^2}{2\lambda}} \cdot e^{\frac{\delta^3}{6\lambda^2} + \mathcal{O}(\frac{\delta^3}{\lambda^2})}$$

For sufficiently small δ such that $\frac{\delta}{\lambda} << 1$ and $\left|e^{\frac{\delta^3}{6\lambda^2}} - 1\right| << 1$ the Poisson distribution approaches the Gaussian distribution with mean and dispersion equal to λ:

$$\left|e^{\frac{\delta^3}{6\lambda^2}} - 1\right| << 1 \quad \Rightarrow \quad \left|\frac{\delta^3}{6\lambda^2}\right| << 1 \quad \Rightarrow \quad \frac{\delta}{\lambda} << \sqrt[3]{\frac{6}{\lambda}} \leq 1,\ \forall\ \lambda \geq 6$$

$$p(k;\lambda) = \frac{\lambda^k}{k!}e^{-\lambda} \rightarrow \sqrt{\frac{1}{2\pi\lambda}}\, e^{-\frac{(k-\lambda)^2}{2\lambda}} \quad : \quad \left|\frac{(k-\lambda)^3}{6\lambda^2}\right| << 1,\ \forall\ \lambda \geq 6 \tag{A.2}$$

Appendix B

Calibration

For, after all, how do we know that two and two make four?
George Orwell, "1984"

The desire to reconstruct the position of events on the Celestial Sphere with systematic errors much less than 1° dictates that the times registered by PMTs have to have resolution about $1\ (ns)$ and the locations of the photo-tubes be known to about $10\ (cm)$ accuracy in horizontal and about $3\ (cm)$ in vertical directions. To meet the latter requirement photographic and theodolite surveys of the pond were performed. At the end of the construction period, when the pond was filled with water, an "as-built" measurement of the PMT elevation was done.

Even though great care has taken to construct all PMT channels as uniformly as possible, remaining systematic differences in PMT channels should be studied and removed. This includes synchronization of all TDC modules (find TDC time offsets and conversion factors) and compensation for the PMT-pulse amplitude dependence of TDC measurements (known as the slewing correction).

To correctly reconstruct the shower front, shower size and, ultimately, to estimate the energy of the primary particle, the relative "pulse-height" to photo-electron (PE) conversion must be determined to interpret all PMT amplitude measurements in a common unit for each event. This is then translated to an absolute scale of the energy deposited in the water.

Full description of the calibration system with its components, operation, data analysis and other comments is available in [13] and references cited therein.

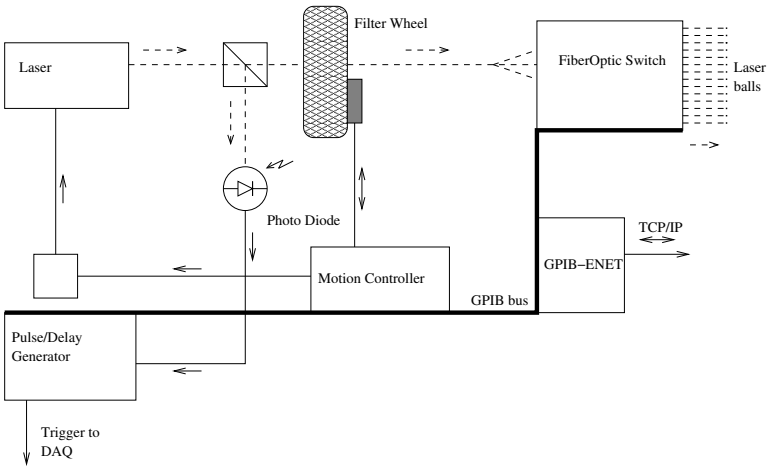

Figure B.1: Calibration system setup

B.1 Calibration system setup.

The Milagro calibration system has been designed to reflect all the above goals and is based on the laser – fiber-optic – diffusing ball concept used in other water-Cherenkov detectors (See, for instance, [6]). A computer operated motion controller (Newport MM3000) drives a neutral density filter wheel to attenuate a pulsed nitrogen dye laser (Laser Photonics LN120C) beam. The beam is directed to one of the thirty diffusing laser balls through the fiber-optic switch (DiCon MC606) as shown on Fig B.1. Part of the laser beam is sent to a photo-diode. When triggered by the photo-diode, the pulse-delay generator (Stanford Research DG535) sends a trigger pulse to the data acquisition system. A laser fire command is issued by the motion controller, providing full automation of the calibration process. The balls are floating in the pond so that each PMT can register signals from more than one light source. Such a redundant setup allows calibration of the PMTs and the electronics.

Calibration data was collected by stepping the filter wheel through a full circle in 10 degrees increments for each laser ball. On each laser ball - filter wheel setting about 2000 laser triggers at $20\ (Hz)$ and about 1600 "random" triggers (with no light input) at the rate of $400\ (Hz)$ were sent to the data acquisition system. Raw data from all PMT channels was recored and analyzed. Only 2- and 4-edge events with correct polarity were selected to ensure proper ToT determination. For purposes of occupancy measurements all data was used without any edge selection.

B.2 Timing calibration.

The importance of accurate time readings from the PMT channels can not be over stressed as the quality of event reconstruction depends on it. The issues which need to be addressed are described in this section.

B.2.1 TDC Conversion Factor.

The time of PMT pulse threshold crossings is read by LeCroy 1887 FASTBUS TDC modules. These digital devices measure time in the units of "counts" and, according to specifications, each count corresponds to 0.5 nanoseconds. Introduction of known variable delays in the calibration-DAQ trigger logic[1] allowed observation of common time shifts in all PMT channels to verify the TDC conversion factors at 2.0000 ± 0.0003 counts per nanosecond. This assured that all TDC modules operate on a common scale and allowed for a simple interpretation of TDC measurements.

B.2.2 Electronic slewing correction.

Time response of a PMT channel depends on the input light intensity and is called electronic slewing. Indeed, a weaker pulse will cross the discriminator threshold later than a strong one arriving at the same time (see figure B.2). Based on the ToT PMT pulse model described in 3.1.2, when the size of the pulse is described by the time over threshold, a slewing correction can be devised by studying the PMT pulse arrival time (T_{start}) as a function of ToT for different filter wheel transparency settings. The time of light pulse emission is supplied by the photo-diode and is believed to be free of slewing effects since the light level incident on the diode is constant. The slewing correcting curve is found by fitting the obtained calibration data with a polynomial (see figure B.3).

Note, however, that obtained T_{start} includes time propagation of the laser pulse in the detector medium and optical fibers. These may vary from PMT to PMT and should be taken into account to produce true T_{start} versus ToT dependence.

The procedure described above should be performed independently for both threshold levels HiToT and LoToT .

[1] Special TDC calibration data should be taken for this procedure.

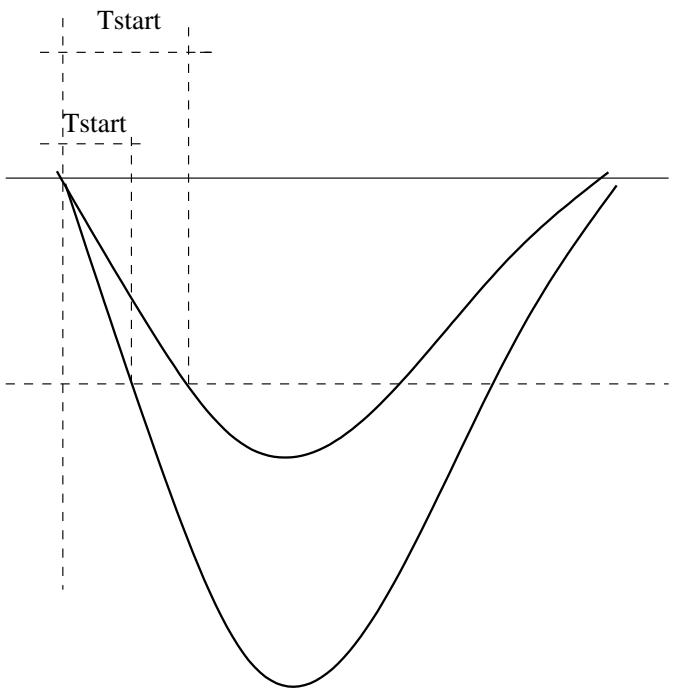

Figure B.2: Illustration of the electronic slewing. Stronger pulses cross the discriminator threshold earlier than the weaker ones.

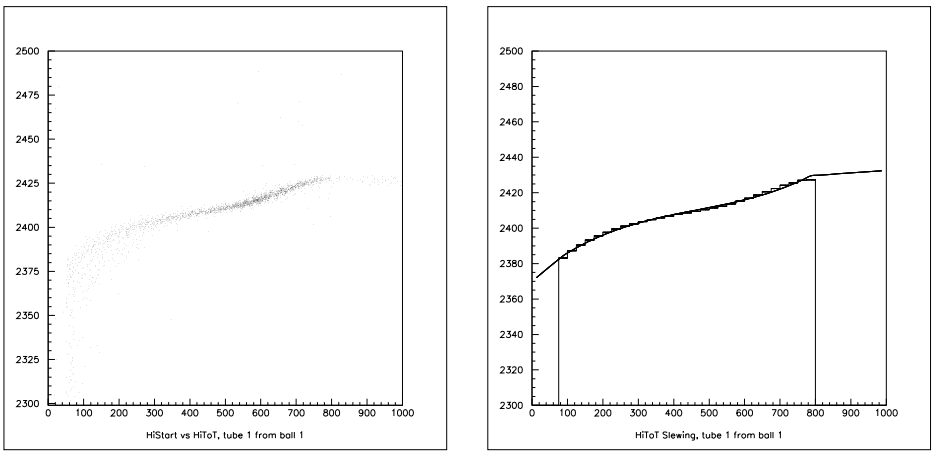

Figure B.3: Plots show T_{start} vs ToT data obtained for calibration (left) and the polynomial fit to the data (right). The units of both axes are TDC counts.

B.2.3 Speed of light in water, fiber delay.

In order to correct for propagation time of light in the detector, coordinates of PMTs and laser balls as well as the speed of light in water must be known. PMT and laser ball coordinates are known from the survey. Only a typical index of refraction of water is found in reference tables and fiber optic delays may vary from laser ball to laser ball, thus, all these parameters need to be measured with the calibration system.

Interestingly enough, this problem can be easily solved [17] if several PMTs can register light from two laser balls (cross-calibration). The times measured from two different laser balls T^1_{start} and T^2_{start} on the same PMT after slewing correction should be identical. The non-zero difference between the times T^1_{start} and T^2_{start} can be attributed to an error in the water propagation time $\Delta_{propagation}$ and/or difference in the laser balls' fiber optic delay Δ_{fiber}. If τ is defined as:

$$\tau = T^1_{start} - T^2_{start} - \Delta_{fiber} - \Delta_{propagation}$$

it will be zero in absence of errors in water propagation time and fiber delays.

The distribution over all PMTS of observed τ from a given laser ball pair can be constructed and studied. Since the Δ_{fiber} is constant for the given laser ball pair and $\Delta_{propagation}$ depends on the relative PMT ball positions, the use of correct speed of light will yield the minimal width of the τ distribution. After that, the mean of the distribution can be interpreted as the fiber optic difference Δ_{fiber}. Note that a PMT in close proximity to any one of the laser balls will have enhanced sensitivity to speed of light variation, while PMTs located half way between the laser balls will have enhanced sensitivity to the fiber optic difference.

Needless to say that the procedure described in this subsection can be used to test the self consistency of the timing calibration. The use of wrong coordinates of laser balls or PMTs will reveal itself as mismatch in the slewing curves (τ). In fact, using this procedure, it was discovered that coordinates of several PMTs were interchanged. An extension of the procedure described here is discussed in [18] where coordinates of the laser balls themselves are allowed to vary and can be restored.

Correcting the slewing curves by corresponding fiber optic delays and water propagation times yields the final calibration curves of T_{start} as a function of ToT.

B.3 Photo-Electron calibration.

The main purpose of the photo-electron calibration is to find a relationship between the observed ToT and the number of photo-electrons emitted inside the photo-tube. The calibration procedure is based on a well known occupancy method described in the literature (see for instance [6] or [32]) and proceeds in two general steps. First, the ToT-PE conversion is established for low input light levels using the occupancy method and then a different procedure is applied to calibrate PMTs at high light levels given the characteristics of the calibration filter wheel. The whole procedure relies on the assumptions that the number of photo-electrons produced in a PMT is proportional to the light intensity at the PMT's photocathode, that the input light level into the calibration system is constant, and that all light level modulation is due to a controlled change in the transmittance of the filter wheel only.

The calibration data required for photo-electron calibration is the same as for the timing calibration which is obtained with laser light passing through a filter at different transparency settings. While it is difficult to establish the light level stability of the laser output, it was found that if probability of the laser to produce no light when it is triggered is less than 2.5%, the PE calibration results are self consistent.

This section presents the main ideas of the PE calibration followed by a description of innovations in the method implementation. Full description of the occupancy method applied for Milagro calibration is presented in [14], [32] and [13].

B.3.1 Low light level calibration and the Occupancy method.

The occupancy method is based on the assumption that the number of photo-electrons produced at a PMT's photocathode obeys a Poisson distribution: $P(n;\lambda) = \frac{\lambda^n}{n!}e^{-\lambda}$. Here λ is the mean number of PEs produced at the photocathode. This is justified by the assumption that the emission of a photo-electron is not related to emission of a different one which is true if the photo-tube did not reach its saturation.

The probability η that a photo-tube registered the light pulse (which means at least one photo-electron was emitted from the photo-cathode) is called the occupancy and is given by:

$$\eta = P(n>0;\lambda) = 1 - P(n=0;\lambda) = 1 - e^{-\lambda} \quad \Rightarrow \quad \lambda = -\ln(1-\eta)$$

Based on its definition, occupancy η can be easily measured if a PMT is illuminated

many times by the light pulses of identical intensity:

$$\eta = \frac{\text{number of observed pulses}}{\text{number of sent pulses}}$$

As the intensity of input light is varied, it is possible to find a relationship between the number of PEs and the observed ToT directly. However, for high light levels when $\lambda > 2$, it is not possible to measure λ reliably based on η, since the error of the measurement on λ increases exponentially with error on η:

$$\Delta\lambda = \frac{1}{1-\eta}\Delta\eta = e^{\lambda}\Delta\eta$$

B.3.2 High light level calibration.

The high light level calibration is based on the assumption that there is no saturation of the PMT channel and the mean number of photo-electrons produced is proportional to the input light level intensity. If the transmittance of the filter wheel T is known, then:

$$\lambda = a \cdot T$$

where a is some parameter which is constant, but different for different laser ball-PMT pairs. It can be found from this equation at low light levels because T is known and λ can be measured with the occupancy method. Thus, given the transmittance properties of the filter wheel, the ToT to PE conversion can be found at high light levels with a linear error on λ.

For some PMT laser ball pairs, even the lowest light level possible was relatively high for the occupancy method to be used. For these PMTs, a farther away laser ball was used to establish the ToT-to-PE conversion for lower light levels. The obtained conversion curve was then extended by the data from the nearest laser ball to the highest possible light level.

If, contrary to the assumption, saturation of the PMT channel is present, the number of PEs can not be established using this method. However, since the goal of calibration is to study the PMT response to different light levels, this is not a problem and the method described here allows one to infer the light intensity at the PMT cathode from the observed ToT as the effective number of PEs which should have been emitted from the photocathode provided the PMT response were linear.

B.3.3 Filter calibration.

As was mentioned earlier, transmittance properties of the filter wheel are important for high light level PE calibration. The transmittance properties can be obtained from the manufacturer of the filter or can be measured in laboratory. A method to calibrate the filter wheel using the same calibration data as for slewing and PE calibration was proposed and used. This method has the advantage that the filter is calibrated as it is being used in detector calibration. The method employs the occupancy method with additional supposition that for any two sufficiently close transmittances of the filter T_1 and T_2 there exist a PMT for which the occupancy method can be used at both light intensities. Then, given two corresponding measurements of mean number of photo-electrons:

$$\frac{T_2}{T_1} = \frac{\lambda_2}{\lambda_1}$$

The transmittance T_3 can be related to T_2 in the analogues manner and so forth, leading to the restoration of the levels of transmittance for all filter settings. Because the absolute calibration of the filter is not required, it is always possible to set $T_0 = 1$.

B.3.4 Dynamic Noise Suppression.

The PE and filter calibration procedures rely on correct knowledge of PMT occupancy. PMT thermo-electron emission, Cherenkov light from the shower particles and other sources can cause a signal on the PMT output not related to the input calibration light. This noise will increase the measured PMT occupancy and damage the calibration accuracy.

Dynamic noise suppression is a technique which allows correction of the apparent occupancy on a tube by tube basis and is based on the assumption that the arrival of the laser light is not correlated with the noise pulses. Then, the probability to observe anything (apparent occupancy $P(any)$) is:

$$P(any) = P(laser) + P(noise) - P(laser) \cdot P(noise)$$

$$\eta = P(laser) = \frac{P(any) - P(noise)}{1 - P(noise)}$$

where $P(laser)$ is the probability to observe laser light (true occupancy η) and $P(noise)$

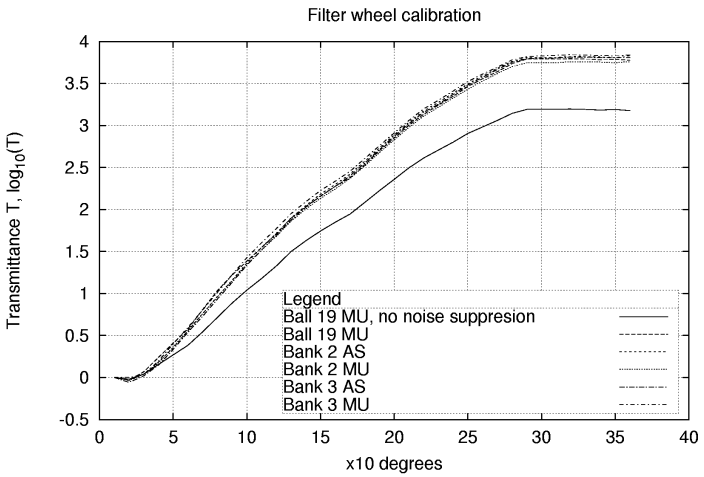

Figure B.4: Filter wheel calibration with and without noise suppression. (Bank 2,3 represent laser balls 11-20 and 21-30 respectively, while AS and MU represent PMTs from "top" and "bottom" layers used for filter calibration.)

is probability to observe noise pulse.

$P(any)$ can be measured by sending laser pulses to a PMT, as before, while $P(noise)$ can be estimated by sending uncorrelated triggers to data acquisition system without any light input which can be interlaced with the laser data taking.

The dynamic noise suppression is an important step in calibration process and was used for the ToT-to-PE and filter calibrations. The effect of the noise suppression is shown on figure B.4 where the filter wheel calibration curves are presented with and without the noise suppression.

B.3.5 Statistical error of the occupancy method.

In order to address the question of the accuracy of the occupancy method, suppose that n shots of the laser beam were sent, out of which m were detected by the PMT. Occupancy η is estimated as:

$$\eta = \frac{m}{n}$$

η	$\delta(\eta)$	pass/fail
0.1	0.009	fail
0.2	0.009	pass
0.3	0.008	pass
...	...	...
0.8	0.004	pass
0.9	0.002	fail

Table B.1: Occupancy accuracy test results to satisfy the error $q = \frac{\Delta\lambda}{\lambda} = 0.01$ on measured λ with $n = 2000$ laser shots.

The question of the accuracy of this estimation is that of the confidence interval. Since the probability of a PMT registering a signal in a shot is equal to η, then the number of detected pulses m is distributed according to binomial distribution:

$$P_\eta(m,n) = C_n^m \eta^m (1-\eta)^{n-m}, \quad C_n^m = \frac{n!}{m!(n-m)!}$$

The upper bound of the confidence interval η_{upper} corresponding to the significance α is defined so that probability of detecting $k \leq m$ pulses is less than $(1-\alpha)$:

$$P_{\eta_{upper}}(k \leq m, n) = \sum_{k=0}^{m} C_n^k \eta_{upper}^k (1-\eta_{upper})^{n-k} \leq 1-\alpha \tag{B.1}$$

Correspondingly, lower bound η_{lower} is such that

$$P_{\eta_{lower}}(k \geq m, n) = \sum_{k=m}^{n} C_n^k \eta_{lower}^k (1-\eta_{lower})^{n-k} \leq 1-\alpha$$

or

$$\sum_{k=0}^{m-1} C_n^k \eta_{lower}^k (1-\eta_{lower})^{n-k} \geq \alpha \tag{B.2}$$

If the required relative error on the value of occupancy is $\delta(\eta) = \frac{\Delta\eta}{\eta}$ then η_{upper} should be no greater than $(1+\delta(\eta))\eta$ and η_{lower} should be no less than $(1-\delta(\eta))\eta$. Thus, for given number of laser shots and number of registered pulses it is possible to check if the required accuracy is met. The requirements on the accuracy $\delta(\eta)$ are governed by the requirement on the relative error $q = \frac{\Delta\lambda}{\lambda}$ on PE (λ) determination:

$$\lambda = -\ln(1-\eta) \quad \Rightarrow \quad \Delta\lambda = \frac{1}{1-\eta}\Delta\eta$$

$$q = \frac{\Delta\lambda}{\lambda} = -\frac{\Delta\eta}{(1-\eta)\ln(1-\eta)} \quad \Rightarrow \quad \delta(\eta) = -q\frac{1-\eta}{\eta}\ln(1-\eta)$$

Now, the task is to estimate the allowed range of occupancies η with error not exceeding the specified value q provided that n laser pulses were sent.

For $\eta < 0.5$ the equation B.2 will be automatically satisfied if:

$$\sum_{k=0}^{\eta*n} C_n^k \eta_{upper}^k (1-\eta_{upper})^{n-k} \leq 1-\alpha, \quad \eta_{upper} = (1+\delta(\eta))\eta$$

and for $\eta > 0.5$ the B.1 is satisfied if:

$$\sum_{k=0}^{\eta*n-1} C_n^k \eta_{lower}^k (1-\eta_{lower})^{n-k} \geq \alpha, \quad \eta_{lower} = (1-\delta(\eta))\eta$$

Therefore, for relative error $q = 0.01$, confidence $\alpha = 95\%$ and $n = 2000$ the allowed range of occupancies to be used is $0.2 < \eta < 0.8$ (see table B.1). For the phototube noise measurements ($\eta \sim 0.03$) the requirements are eased: $q = 0.1$. We also verify that using 60000 random "shots" is just enough to reach the goal. (The requirement of $q = 0.01$ is met at 66% confidence level only.)

B.3.6 Threshold effect on the occupancy measurement.

The problem addressed here is that of a finite threshold which a PMT pulse should cross in order to be recorded by the electronics. The presence of the finite threshold leads to an under estimation of the occupancy and if the final effect on the number of PEs is bigger than q a correction should be made.

The assumption of PMT operation is that electron multiplication in each stage is a statistical process with some average gain g. Then, the number of electrons k on the output of the first amplification stage obeys Poisson distribution with average gw where w is the number of photo-electrons emitted from the PMT photocathode (This assumption is similar to that of occupancy method and is based on proposition that probability of emitting an "amplified" electron does not depend on other electrons being

emitted.) and is distributed according to:

$$P(k;gw) = \frac{(gw)^k}{k!}e^{-gw}$$

It is the number of electrons on the output of the first stage that dominates the fluctuations on the output of the entire cascade and is responsible for ability of the PMT pulse to cross the discriminator threshold. The PMT electronic channel was constructed in such a way that only ρg or more electrons after the first stage will produce signal strong enough to be detected. Thus, the probability that PMT signal of strength w PEs will not be detected is:

$$\beta(w) = \sum_{k=0}^{k<\rho g} P(k;gw) = \sum_{k=0}^{k<\rho g} \frac{(gw)^k}{k!}e^{-gw}$$

and the occupancy given average number of PE λ is decreased:

$$\eta(\lambda) = 1 - P(0;\lambda) - \sum_{w=1}^{\infty} P(w;\lambda)\beta(w) = 1 - e^{-\lambda} - \lambda e^{-\lambda}\beta(1) - \frac{\lambda^2}{2}e^{-\lambda}\beta(2) - \cdots$$

For estimation purposes Milagro PMT is assumed to have uniform stage to stage amplification with typical gain of the entire PMT's cascade of $2 \cdot 10^7$ (see [4] for the measured PMT's gain at the operated voltage). Since the PMT consists of 10 stages, the gain of a single stage is $g = (2 \cdot 10^7)^{\frac{1}{10}} = 5.3$ and the threshold level is set at $\rho = 0.25$ (signals with more then 0.25 equivalent PEs will cross the discriminator threshold and will be detected.) the function $\beta(w)$ falls off rapidly and for given PMT parameters a one PE input will be lost with probability $\beta(1) = 3.1 \cdot 10^{-2}$ while 2PE — with $\beta(2) = 2.9 \cdot 10^{-4}$ and can be neglected. Hence, taking into account only the loss of 1 PE signals, the measured occupancy is equal to:

$$\eta \approx 1 - e^{-\lambda} - \beta(1)\lambda e^{-\lambda}$$

The magnitude of the correction $\beta(1)\lambda e^{-\lambda}$ has to be compared with the required accuracy on η which leads to the direct comparison of $\beta(1)$ and q.

Therefore, it is concluded that the systematic error on occupancy is comparable to the statistical one and for the desired accuracy of PE determination (few per cent) the threshold effect can be neglected. If the probabilities $\beta(1)$ are known for each PMT the

correction, could be done with the following approximate formula:

$$\lambda \approx -\frac{1}{1-\beta(1)} \ln(1-\eta)$$

Also note, the filter wheel calibration is quasi-immune from this problem because it is based on the ratio of the λ's for a given PMT and the $\frac{1}{1-\beta(1)}$ factor cancels.

B.4 Calibration Extrapolation.

The maximum light level at which the calibration data was available often was lower than could be observed in the shower data rendering strong PMT pulses unusable. To cope with this problem, extrapolation was used to infer the values of calibration parameters beyond the calibrated range based on the known values and trends. Indeed, typically it was required to extend HiToT calibrated range by about $100\ (ns)$ to interpret shower data.[2]

B.4.1 Slewing extrapolation.

The shape of the slewing correction function depends on the discriminator threshold level, amplification coefficients, gains of PMTs, wiring and so on. Instead of trying to take all the unknown parameters into account and putting together a physical model of the slewing, a statistical one was built taking the following approach.

It is believed that all PMT channels (PMTs themselves and electronic boards) were designed and manufactured to meet common characteristics. Therefore, the study of the channels' responses (calibration) can be viewed as a multiple (about 700 times) measurement of a singe function: T_{start} vs ToT. The fact that the curves obtained for different channels are slightly different can be attributed to the "manufacturing imperfections" and the channels differ only due to unavoidable uncontrollable reasons such as spread of characteristics of electronic components and/or actual slewing measurement errors. Thus, a slewing curve for a PMT can be viewed as a particular realization of some random function. All slewing curves together form one slewing function family characterized by its mean dependence[3] $m(t)$ and correlation function $K(t,t')$, by

[2] LoToT was never extrapolated as it is prudent to switch to the use of HiToT as soon as it becomes meaningful.

[3] Here, t and t' denote the time over threshold.

analogy with the mean and dispersion for a random variable.

The characteristics $m(t)$ and $K(t,t')$ of the random function were deduced from the observed high range slewing calibration data and, based on the random function framework carried out to the first order of canonical expansion, the value of the slewing correction $x(t)$ given the last known calibrated value $x(t_1)$ at time t_1 is:

$$x(t) = m(t) + \frac{x(t_1) - m(t_1)}{K(t_1,t_1)} K(t,t_1)$$

with the root mean square error of:

$$rms(t) = \sqrt{K(t,t) - \frac{(K(t,t_1))^2}{K(t_1,t_1)}}$$

Using this method slewing curves were extrapolated only to the point where real data for at least 50 PMTs existed with estimated error on extrapolation of the order of $0.7\ (ns)$.[4] Beyond that, linear extrapolation was used with the slope of $0.0381 \frac{T_{start}}{HiToT}$.

Details describing the extrapolation method used to extend slewing curves for the HiToT calibration can be found in report [16]. A brief review of the notion of random functions can be found in memo [20].

B.4.2 PE extrapolation.

Contrary to slewing calibration where the quality of the data increases with the input light level, the quality of ToT-to-PE conversion degrades due to exponential relation between ToT and PE and possible PMT saturation. This lead to the conclusion that sophisticated random function extrapolation is not justified and the extrapolation was developed based on a simple physical argument that $\log PE \sim ToT$. Thus, the PE vs ToT data was fit to a third order polynomial of the form:

$$\ln PE = a_0 + a_1 ToT + a_2 ToT^2 + a_3 ToT^3$$

and the values of the polynomial were used as the extrapolation. Needless to say that beyond approximately $PE = 100$ the error grows very fast and any algorithm relying

[4] The comparison of extrapolated data from a calibration run with calibrated data obtained independently [38] yielded the measured extrapolation error of $0.55\ (ns)$ in good agreement with the expectations.

on PE should treat the values beyond $PE = 100$ as logical “big”, “Big” and “BIG”.

B.5 Energy calibration.

It is planned that absolute energy calibration measurements will be done using through-going muons. The imaging capabilities of the detector will be exploited in order to find, fit and select well-defined through-going muon tracks. Once the geometry of the track is known, the Cherenkov energy deposit will be estimated and compared against the photo-electron distribution in the event. This was the primary absolute energy calibration method used in the IMB detector [6].

Appendix C

Auxiliary Celestial Coordinate system

An additional coordinate system on the Celestial sphere which is used in this work is defined relative to a preselected celestial object (point on the celestial sphere). The object is the origin of the coordinate grid. The "zero" axis of this coordinate system can be chosen to point to any point M on the celestial sphere.

Let $L = (\delta_L, \alpha_L)$ be the point on the Celestial sphere which should be the center of the map directed to point $M = (\delta_M, \alpha_M)$, then the point $X = (\delta_X, \alpha_X)$ on the Celestial sphere will have coordinates (χ, ξ) relative to the point L defined as (see figure C.2):

$$\chi = \overset{\smile}{LX} = \angle LCX, \quad \xi = \angle MLX$$

ξ is measured clockwise from the LM line and $\xi \in (-\pi; \pi)$, $\chi \in (0; \pi)$

From spherical triangle $\triangle LPX$:

$$\cos\chi = \cos(\overset{\smile}{LX}) = \sin\delta_L \sin\delta_X + \cos\delta_L \cos\delta_X \cos(\alpha_L - \alpha_X)$$

From spherical triangle $\triangle PMX$:

$$\cos(\overset{\smile}{MX}) = sin\delta_M \sin\delta_X + \cos\delta_M \cos\delta_X \cos(\alpha_M - \alpha_X)$$

From spherical triangle $\triangle PML$:

$$\cos(\overset{\smile}{ML}) = \sin\delta_M \sin\delta_L + \cos\delta_M \cos\delta_L \cos(\alpha_M - \alpha_L)$$

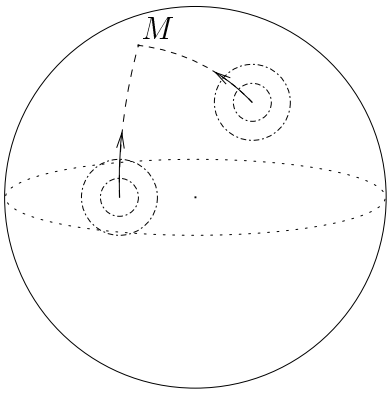

Figure C.1: Schematic of the map

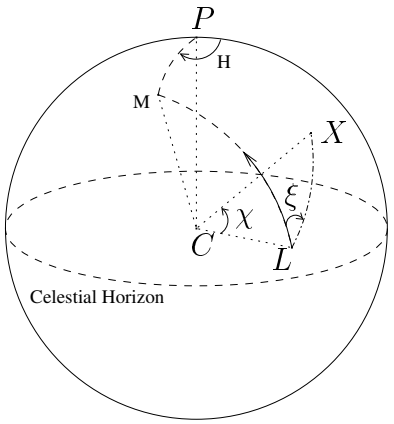

Figure C.2: Auxiliary coordinates on the Celestial sphere

From spherical triangle $\triangle MLX$:

$$\cos(\overset{\smile}{MX}) = \cos(\overset{\smile}{ML})\cos(\overset{\smile}{LX}) + \sin(\overset{\smile}{ML})\sin(\overset{\smile}{LX})\cos(MLX)$$

$$\cos\xi = \cos(\angle MLX) = \frac{\cos(\overset{\smile}{MX}) - \cos(\overset{\smile}{ML})\cos(\overset{\smile}{LX})}{\sin(\overset{\smile}{ML})\sin(\overset{\smile}{LX})}$$

There is no problem in defining the χ, however, points symmetric with respect to MCL-plane are indistinguishable. A way to solve this problem is to introduce an auxiliary vector $\vec{n} = \overrightarrow{CM} \times \overrightarrow{CL}$.[1] Then if $(\vec{n} \cdot \overrightarrow{CX}) > 0$ then $\xi \in (0; \pi)$ else $\xi \in (-\pi; 0)$.

[1] Since Right Ascensions of the objects come only in differences, the derived formulae will work in the local coordinates of (δ, H) by substituting $\alpha_* \to H_*$. However, the (δ, H) coordinate system is left-handed and the cross-product is defined in the right-handed system. Beware!

Appendix D

Kinematics of the particles in the Solar system (Simulations appendix)

D.1 `propagate_infinity().`

The task of this function is to find a particle state at infinity given its state at the annihilation point by "backward-in-time" propagation. The function, however, should return the state in "forward-time" frame since only these quantities have physical meaning. The sequence of actions to be performed is summarized below:

1. Find orientation of the orbit in space (section D.2).

2. Check that a particle crosses the Sun (section D.3). If "no", go to 6.

3. Generate column density which should be accumulated before next scattering (section D.10). Compute parameters of the inside and outside orbits (if orbit at least partially exits the Sun) (see section D.5). Propagate the particle to its first scattering point or go to 6 if the particle does not scatter. (The last situation is not possible within the considered model, but is implemented for future development.)

4. Generate scattering off of a proton (section D.9), compute the parameters of the new orbit (section D.5). Generate the column density to be accumulated until the next scattering (section D.10).

- If the particle in on unbound orbit, propagate it to the edge of the Sun, compute the Runge-Lenz vector and go to 6.
- If orbit is completely inside the Sun find the next scattering point (section D.6).
- If particle leaves the Sun, rotate the orbit according to the column density required and then, propagate the particle to the next scattering point (section D.7).

5. Go to 4.

6. Use Runge-Lenz vector to find the $\vec{v}_\infty$ or record that the particle is on a non-crossing Sun bound orbit. Perform time reflection on initial and final state (section D.7).

D.2 Conserved quantities.

In the considered model, the Sun is a ball of uniform density of mass $M_\odot$ and radius $R_\odot$. Thus, the gravitational potential $U(r)$ is the function of the distance r from the center of the Sun and is:

$$U(r) = \begin{cases} -\frac{\alpha}{r} & r \geq R_\odot \\ \frac{\alpha}{2R_\odot^3} r^2 - \frac{3\alpha}{2R_\odot} = \frac{\alpha}{2R_\odot}(\frac{r^2}{R_\odot^2} - 3) & r \leq R_\odot \end{cases}$$

where $\alpha = G_N M_\odot$ and G_N is the gravitational constant. The energy and angular momentum are conserved in such a system and are:

$$\mathcal{E} = \frac{\vec{v}^2}{2} + U(r) = \text{const}, \quad \vec{\mathcal{J}} = \vec{r} \times \vec{v} = \text{const}$$

When the particle moves outside of the Sun, its trajectory can be described by a conical section with the Sun in one of its foci. The trajectories of the particles inside the Sun are elliptical only with the center of the Sun in the center of the ellipse.

There is an additional conserved quantity when the particles is outside the Sun. It is the Runge-Lenz vector $\vec{\mathcal{K}}$:

$$\vec{\mathcal{K}} = \dot{\vec{r}} \times \vec{\mathcal{J}} - \alpha \vec{r}/r \quad |\vec{\mathcal{K}}| = \sqrt{\alpha^2 + 2\mathcal{E}\mathcal{J}^2}$$

The Runge-Lenz vector points along the major axis from focus to perihelion.

D.3 Which orbits cross the Sun.

The energy conservation law outside the Sun has the form:

$$\mathcal{E} = \frac{v_r^2}{2} + \frac{\mathcal{J}^2}{2r^2} - \frac{\alpha}{r}$$

where v_r is the radial velocity of the particle. The particle will cross the Sun if its minimum distance to the center of the Sun r_{min} is less than $R_\odot$. At this point $v_r = 0$ and:

$$\mathcal{E} = \frac{\mathcal{J}^2}{2r_{min}^2} - \frac{\alpha}{r_{min}} \quad \Rightarrow \quad r_{min} = \frac{\sqrt{\alpha^2 + 2\mathcal{E}\mathcal{J}^2} - \alpha}{2\mathcal{E}}$$

Thus, only the trajectories for which $\mathcal{J}^2 < 2R_\odot(\mathcal{E}R_\odot + \alpha)$ will cross the Sun.

A separate remark should be made regarding the unbound orbits which cross the Sun. Particles on such orbits may never cross the Sun. Indeed, if a particle is at its annihilation point and if it happens to be on an unbound orbit (as can be determined from its velocity and position vectors), the angle between its velocity and the Runge-Lenz vector should be acute for the particle to pass through the Sun. In other words, if $\mathcal{E} \geq 0$ and $\vec{\mathcal{K}} \cdot \vec{v} \leq 0$ the particle will not cross the Sun.

D.4 Rotation of a vector $\vec{B}$ around a vector $\vec{L}$ by an angle γ.

Only the proper rotations on angle γ are considered where the rotation is governed by the "right handed screw" rule around vector $\vec{L}$, $|\vec{L}| \neq 0$. The new vector $\vec{B'}$ is obtained from the original $\vec{B}$ by application of the rotation matrix $A(\gamma, \vec{L})$.

$$\vec{B'} = A(\gamma, \vec{L})\vec{B}$$

The explicit from of the transformation in Cartesian coordinates is:

$$\vec{B}' = \begin{pmatrix} B'_x \\ B'_y \\ B'_z \end{pmatrix} = \begin{pmatrix} a + cL_x^2 & cL_xL_y - bL_z & cL_xL_z + bL_y \\ cL_xL_y + bL_z & a + cL_y^2 & cL_yL_z - bL_x \\ cL_xL_z - bL_y & cL_yL_z + bL_x & a + cL_z^2 \end{pmatrix} \cdot \begin{pmatrix} B_x \\ B_y \\ B_z \end{pmatrix}$$

where

$$a = \cos\gamma \quad b = \frac{\sin\gamma}{\sqrt{L^2}} \quad c = \frac{1 - \cos\gamma}{L^2}$$

If operation of rotation of vector $\vec{\mathcal{K}}$ is performed around vector $\mathcal{J}$, a special case arises when $\mathcal{J} = 0$. In this situation the operation of rotation is not defined. However, from the physics of the situation, it follows that the rotation angle γ is either 0 or π. Thus the rotation in this case is very simple:

$$\begin{array}{ll} \text{if}\big(\gamma == \pi\big) & \vec{\mathcal{K}}' = -\vec{\mathcal{K}} \\ \text{else} & \vec{\mathcal{K}}' = \vec{\mathcal{K}} \end{array}$$

D.5 Some facts about elliptical trajectories.

In addition to the global coordinate system which is attached to the Sun and whose z axis is oriented along the Sun's motion in the Galactic disk, there are several auxiliary coordinate systems which are convenient to introduce. Both of the auxiliary coordinate systems are centered on the Sun's center and one of them is used to analyze the particle trajectory inside the Sun, and the other — outside.

Capital letters for the names of the variables will represent the trajectory which is outside the Sun and the small letters will represent the parameters for the trajectories which lie inside the Sun.

D.5.1 Equation of the ellipse.

The equation of ellipse with the coordinate system at its center is

$$\frac{x^2}{a^2} + \frac{y^2}{b^2} = 1 \quad \text{or} \quad r^2 = \frac{b^2}{1 - e^2\cos^2\phi}$$

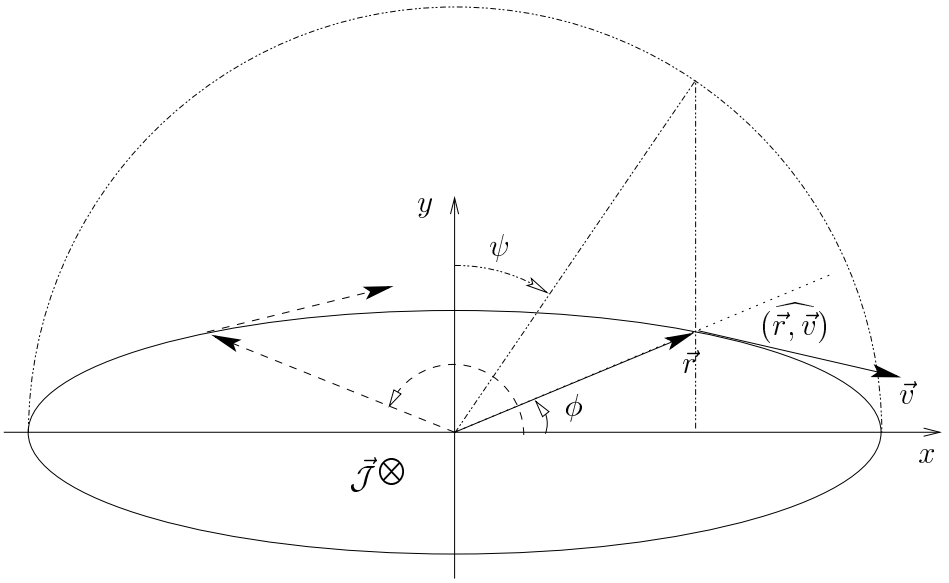

Figure D.1: Elliptical trajectory inside the Sun.

where $\phi = 0$ is the point of maximal distance from the point on ellipse to the origin (see figure D.1).

The equation of ellipse with the coordinate system at one of its foci

$$r = \frac{P}{1 + E\cos\Phi}$$

where $\Phi = 0$ is the point of minimal distance from the point on ellipse to the origin (see figure D.2).

The relationship between the semimajor axis a (or A) and semiminor one b (or B) and the eccentricity e (or E) and the latus rectum ρ (or P) is:

$$\begin{cases} e^2 = 1 - b^2/a^2 & \rho = b^2/a \\ E^2 = 1 - B^2/A^2 & P = B^2/A \end{cases}$$

D.5.2 Ellipse inside the Sun.

The parameters of the ellipse inside the Sun are:

$$\left\{ \begin{array}{l} a^2 = \frac{R_\odot^2}{\alpha}\left(\mathcal{E}' R_\odot + \sqrt{\mathcal{E}'^2 R_\odot^2 - \alpha \mathcal{J}^2 / R_\odot}\right) \\ b^2 = \frac{R_\odot^2}{\alpha}\left(\mathcal{E}' R_\odot - \sqrt{\mathcal{E}'^2 R_\odot^2 - \alpha \mathcal{J}^2 / R_\odot}\right) \end{array} \right| \quad \mathcal{E}' = \mathcal{E} + \frac{3\alpha}{2R_\odot}$$

The trajectory of a particle inside the Sun is an ellipse since the potential energy varies as distance from the Sun's center squared. Moreover, the ellipse is centered on the Sun's center. It is always possible to choose the coordinate system in such a way that the OX axis is along the semimajor axis of the ellipse and OY — the semiminor one. Because same calculations are simpler using one parameterization of an ellipse and others in another, two different ellipse parameterizations are used in this work. One is by providing the polar angle ϕ measured counterclockwise from the OX and the distance to the point from the origin r and the other is by specifying a phase angle ψ "*measured clockwise from the OY axis*" only.[1] (See figure D.1.)

The orientation of the coordinate system is chosen by requiring that at one selected point (usually initial point of propagation) if the angle between $\vec{r}$ and $\vec{v}$ is acute, the phase angle ψ of the point should be between zero and $\pi/2$ and between $-\pi/2$ and zero if the angle is obtuse (see fig D.1).

The equations of the same ellipse in different parameterizations are:

$$\left\{ \begin{array}{l} x = a\sin\psi = \sqrt{\frac{b^2}{1-e^2\cos^2\phi}}\cos\phi \\ y = b\cos\psi = \sqrt{\frac{b^2}{1-e^2\cos^2\phi}}\sin\phi \end{array} \right| \Rightarrow \left\{ \begin{array}{l} \tan\phi = \frac{b\cos\psi}{a\sin\psi} \\ r^2 = b^2 + (a^2-b^2)\sin^2\psi = \frac{b^2}{1-e^2\cos^2\phi} \end{array} \right| \tag{D.1}$$

The length s of the elliptical arc between the angles ψ_1 and ψ_2 is:

$$\left\{ \begin{array}{l} dx = a\cos\psi\, d\psi \\ dy = -b\sin\psi\, d\psi \end{array} \right| \Rightarrow (ds)^2 = (dx)^2 + (dy)^2 = a^2\left[1 - \frac{a^2-b^2}{a^2}\sin^2\psi\right](d\psi)^2$$

$$ds = a\sqrt{1 - e^2\sin^2\psi}\, d\psi, \quad e^2 = 1 - b^2/a^2$$

$$s = a\int_{\psi_1}^{\psi_2}\sqrt{1 - e^2\sin^2\psi}\, d\psi$$

Thus, the length of an elliptical arc can be expressed in terms of the elliptical inte-

[1] The angle $(\pi/2 - \psi)$ is called the eccentric anomaly in celestial mechanics.

gral:

$$EE(\theta, k) = \int_0^\theta \sqrt{1 - k^2 \sin^2 t}\, dt, \quad k^2 < 1 \;\; \theta \in [0; \pi/2]$$

D.5.3 Angle between $\vec{r}$ and $\vec{v}$.

If current position $\vec{r}$ and velocity $\vec{v}$ are known, it is easy to find the angle $(\widehat{\vec{r}, \vec{v}})$ between the two:

$$\cos(\widehat{\vec{r}, \vec{v}}) = \frac{\vec{r} \cdot \vec{v}}{rv}$$

If velocity $\vec{v}$ is not known, but the the phase angle ψ corresponding to the position $\vec{r}$ on the ellipse is known it is possible to find the angle between $\vec{r}$ and $\vec{v}$. Inside the Sun, the energy conservation law is:

$$\mathcal{E} = \frac{v^2}{2} + \frac{\alpha}{2R_\odot^3} r^2 - \frac{3\alpha}{2R_\odot} \quad \Rightarrow \quad v^2 = \left(2\mathcal{E}' R_\odot - \alpha \frac{r^2}{R_\odot^2} \right) / R_\odot \tag{D.2}$$

$$\vec{\mathcal{J}} = \vec{r} \times \vec{v} \;\; \Rightarrow \;\; |\vec{\mathcal{J}}| = |\vec{r}| \cdot |\vec{v}| \sin(\widehat{\vec{r}, \vec{v}}) \;\; \Rightarrow \;\; \sin(\widehat{\vec{r}, \vec{v}}) = \frac{\mathcal{J}}{rv} = \sqrt{\frac{\mathcal{J}^2}{r^2 v^2}}$$

$$(\widehat{\vec{r}, \vec{v}}) = \begin{cases} \arcsin(\sqrt{\frac{\mathcal{J}^2}{r^2 v^2}}), & \psi \in [-\pi; -\pi/2] \bigcup [0; \pi/2] \;\; \Leftrightarrow \;\; \tan\psi \geq 0 \\ \pi - \arcsin(\sqrt{\frac{\mathcal{J}^2}{r^2 v^2}}), & \psi \in [-\pi/2; 0] \bigcup [\pi/2; \pi] \;\; \Leftrightarrow \;\; \tan\psi \leq 0 \end{cases} \tag{D.3}$$

To find $\vec{v}$ it is enough to rotate the vector $\vec{r}$ around $\vec{\mathcal{J}}$ by angle $(\widehat{\vec{r}, \vec{v}})$ (see figure D.1) and rescale appropriately:

$$\vec{v} = \frac{v}{r} \texttt{rotate_vector}(\vec{r}, \vec{\mathcal{J}}, (\widehat{\vec{r}, \vec{v}}))$$

D.5.4 Ellipse outside the Sun.

The parameters of the ellipse outside the Sun are:

$$E^2 = 1 + \frac{2\mathcal{E}\mathcal{J}^2}{\alpha^2} \quad P = \mathcal{J}^2/\alpha$$

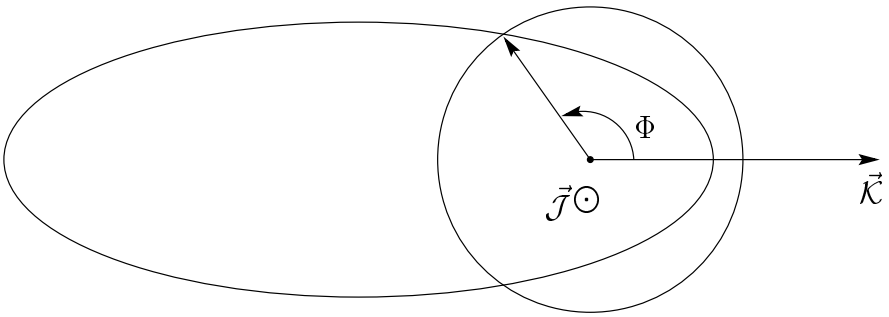

Figure D.2: Elliptical trajectory outside the Sun.

The bound trajectory while outside the Sun is an ellipse with the center of the Sun at one of its foci ("the outside ellipse"or "the outside orbit"). It is interesting to find the angle Φ between the Runge-Lenz vector (the direction on the perihelion) and the point where the outside ellipse intersects the Sun (see figure D.2). This angle is easily found from the equation of the outside ellipse:

$$\frac{P}{R_\odot} = 1 + E\cos\Phi$$

$$\cos\Phi = \frac{1}{E}\left(P/R_\odot - 1\right) = \frac{\mathcal{J}^2 - \alpha R_\odot}{E\alpha R_\odot} \tag{D.4}$$

D.5.5 Rotation of outside orbit due to passage through the Sun.

The angle of rotation of the orbit in a single pass through the Sun is defined as the angle of rotation of Runge-Lenz vector due to this passage.

If γ is angle of rotation of the orbit as it passes through the Sun, and Φ_0 is the coordinate describing the point of entrance of the orbit into the Sun and ϕ_0 is direction to the same point, but with respect to the orbit which is inside the Sun, we obtain the relationship for the angle of rotation of the orbit (see figure D.3):

$$\phi_0 = \Phi_0 + (\pi/2 - \gamma/2) \quad \Rightarrow \quad \gamma = \pi + 2\Phi_0 - 2\phi_0$$

From the equation (D.4) Φ_0 can be obtained:

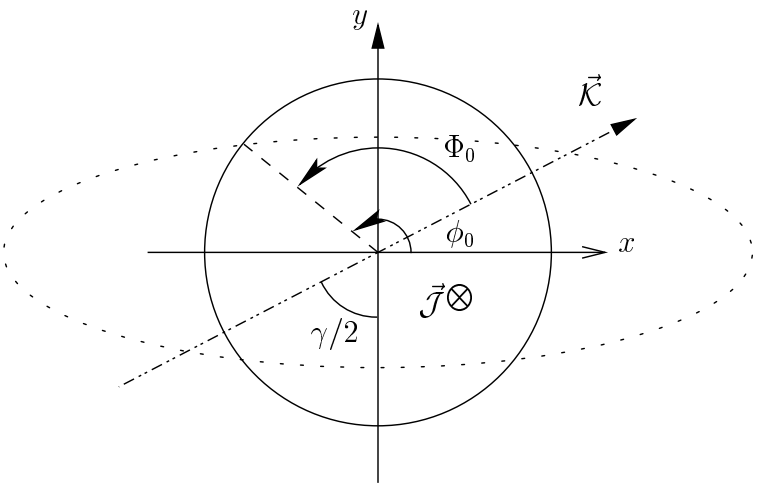

Figure D.3: Rotation of the outside orbit due to passage through the Sun.

$$\Phi_0 = \arccos\left(\frac{\mathcal{J}^2 - \alpha R_\odot}{E\alpha R_\odot}\right)$$

From the equations (D.1) and (D.3) the phase and spatial angles of the entrance point of the orbit into the Sun are:

$$\sin\psi_0 = -\sqrt{\frac{R_\odot^2 - b^2}{a^2 - b^2}} \qquad \tan\phi_0 = \frac{b\cos\psi_0}{a\sin\psi_0} \tag{D.5}$$

The "$-$" sign is selected since at the entrance point into the Sun $(\vec{r}\cdot\vec{v}) < 0$ always.

Rotation of the Runge-Lenz vector $\vec{\mathcal{K}}$ happens on the angle $(-\gamma)$ around $\vec{\mathcal{J}}$ in one passage of the orbit through the Sun.

D.6 Motion inside the Sun `propagate_in_sun()`.

Only the motion which is initialized from inside and while inside the Sun is treated here. That is, the task considered here is knowing the requested column density to evolve a particle from its initial position and velocity inside the Sun to the scattering point inside the Sun or if the particle exits the Sun — output the new direction of Runge-Lenz vector

and the remaining column density to be accumulated in subsequent passes through the Sun.

There are several situations possible:

- The orbit is completely inside the Sun. Propagate the particle to its next scattering. Output final $\vec{r}$ and $\vec{v}$.
- The orbit exits the Sun and column density to be accumulated is large to allow the particle to exit the Sun. Output the final Runge-Lenz vector $\vec{\mathcal{K}}$.
- The orbit exits the Sun geometrically, but the column density to be accumulated is not large enough. Particle scatters before its exist. Output $\vec{r}$ and $\vec{v}$ just before the scattering.

D.6.1 Particle is inside the Sun.

An orbit lies completely inside the Sun if the semimajor axis of the ellipse is not larger than the radius of the Sun: $a \leq R_\odot$. The phase angle ψ_1 and the spatial angle ϕ_1 corresponding to the current position $\vec{r}_1$ inside the Sun can be found from the equation of the ellipse in phase coordinates (see equations (D.3) and (D.1)):

$$\begin{gathered}\sin\psi_1 = sign(\vec{r}_1 \cdot \vec{v}_1)\sqrt{\frac{r_1^2 - b^2}{a^2 - b^2}}, \qquad \psi_1 \in [-\pi/2; \pi/2] \\ \tan\phi_1 = \frac{b\cos\psi_1}{a\sin\psi_1}\end{gathered} \tag{D.6}$$

The final angles ψ_2 and ϕ_2 are such that the column density accumulated by a particle traveling inside the Sun is equal to the specified column density L. Currently, the equation formulated in the phase angles is considered:

$$L = \texttt{trajectory_length}(\psi_1, \psi_2)$$

This equation can be solved (see section D.8) and the corresponding spatial angle is:

$$\tan\phi_2 = \frac{b\cos\psi_2}{a\sin\psi_2}$$

Now, the sought for direction of $\vec{r}_2$ can be found by rotating the vector $\vec{r}_1$ on angle $-(\phi_2 - \phi_1)$ around $\vec{\mathcal{J}}$ and the magnitude of $\vec{r}_2$ an be found from the equation of the

ellipse (D.1):

$$r_2^2 = b^2 + (a^2 - b^2)\sin^2\psi_2 \qquad \vec{r}_2 = \texttt{rotate_vector}(\vec{r}_1, \vec{\mathcal{J}}, \phi_1 - \phi_2) \cdot \sqrt{\frac{r_2^2}{|\vec{r}_1|^2}}$$

The velocity vector $\vec{v}_2$ at the point $\vec{r}_2$ can be found by rotating the vector $\vec{r}_2$ on the angle between $\vec{r}_2$ and $\vec{v}_2$ obtained from the equation (D.3). The magnitude of $\vec{v}_2$ is found from the energy conservation law (D.2).

In the case of a circular orbit $a \equiv b$ and the previous logic will fail because the initial phase ψ_1 is arbitrary and the most appealing choice is to set $\psi_1 = 0$. The logic of the presented algorithm is intact.

D.6.2 Orbit exits the Sun, but the particle doesn't.

It is possible to have a situation where a particle has its initial position inside the Sun, but its orbit leaves the Sun geometrically. It is also possible, however, that the column density to be accumulated is small and the particle scatters before it has a chance to exit the Sun. This is case of motion confined to the interior of the Sun and was treated above. To make sure that the particle stays inside the Sun, the column density which can be accumulated until the exit from the Sun should be greater than the requested column density L:

$$L < \texttt{trajectory_length}(\psi_1, \psi_{R_\odot})$$

where ψ_1 is the initial phase defined in equation (D.6) and $\psi_{R_\odot}$ is the phase of the exit point from the Sun and computed as in equation (D.1):

$$\sin\psi_{R_\odot} = +\sqrt{\frac{R_\odot^2 - b^2}{a^2 - b^2}} \tag{D.7}$$

If it is found that the requested column density is greater than maximum possible in the configuration, the particle leaves the Sun and this case is treated right below.

D.6.3 Particle exits the Sun.

Again, as before, ϕ_1, ψ_1 describe the initial point (equation (D.6)) and ϕ_2,ψ_2 is the final point of propagation — the point of orbit exit from the Sun (see equations (D.1) and

(D.7), $\psi_2 \equiv \psi_{R_\odot}$):

$$\sin\psi_2 = +\sqrt{\frac{R_\odot^2 - b^2}{a^2 - b^2}}, \quad \tan\phi_2 = \frac{b\cos\psi_2}{a\sin\psi_2} \tag{D.8}$$

The accumulated column density inside the Sun between angles ψ_1 and ψ_2 should be computed and subtracted from the remaining column density.

The spatial angle between the initial point $\vec{r}_1$ and the Runge-Lenz vector $\vec{\mathcal{K}}$ consists of the angle between the initial point and the exit point from the Sun $(\phi_1 - \phi_2)$ and the angle Φ_2 between the exit point from the Sun and the Runge-Lenz vector which is found from equation (D.4). Therefore, the vector $\vec{r}_1$ should be rotated by $(\phi_1 - \phi_2 - \Phi_2)$ around the $\vec{\mathcal{J}}$ with `rotate_vector`$(\vec{r}_1, \vec{\mathcal{J}}, (\phi_1 - \phi_2 - \Phi_2))$ to find the direction of the Runge-Lenz vector.

D.7 Motion outside the Sun `propagate_outside_sun()`.

The task of this function is given the direction of the Runge-Lenz vector and the column density `column_density` to be accumulated inside the Sun until the next scattering point find the particle position and velocity at the scattering point. Needless to say, the function should process only the particles which pass through the Sun. The other parameters which are expected to be available are the parameters of the orbit inside the Sun and the phase angle ψ_2 defined in the equation (D.8).

There could be several distinct cases:

1. The trajectory is an ellipse

2. The trajectory is a hyperbola or parabola (but the particle crosses the Sun)

D.7.1 Find the scattering point.

The parameters of the trajectory do not change between scatterings and only rotation of the whole orbit is possible as the orbit passes through the Sun. The angle γ of orbit rotation due to a single pass through the Sun was obtained in section D.5.5. The number of required passes through the Sun can be be determined from the required column

density to be accumulated and the column density accumulated in a single pass through the Sun. This will give the total angle of the orbit rotation before the scattering.

Due to spherical symmetry of the Sun, the column density accumulated in one pass through the Sun has the form of (see section D.5.2 and equation (D.7)):

$$L_1 = 2 \cdot \texttt{trajectory_length}(0, \psi_{R_\odot})$$

The total angle $n \cdot \gamma$ of rotation of the orbit is:

$$n \cdot \gamma = \texttt{floor(column_density}/L_1\texttt{)} \cdot \gamma$$

$$\texttt{column_density} := \texttt{column_density} - nL_1$$

From figures D.2 and D.3, one sees that the vector pointing to the entrance point into the Sun can be found by rotating the Runge-Lenz vector by angle $(-\Phi_0)$, that is why the total rotation of $\vec{\mathcal{K}}$ to be performed is on angle $(-n\gamma - \Phi_0)$ around $\vec{\mathcal{J}}$.

The remaining problem is to find the angle between the point of entrance into the Sun and the scattering point using the remaining column density to be accumulated. The particle will spend remaining time on an ellipse inside the Sun, and the phase angle at the scattering point ψ_1 can be found given the remaining column density and the phase angle ψ_0 (equation (D.5)) of particle entrance into the Sun (see section D.8):

$$\texttt{column_density} = \texttt{trajectory_length}(\psi_0, \psi_1) \quad \Rightarrow \quad \tan\phi_1 = \frac{b\cos\psi_1}{a\sin\psi_1}$$

Now, the sought for scattering point $\vec{r}_1$ can be found by rotating the vector $\vec{\mathcal{K}}$ on angle $(-n\gamma - \Phi_0 + \phi_0 - \phi_1)$ around $\vec{\mathcal{J}}$ and the magnitude of $\vec{r}_1$ an be found from the equation of the ellipse (D.1):

$$r_1^2 = b^2 + (a^2 - b^2)\sin^2\psi_1 \quad \vec{r}_1 = \texttt{rotate_vector}(\vec{\mathcal{K}}, \vec{\mathcal{J}}, -n\gamma - \Phi_0 + \phi_0 - \phi_1) \cdot \sqrt{\frac{r_1^2}{|\vec{\mathcal{K}}|^2}}$$

The velocity vector $\vec{v}_1$ at the point $\vec{r}_1$ can be found by rotating the vector $\vec{r}_1$ on the angle between $\vec{r}_1$ and $\vec{v}_1$ obtained from the equation (D.3) around vector $\vec{\mathcal{J}}$. The magnitude of $\vec{v}_1$ is found from the energy conservation law (D.2).

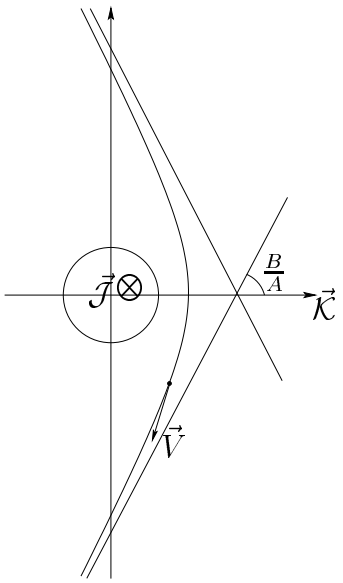

Figure D.4: Finalize

D.7.2 Particle on an unbound orbit crossing the Sun.

This situation can occur if a particle is generated on a hyperbolic or parabolic orbit, but it passes through the Sun. If the requested column density is smaller than can be accumulated in one passage through the Sun, the above logic will suffice. If however, the requested column density can not be accumulated in a single pass, the particle will leave the Solar system, thus, in the previous calculations the angle of orbit rotation due to passage through the Sun is equal to γ from the section D.5.5 only. The output of the function in this case is the final direction of the Runge-Lenz vector and is found by rotating the input Runge-Lenz vector on the angle $(-\gamma)$ around $\vec{\mathcal{J}}$.

D.7.3 Velocity at infinity.

This is the final function and its task is to find the velocity of the particle at infinity. Since only "forward" in time information is needed, this function should perform time-reflection on the initial and final velocities of the particle.

The time reflection can be performed in the spherical coordinates by requiring the change in the polar angle $\theta \to (\pi - \theta)$ and in the azimuth $\phi \to (\pi + \phi)$modulo(2π).

A particle can exit the Solar system only when it is on a hyperbolic or a parabolic trajectory when $\mathcal{E} \geq 0$. The direction of the velocity at infinity can coincides with the direction of the trajectory asymptote. Thus, the velocity direction can be found by rotating the Runge-Lenz vector to point to the asymptote (see figure D.4) by angle $(\pi - \arctan B/A)$.

$$\frac{B}{A} = \frac{\mathcal{J}}{\sqrt{2\mathcal{E}}}\frac{2\mathcal{E}}{\alpha} = \frac{1}{\alpha}\sqrt{2\mathcal{E}\,\mathcal{J}^2}$$

and the magnitude of the velocity can be found from the energy conservation law:

$$v_\infty = \sqrt{2\mathcal{E}}$$

The above works for the Solar system escape on a parabolic orbit too, because in this case the particle starts its fall into the Solar system in $(\vec{\mathcal{K}})$ direction. Even though $\vec{v}_\infty = 0$ in this case, it is necessary to know the direction in which the particle started to fall onto the Solar System, that is why $\vec{v}_\infty$ should be stored in spherical coordinates providing the information about the magnitude and the direction of the velocity even if $|\vec{v}_\infty| = 0$.

If $\mathcal{E} < 0$ and the particle does not cross the Sun, it stays on closed bound orbit around the Sun and the velocity at infinity is not defined.

D.8 SolvePath4Psi.

The task of the function is given initial point on an ellipse inside the Sun via its phase angle ψ_{in} find the point ψ_{out} such that the ellipse pathlength from ψ_{in} to ψ_{out} is equal to the given value of `path_in`. If such a point is found, its phase ψ_{out} is returned. If the point can not be found because the particle leaves the Sun before the requested pathlength is accumulated, the `path_in` is decreased by the path traveled in the Sun and ψ_{out} is set to the exit point from the Sun.

The length of an ellipse from point $\psi = 0$ to ψ is found by the elliptical integral:

$$EE(\psi, e) = sign(\psi) \cdot \int_0^\psi \sqrt{1 - e^2 \sin^2 t}dt$$

where e is eccentricity of the ellipse and $|\psi| < \pi/2$.

Thus, elliptical distance between two points on ellipse is

$$L(\psi_{in}, \psi_{out}) = a\Big(EE(\psi_{out}, e) - EE(\psi_{in}, e)\Big)$$

The problem with this definition is that both initial ψ_{in} and final ψ_{out} phases should be less than $\pi/2$, otherwise, the definition of the distance on the ellipse must be modified.

The initial phase ψ_{in} is within allowed range by its construction.

D.8.1 Bracketing the root.

If the orbit exits the Sun, both ψ_{in} and ψ_{out} are within allowed bounds since the phase for the exit point $\psi_{out} \leq \psi_R \leq \pi/2$.

If the pathlength `path_in` is larger than the path from ψ_{in} to ψ_R the particle exits the Sun. The path $L(\psi_{in}, \psi_R)$ is subtracted from `path_in` and the remaining `path_in` and ψ_R are returned with a flag that the particle exited the Sun.

Otherwise, the particle stays inside the Sun even though, its orbit geometrically exits the Sun and $\psi_{in} < \psi_{out} < \psi_R$. The root bracket is found. If the ellipse is completely inside the Sun, more things have to be done.

If the total requested pathlength `path_in` is greater than the length of ellipse, particle will make one or several full revolutions which are not interesting for us. Pathlength `path_in` should be reduced by the path acquired in full revolutions. After this is done, ψ_{out} is within: $\psi_{in} < \psi_{out} < 2\pi + \psi_{in}$. The problem is reduced to the one where the particle does not make a full revolution in the Sun.

Since it is known that the particle makes less than a full revolution, a check can be made if $\psi_{out} < \pi/2$ and $\psi_{out} < 3\pi/2$ by comparing `path_in` with $L(\psi_{in}, \pi/2)$ and $\Big(L(\psi_{in}, \pi/2) + L(-\pi/2, \pi/2)\Big)$.

If it is found that the solution is in $\psi_{out} < \pi/2$ the lower bound on the root ψ_l is set to ψ_{in} and the upper ψ_u to $\pi/2$.

If it is found that the solution is in $\pi/2 < \psi_{out} < 3\pi/2$, the pathlength $L(\psi_{in}, \pi/2)$ is subtracted from `path_in` and ψ_{in} is reset to to $-\pi/2$, ψ_l is set to $-\pi/2$, and the upper bound ψ_u is set to $\pi/2$. This effectively produces a rotation of the coordinate system by the angle of π. Thus, after the root is found, its value will have to be increased by π.

If it is found that the solution is in $\psi_{out} \geq 3\pi/2$, the pathlength $L(\psi_{in}, 3\pi/2) = \Big(L(\psi_{in}, \pi/2) + L(-\pi/2, \pi/2)\Big)$ is subtracted from `path_in` and ψ_{in} becomes the upper bound on the root $\psi_u = \psi_{in}$. The lower bound on the root ψ_l is set to $-\pi/2$ and ψ_{in} is

reset to to $-\pi/2$. This effectively produces a rotation of the coordinate system by the angle of 2π. Thus, after the root is found, its value will have to be increased by 2π.

When the algorithm arrives to this point, the bracketing of the root is finished:

$$-\pi/2 \leq \psi_l \leq \psi_{out} \leq \psi_u \leq \pi/2 \text{ with possible flag to increase } \psi_{out} \text{ by } \pi \text{ or } 2\pi.$$

D.8.2 Circular bracketing.

The phase angle interval can be reduced further by noticing that the length of the arc of radius of semimajor axis a is not smaller than the length of the ellipse within the same boundaries on the phase angle ψ. Likewise, the length of the arc of the semiminor axis radius b is not greater than the length of the ellipse within the same boundaries on the phase angle ψ. In other words, the solution ψ_{out} can be bracketed as:

$$\psi_1 \leq \psi_{out} \leq \psi_2, \quad \psi_1 = (\psi_l + 2\pi/a) \quad \psi_2 = min\Big((\psi_l + 2\pi/b), \psi_u\Big)$$

D.8.3 The solution.

The equation for ψ_{out} which needs to be solved is:

$$L(\psi_{in}, \psi_{out}) = \texttt{path_in}$$

This equation can be solved on the specified interval $(\psi_1; \psi_2)$ using the secant or bisection method until the error on accumulated pathlength L becomes within allowed range. (It was found that for $e > 0.99$, when the ellipse is close to degeneration into a line, the bisection method is faster than the secant.)

The solution of this equation should be increased by π or 2π if coordinate system rotation was required as described before.

D.9 Scattering in the Sun.

Let momenta of a neutralino and a scatterer (proton) before scattering in the laboratory reference frame be $\vec{p}_\chi$ and $\vec{p}_p$ and after $\vec{p}\,'_\chi$ and $\vec{p}\,'_p$ accordingly. It should be noted that two vectors $\vec{p}_\chi$ and $\vec{p}\,'_\chi$ form a plane thus $\vec{p}_\chi$ can be found from $\vec{p}\,'_\chi$ by a rotation. The magnitude and the angle of rotation can be found from the kinematics of the elastic scattering. The axis of rotation has a random direction in space.

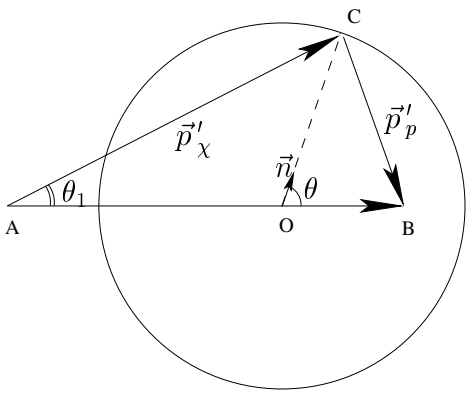

Figure D.5: Scattering diagram. $\vec{AO} = \frac{m_\chi}{m_\chi+m_p}(\vec{p}_\chi + \vec{p}_p)$, $\vec{OB} = \frac{m_p}{m_\chi+m_p}(\vec{p}_\chi + \vec{p}_p)$, $\vec{OC} = |\mu\vec{v}|\vec{n}$.

D.9.1 Elastic scattering.

In the center-of-mass frame, the momenta before scattering are:

$$\left\{ \begin{array}{l} \vec{p}_{\chi 0} = \mu\vec{v} \\ \vec{p}_{p0} = -\mu\vec{v} \end{array} \right| \quad \mu = \frac{m_\chi m_p}{m_\chi + m_p} \quad \vec{v} = \frac{\vec{p}_\chi}{m_\chi} - \frac{\vec{p}_p}{m_p}, \quad \mu v = \frac{1}{\eta+1}|\vec{p}_\chi - \eta\vec{p}_p| \quad \eta = \frac{m_\chi}{m_p}$$

In the center-of-mass reference frame, the act of elastic scattering can change the directions of the momenta only [2]:

$$\left\{ \begin{array}{l} \vec{p}\,'_{\chi 0} = \mu v\vec{n} = \frac{1}{\eta+1}|\vec{p}_\chi - \eta\vec{p}_p|\vec{n} \\ \\ \vec{p}\,'_{p0} = -\mu v\vec{n} = -\frac{1}{\eta+1}|\vec{p}_\chi - \eta\vec{p}_p|\vec{n} \end{array} \right.$$

where $\vec{n}$ is a unit vector along the velocity of the neutralino after the collision. In laboratory reference frame:

$$\left\{ \begin{array}{l} \vec{p}\,'_\chi = \mu v\vec{n} + \frac{m_\chi}{m_\chi+m_p}(\vec{p}_\chi + \vec{p}_p) = \frac{1}{\eta+1}|\vec{p}_\chi - \eta\vec{p}_p|\vec{n} + \frac{m_\chi}{m_\chi+m_p}(\vec{p}_\chi + \vec{p}_p) \\ \\ \vec{p}\,'_p = -\mu v\vec{n} + \frac{m_p}{m_\chi+m_p}(\vec{p}_\chi + \vec{p}_p) = -\frac{1}{\eta+1}|\vec{p}_\chi - \eta\vec{p}_p|\vec{n} + \frac{m_p}{m_\chi+m_p}(\vec{p}_\chi + \vec{p}_p) \end{array} \right.$$

[2] This is merely a statement of the energy conservation law

The task is to find the $\vec{p}_\chi$ when $\vec{p}\,'_\chi$ is known. If in the laboratory frame the scatter is at rest before the scattering $\vec{p}_p = 0$, then (see figure D.5): $\vec{OB} = \mu\vec{v}$ $\vec{AB} = \vec{p}_\chi$ and point B is on the sphere. In this case, the angle of deflection of neutralino velocity θ_1 from its original direction is related to the scattering angle θ in the center-of-mass frame as:

$$\tan\theta_1 = \frac{m_p \sin\theta}{m_\chi + m_p\cos\theta} = \frac{\sin\theta}{\eta + \cos\theta}$$

and

$$|\vec{p}_\chi| = |\vec{p}\,'_\chi|\frac{m_\chi + m_p}{\sqrt{m_\chi^2 + m_p^2 + 2m_\chi m_p\cos\theta}} \;\Rightarrow\; |\vec{v}_\chi| = |\vec{v}\,'_\chi|\frac{\eta+1}{\sqrt{\eta^2 + 2\eta\cos\theta + 1}}$$

$$|\vec{v}_\chi|^2 = |\vec{v}\,'_\chi|^2\frac{\eta^2 + 2\eta + 1}{\eta^2 + 2\eta\cos\theta + 1}$$

The energy loss in a collision is:

$$\frac{\left(|\vec{v}_\chi|^2 - |\vec{v}\,'_\chi|^2\right)}{2} = \frac{2\eta(1-\cos\theta)}{(1+\eta)^2}\cdot\frac{|\vec{v}_\chi|^2}{2}$$

D.9.2 Choosing the axis of rotation.

Vectors $\vec{v}_\chi$ and $\vec{v}\,'_\chi$ from a plane which is defined by some vector $\vec{n}$. A vector $\vec{n}$ perpendicular to $\vec{v}\,'_\chi$ can be found by solving:

$$\vec{v}\,'_\chi \cdot \vec{n} = 0 \;\Rightarrow\; v'_x n_x + v'_y n_y + v'_z n_z = 0$$

This equation can be solved by setting trial coordinates for the vector $\vec{n} = (1,1,1)$ and then modifying one of the coordinates to satisfy the orthogonality condition:

if $(v'_z \neq 0)$	$n_z := -(v'_x + v'_y)/v'_z$
else if $(v'_y \neq 0)$	$n_y := -v'_x/v'_y$
else	$n_x := 0$

Then, the obtained vector $\vec{n}$ can be rotated on a random angle around $\vec{v}'_\chi$ which will produce a vector perpendicular to $\vec{v}'_\chi$ and pointing in a random direction in space. The obtained vector defines the $(\vec{v}'_\chi, \vec{v}_\chi)$ plane.

D.10 Generate path inside the Sun.

The probability dp that a particle will travel distance x through matter without scattering and then scatter immediately after that in the distance $(x, x + dx)$ is:

$$dp = \frac{1}{\lambda} e^{-x/\lambda}\, dx$$

where λ is the mean free path of the particle in matter.

Thus, the pathlength which need to be accumulated in the Sun until next scattering should be drawn from an exponential distribution with parameter λ.

$$\lambda = \frac{1}{\sigma_{p\chi} n_p}$$

n_p is the concentration of the scatterers and $\sigma_{p\chi}$ is the crossection of the scattering process. In the given model $n_p = \frac{M_\odot}{\frac{4}{3}\pi R_\odot^3 m_p}$, m_p is the mass of scatterers (protons).

Appendix E

Comments on the upper limit construction procedure

Very often physicists consider the question of validity of a new theory to be equivalent to a non-zero value of the parameter(s) of the theory. Thus, often, the tests of validity of a new theory are designed in such a way as to measure the value(s) of its parameter(s). If the measured value is non-zero it is concluded that the new theory is valid with the obtained value of the parameter. Such a "physical" approach seems to give adequate results but is not correct from a methodological point of view. Indeed, one can always assume that some theory is correct and obtain a non-zero value for the parameter of the theory based on the experiment, but that does not mean that the theory correctly describes the observed process. Also, if the measurement was "not successful", that is, the experiment could not show that the value of the parameter is non-zero, it is not possible to decide if the new theory is valid or not. And more importantly, the new theory might not even have a free parameter to be measured.

In the defining work by Neyman [39] on statistical estimation the question of a statistical test is separated from the question of the measurement. The procedure for parameter estimation (measurement) demands that it is known that the process, whose parameter is being measured, exists and the observed data is described by the known distribution with the parameter being measured. If it is not the case, the procedure can not guarantee that the constructed confidence interval will contain the true value of the parameter with requested probability. This fact if often overlooked.

When a new theory is proposed the experiment should not try to estimate the value of the parameter of the theory, but, instead, it should be designed to exploit the differences

between the adopted (old) and the new theories and check if indeed there is evidence to reject the old one. It is the difference between the old and the new theories which provides the "signal" in the test. The test of the validity of the new theory should be designed in the spirit of the proof by contradiction (also called indirect proof) method. In other words, it should be assumed that the new theory is wrong and the old one is correct. If the contradiction between the old theory and observed data is found (i.e. the "signal" is found), the assumption of validity of the old theory should be rejected and the new theory may be accepted as a valid one. If the contradiction is not found, nothing can be said regarding the validity of the new theory and the old theory can not be rejected in favor of the new one due to lack of evidence.

E.1 Sensitivity and upper limit.

There is a question which an experimenter should answer when designing the experiment: what is the probability to accept H_0 due to pure chance when H_1 is true i.e. what is the power of the constructed test. The power of the test depends on the alternative hypothesis and its parameters as well as on the null hypothesis. If a new theory provides a large power of the test and is true, the contradiction between the observed data and the old theory will be found easily by the constructed test. If, on the other hand, the new theory provides small power if it is true, the contradiction between the observed data and the old theory will not be found easily. It is seen that the "strength" of a "signal" is defined in terms of the power of the test. The new theory predicts a "strong" detectable "signal" if it provides large power of the test.

Suppose that the alternative hypothesis has the form of $p_1(x;\lambda)$ where x is observed quantity and λ is the parameter of the new theory. For some values of λ the power of the test will be small and for others the power will be big. It is proposed to define "sensitivity" of the test (or experiment) as such values of the parameter λ for which the test has the power of at least 50%. The sensitivity defined this way has several important properties: it is a detector feature and can be estimated before the experiment is performed, it is not a random number and does not depend on the value of the observed quantity.

It is also proposed to state the upper limit when H_0 is not rejected as such values of λ for which the power of the test is big (say at least 90%). The choice is motivated by the logic that it is hard to miss such a strong "signal" and yet it was not observed. In other words the values of λ for which there is a big chance to not reject the null hypothesis are

below the upper limit and the values of λ for which the chance to reject H_0 is big can be dismissed when H_0 was not rejected based on the observed data.

E.2 Problem with the current approach.

Currently, the upper limit on the value of the parameter λ of a theory is reported as the upper boundary of the one-sided confidence interval on the parameter which is obtained assuming that the data came from a distribution characterized by $p_1(x;\lambda)$. This is, however, true and correct only in the cases when the physical process originating the observed data exists and according to the theory is described by $p_1(x;\lambda)$. Again, only if there is no question of existence of the process is it correct to use the procedure for confidence interval construction for parameter estimation. Note that the bounds of the confidence interval are random by nature because they are functions of a random variable and will vary with the data observed.

The application of the same technique to construction of a confidence interval on λ due to a process which is not known to exist when the hypothesis of absence of this process is not rejected based on the observed data will lead to meaningless results. The constructed confidence interval will not have the desired confidence level and more over, the theory H_0 which has no parameter λ has not been rejected based on the observed data. It is irrational and illogical to assume the validity of H_1 when H_0 is not rejected.

E.3 Example I.

Let us consider a situation when according to the old adopted theory a quantity X is distributed according to Gaussian law with zero mean and known standard deviation σ:

$$p_0(x) = \frac{1}{\sqrt{2\pi\sigma^2}} e^{-x^2/2\sigma^2}$$

If a new theory is correct, the data X should be distributed according to the Gaussian distribution with positive mean λ:

$$p_1(x;m) = \frac{1}{\sqrt{2\pi\sigma^2}} e^{-(x-\lambda)^2/2\sigma^2} \quad \lambda > 0$$

Let us assume that if $x > 3\sigma$ the old theory is rejected and a confidence interval on

the values of λ may be constructed. If $X < 3\sigma$ the old theory is not rejected and an upper limit on the values of λ should be set with the confidence of 90% (or 1.28σ).

Further, let us assume that the outcome of the measurement is $x = 0$, which is the most probable outcome when the old theory is true. According to the current approach, the upper limit on the λ would be $\lambda < 1.28\sigma$ (This is a standard one-sided confidence interval on λ with 90% confidence.)

Now, suppose that the new theory is true with the parameter $\lambda = 1.29\sigma$. This signal is above the upper limit. What is the probability of discovering the signal in this experiment or what is the power of the test? For a discovery to happen $x > 3\sigma$ should be observed which has a probability of happening of 5% only. Therefore, the experiment which set a limit of $\lambda < 1.28\sigma$ has almost no capability to discover a stronger signal. This is clearly unsatisfactory result.

Using the approach proposed here, it is required to state the upper limit corresponding to 90% power of the test. Since in the observed data $x < 3\sigma$. no discovery is made. The upper limit would be $\lambda < (3.0 + 1.28)\sigma = 4.28\sigma$. The result is stated as: the upper limit corresponding to significance $1.35 \cdot 10^{-3}$ and the power 0.9.

E.4 Example II.

The importance of knowledge of existence of a process before a measurement can be performed can be illustrated on a somewhat artificial example. Suppose according to a new theory elephants have wings. An attempt to measure the length of the wings, for example, resulted in the limit that their length is between 0 and 2 centimeters, for example. The approach proposed here would state that no wings were found, but if they were longer than 5 centimeters, for example, they would have definitely been found.

This illustrates that by following the assumption that the new theory is correct without testing it, one is in danger of reporting a limit on an absurd parameter while according to the approach proposed it will be clearly stated that the new effect was not discovered and how strong the effect should have been to be discovered.

E.5 Example III.

Suppose it is known that observed data X comes from a Gaussian distribution with unknown mean λ and known variance σ:

$$p(x;\lambda) = \frac{1}{\sqrt{2\pi\sigma^2}} e^{-\frac{(x-\lambda)^2}{2\sigma^2}}$$

If it is desired to estimate the value of λ by a 90% one-sided confidence interval, given that the observed data x is $x = 0$, the interval on the values of λ is: $-\infty < \lambda < 1.28\sigma$.

Suppose, later, an existence of a new process is proposed according to which the same data X on the same experiment should have the distribution of:

$$p(x;\lambda,\mu) = \frac{1}{\sqrt{2\pi\sigma^2}} e^{-\frac{(x-\lambda-\mu)^2}{2\sigma^2}}, \quad \mu \geq 0$$

One is tempted (and according to the current approach this would happen) to state that based on the same data the total signal is $-\infty < (\lambda + \mu) < 1.28\sigma$. This is, of course, incorrect, because it is not known if the new process with the parameter μ exists. Instead, one should consider a statistical test with:

H_0: $p_0(x;\lambda) = \frac{1}{\sqrt{2\pi\sigma^2}} e^{-\frac{(x-\lambda)^2}{2\sigma^2}}$

H_1: $p_1(x;\lambda,\mu) = \frac{1}{\sqrt{2\pi\sigma^2}} e^{-\frac{(x-\lambda-\mu)^2}{2\sigma^2}}, \quad \mu \geq 0$

If the value of λ is known, the test would be very simple: if the observed data is greater than some x_0 the null hypothesis should be rejected. For a $1.35 \cdot 10^{-3}$ significance the critical region is defined as:

$$x > x_0 = \lambda + 3\sigma$$

If the observed data is inside of the critical region, a confidence interval on the value of μ may be constructed. If the null hypothesis is not rejected based on the observed data, the upper limit μ_u corresponding to the power of 0.9 can be found from the equation:

$$\int_{3\sigma+\lambda}^{\infty} \frac{1}{\sqrt{2\pi\sigma^2}} e^{-(x-\lambda-\mu_u)^2/2\sigma^2}\, dx = \int_{3\sigma-\mu_u}^{\infty} \frac{1}{\sqrt{2\pi\sigma^2}} e^{-y^2/2\sigma^2}\, dy = 0.9$$

If all the information available on the value of λ is in the form $-\infty < \lambda < \lambda_u$ with 100% confidence, one is forced to construct a conservative test as above assuming that $\lambda = \lambda_u$. This will lead to the critical region corresponding to the significance $1.35 \cdot 10^{-3}$ constructed as:

$$x > x_0 = \lambda_u + 3\sigma$$

Again, as before, if the observed data is inside the critical region, the null hypothesis of absence of the secondary process μ can be rejected and the value of μ may be estimated. If the observed data is outside of the critical region, the null hypothesis is not rejected and an upper limit on the value of μ based on power of the test can be constructed as above. Note that the information on the value of λ_u should come from an independent experiment otherwise the constructed test and upper limit are not correct.

If, however, no information on the value of λ is available the proposed test will not yield any meaningful result as it is not possible to distinguish data X originating due to process λ or μ.

A more general statement can be made. If the null and the alternative hypotheses on the origin of observed data X come from the same family of probability distributions i.e:

$$p_0(x;\lambda) = f(x;\lambda) \quad \text{and} \quad p_1(x;\lambda,\mu) = f(x;\lambda+\mu)$$

and if no knowledge regarding the value of λ is available, it is not possible to construct a meaningful statistical test to differentiate the two.[1] However, if several independent

[1]Indeed, the hypothesis test should be constructed in such a way so that the critical region on the values of X does not depend on λ. A procedure for constructing such a region was proposed by Neyman and Pearson [40] for the case when:

$$\phi(x;\lambda) = \frac{d\ln p_0(x;\lambda)}{d\lambda} \qquad \frac{d\phi(x;\lambda)}{d\lambda} = A(\lambda) + B(\lambda)\phi(x;\lambda)$$

For these conditions to be satisfied the function $p_0(x;\lambda)$ should come from exponential family of the form:

$$f(x;\lambda) = e^{Z(\lambda)T(x)+Q(\lambda)+S(x)}$$

where $Z(\lambda)$, $Q(\lambda)$, $T(x)$, $S(x)$ are some functions and $Z(\lambda)$, $Q(\lambda)$ are infinitely differentiable functions of λ. The equation of hypersurface $\phi(x;\lambda) = const$ in the X-space is equivalent to the equation $T(x) = const$.

Since in the considered case both p_0 and p_1 are of the same type, the likelihood ratio p_1/p_0 is inde-

observations x_1 and x_2 can be made such that it is known that data x_1 originated due to process with parameter λ only and x_2 is due to possible $(\lambda + \mu)$ the test constructed in the form:

$$p_0(x_1, x_2; \lambda) = f(x_1; \lambda) f(x_2; \lambda) \quad \text{and} \quad p_1(x_1, x_2; \lambda, \mu) = f(x_1; \lambda) f(x_2; \lambda + \mu)$$

will have the power to differentiate whether or not the data x_2 came from a new process even if no information on λ is available before the test.

E.6 When is the new theory valid?

Any theory of a physical process should be considered "admissible" if no observed data contradicts predictions based on the theory. However, in statistical tests it is only possible to reject a theory in favor of some other theory and it is not possible to state with absolute certainty whether or not the given theory describes the given process correctly.

The question of how much evidence contradicting to validity of the old theory in favor of the new one should be observed in order to declare that the new theory correctly describes the given physical process is a philosophical one. Obviously, the answer to this question is of great practical importance and will govern the choice of desired significance and power in formulating and performing the test.

---

pendent of the values of x on the hypersurface $\phi(x; \lambda) = const$ and the equation for the critical region corresponding to the error of the first kind ξ becomes:

$$\begin{cases} \xi \int_{\phi(x;\lambda)=const} p_0(x; \lambda) dx = \int_{\phi(x;\lambda)=const;\ p_1/p_0>q} p_0(x; \lambda) dx \\ \frac{p_1(x;\lambda,\mu)}{p_0(x;\lambda)} = e^{const \cdot (Z(\lambda+\mu)-Z(\lambda))+Q(\lambda+\mu)-Q(\lambda)} > q \end{cases} \tag{E.1}$$

Since the integration in (E.1) is performed over all x for which $p_1/p_0 > q$ is true and because $p_1/p_0 > q$ is either always true or always false for all values of X, the equation (E.1) becomes:

$$\xi \int_{\phi(x;\lambda)=const} p_0(x; \lambda) dx = \int_{\phi(x;\lambda)=const} p_0(x; \lambda) dx$$

For a given ξ this equation can be satisfied only if $p_0(x; \lambda) \equiv 0$ or if $\xi = 1$. The former condition is not interesting and the later one states that the null hypothesis should be rejected all the time regardless of the value x.

Bibliography

[1] R. Abusaidi et al. Exclusion limits on the wimp-nucleon cross section from the cryogenic dark matter search. *Phys. Rev. Lett*, 84:5699–5703, 2000.

[2] U. Amaldi et al. *Phys. Lett. B*, 260:447, 1991.

[3] R. Atkins et al. *Nuclear Instruments and Methods in Physics Research,Section A*. in preparation.

[4] R. Atkins et al. *Nuclear Instruments and Methods in Physics Research,Section A*, 449:478–499, 2000.

[5] R. Atkins et al. Observation of TeV gamma rays from the Crab nebula with milagro using new background rejection technique. 2003. in preparation.

[6] R. Becker-Szendy et al. *Nuclear Instruments and Methods in Physics Research,Section A*, 352:629, 1995.

[7] C. L. Bennett et al. 2003. available as astro-ph/0302207.

[8] A. Benoit et al. First results of the EDELWEISS WIMP search using a 320 g heat-and-ionization Ge detector. *Phys. Lett B*, 513:15–22, 2001.

[9] Lars Bergström et al. *Astroparticle Physics*, 9:137–162, 1998. available as astro-ph/9712318.

[10] R. Bernabei et al. Searching for wimps by the annual modulation signature. *Phys. Lett. B*, 424:195–201, 1998.

[11] C. Caso et al. *The European Physical Journal*, C3:1, 1998. partial update is available on http://pdg.lbl.gov/.

[12] T.C. Van Flandern and K.F. Pulkkinen. Low-precision formulae for planetary positions. *Astrophysical Journal*, 41:391–411, 1979.

[13] L. Fleysher and R. Fleysher. Milagro calibration system. In Milagro Memoranda [36].

[14] L. Fleysher, R. Fleysher, and T. Haines. Methods of photo-electron calibration. In Milagro Memoranda [36].

[15] L. Fleysher, R. Fleysher, T. Haines, and P. Nemethy. Angle fitter 3++. In Milagro Memoranda [36].

[16] L. Fleysher, R. Fleysher, A. Mincer, and P. Nemethy. Slewing extrapolation. In Milagro Memoranda [36].

[17] L. Fleysher, R. Fleysher, and P. Nemethy. Time pedestals ii (enhancements). In Milagro Memoranda [36].

[18] L. Fleysher, R. Fleysher, and P. Nemethy with I. Leonor. Time pedestals. In Milagro Memoranda [36].

[19] Lazar Fleysher, Roman Fleysher, and Allen Mincer. Pointing with milagro. In Milagro Memoranda [36].

[20] R. Fleysher and L. Fleysher. An invitation to random functions. In Milagro Memoranda [36].

[21] N. Gehrels and P. Michelson. *Astropart. Phys.*, 11:277, 1999.

[22] Javier Bussons Gordo. Sampling and curvature corrections from milagro data itself. In Milagro Memoranda [36].

[23] Javier Bussons Gordo. Event filtering prior to the core and angle fitters. In Milagro Memoranda [36].

[24] Andrew Gould. Resonant enhancements in weakly interacting massive particle capture by the earth. *Astrophysical Journal*, 321:571–585, 1987.

[25] A. Habig et al. An indirect search for wimps with super-kamiokande. 2001. hep-ex/0106024v1.

[26] Todd Haines. A causality criteria — work in progress. In Milagro Memoranda [36].

[27] Scott Hugenberger. Edge finding code. In Milagro Memoranda [36].

[28] A.X. Huo et al. In *Proceedings of the Twenty-First International Cosmic Ray Conference*, volume 2, page 427, 1990. edited by J. Protheroe.

[29] Gerard Jungman, Mark Kamionkowski, and Kim Griest. Supersymmetric dark matter. *Physics Reports*, 267:195, 1996. also available at http://t8web.lanl.gov/people/jungman/.

[30] J. Knapp and A. Heck. *KfK*, 5196 B, 1993. http://www-ik3-fzk.de/ heck/corsika.

[31] Edward W. Kolb and Michael S. Turner. *The Early Universe*. Addison-Wesley Publishing Co, 1990.

[32] I. Leonor. Tot-pe conversion using occupancy method. In Milagro Memoranda [36].

[33] I. Leonor. *Search for a TeV Component of Gamma-Ray Bursts Using the Milagrito Detector*. PhD thesis, University of California at Irvine, 2000.

[34] Ti-pei Li and Yu-qian Ma. Analysis methods for results in gamma-ray astronomy. *Astrophysical Journal*, 272:317–324, 1983.

[35] J. F. McCullough and Javier Bussons Gordo. Tuning the angle fitter, sampling and curvature corrections for milagro. In Milagro Memoranda [36].

[36] *Milagro Memoranda*. http://scipp.ucsc.edu/milagro/memos.

[37] M. Mori et al. *Phys. Rev. D*, 48:5505, 1993.

[38] P. Nemethy, L. Fleysher, and R. Fleysher. Time calibration: Stability studies. In Milagro Memoranda [36].

[39] J. Neyman. Outline of a theory of statistical estimation based of the classical theory of probability. *Phil. Trans. R. Soc. London, Series A*, 236:333–380, 1937. also available in "A Selection of Early Statistical Papers of J. Neyman", (Berkeley, University of California Press, 1967).

[40] J. Neyman and E. S. Pearson. On the problem of the most efficient tests of statistical hypotheses. *Phil. Trans. R. Soc. London, Series A*, 231:289–337, 1933.

[41] J.P. Ostriker et al. *Ap. J. Lett.*, 193:L1, 1974.

[42] H. Pagels and J.R. Primack. *Phys. Rev. Lett*, 48:223, 1982.

[43] William H. Press and David N. Spergel. Capture by the sun of a galactic population of weakly interacting massive particles. *Astrophysical Journal*, 296:679–684, 1985.

[44] Vera C. Rubin and W. Kent Ford, Jr. Rotation of the andromeda nebula from a spectroscopic survey of emission regions. *Ap. J.*, 159:379, 1970.

[45] R. Sancisi and T.S. van Albada. *Dark Matter in the Universe*, page 67. Reidel, Dordrecht, 1987. eds. J. Kormendy and G. Knapp.

[46] G. Di Sciascio, B. D'Ettorre Piazzoli, and M. Iacovacci. A comparative study of the electron and photon components in photon-induced air showers. *Astropart. Phys.*, 3:313–322, 1997.

[47] Martin F. Sohnius. Introducing supersymmetry. *Physics Reports*, 128:39–204, 1985.

[48] G. Sullivan and A. Smith. An off-pond core finder. In Milagro Memoranda [36].

[49] M.S. Turner. *Physics Reports*, 197:67, 1990.

[50] Gaurang B. Yodh. Algorithm for rejection of non-shower hits in milagro. In Milagro Memoranda [36].

[51] Gaurang B. Yodh. A simple algorithm for hadron rejection in milagro. In Milagro Memoranda [36].

[52] Gaurang B. Yodh. Event energy determination. In Milagro Memoranda [36].

[53] F. Zwicky. *Helv. Phys. Acta*, 6:110, 1933.